SCUOLA di DOTTORATO

Dottorato in Ingegneria dell'Informazione

Direttore della Scuola di Dottorato
prof. Felice Arena

Collegio dei docenti
Dottorato di Ricerca in Ingegneria dell'Informazione
XXXVIII ciclo

Tommaso ISERNIA (coordinatore)
Giuseppe ARANITI
Francesco BUCCAFURRI
Claudio CAMPOLO
Riccardo CAROTENUTO
Giuseppe COPPOLA
Marintonia COTRONEI
Lorenzo CROCCO
Dominique DALLET
Claudio DE CAPUA
Francesco DELLA CORTE
Loreto DI DONATO
Giuliana FAGGIO
Gioia FAILLA
Sofia GIUFFRÈ
Voicu GROZA
Gianluca LAX
Aimè LAY EKUAKILLE
Elena Simona LOHAN
Pietro MANZONI
Giacomo MESSINA
Marina MISTRETTA
Antonella MOLINARO
Andrea Francesco MORABITO
Francesco Carlo MORABITO
Rosario MORELLO
Gabriel-Miro MUNTEAN
Giuseppe MUSOLINO
Fortunato PEZZIMENTI
Filippo Gianmaria PRATICO'
Sandro RAO
Maria ROMANO
Domenico ROSACI
Giuseppe Ruggeri
Mariateresa RUSSO
Alexey VINEL

I would like to express my profound appreciation to my committee. I also extend my deepest gratitude to my supervisor, Prof. Francesco Della Corte, for his guidance and support throughout these years. I further wish to thank Dr. Maurizio Casalino for his guidance and valuable feedback throughout this work, Dr. Teresa Crisci for her support and constructive suggestions, and my family for their constant support and encouragement.

This work was supported by the European Union - Next Generation EU under the Italian National Recovery and Resilience Plan (NRRP), Mission 4, Component 2, Investment 1.3, CUP C37G22000480001, partnership on "Telecommunications of the Future" (PE00000001 - program "RESTART").

Babak Hashemi is a researcher in photonics with a focus on integrated photonic devices, optical waveguides, and experimental characterization. His research combines device design, fabrication-aware optimization, and hands-on optical measurements, with interests in integrated photonics, sensing technologies, and applied photonic systems.

SCUOLA DI DOTTORATO
Università Mediterranea di Reggio Calabria

DIPARTIMENTO
Dipartimento di ingegneria dell'informazione, delle infrastrutture e dell'energia sostenibile (DIIES)

DOTTORATO DI RICERCA
Ingegneria dell'Informazione

S.S.D.
IINF-01/A
XXXVIII CICLO

DESIGN, FABRICATION AND CHARACTERIZATION OF PHOTONIC INTEGRATED SWITCH CIRCUITS FOR TELECOMMUNICATION APPLICATIONS

[redacted]
Dottorando
Babak Hashemi

Tutor
Prof. Francesco Giuseppe Della Corte
[redacted]

Co-tutor
Dr. Maurizio Casalino
Dr. Teresa Crisci
[redacted]

Coordinatore del Dottorato
Prof. Tommaso Isernia
[redacted]

Finanziato dall'Unione europea NextGenerationEU
Ministero dell'Università e della Ricerca
Italiadomani
RESTART

Index

Abstract

Abstract

The rapid growth of optical communication networks and the widespread deployment of fiber-to-the-home (FTTH) systems require compact, scalable, and energy-efficient photonic switches. Silicon photonics provides a mature and cost-effective platform for large-scale integration; however, designing optical switches that combine broadband operation, low power consumption, fabrication tolerance, and scalability remains challenging. This thesis addresses these challenges through the design, simulation, fabrication, and characterization of integrated photonic switches based on thermo-optic and graphene-enabled electro-optic effects.

This work was carried out within the framework of the GrapHICS project (Graphene/a-Si:H Photonic Integrated Circuit Switch), which aims to develop a new photonic platform by combining standard silicon photonics with advanced materials such as graphene and hydrogenated amorphous silicon (a-Si:H). The final goal of the project is the realization of active, remotely reconfigurable optical switching matrices capable of replacing passive splitters in passive optical networks, thereby reducing operational costs and improving network flexibility and reliability.

Several photonic switch architectures are investigated, including Mach–Zehnder interferometers, ring resonators, multimode interference (MMI) devices, and adiabatic structures. Through numerical comparison, adiabatic thermo-optic switches and MMI-based Mach–Zehnder thermo-optic switches are identified as the most suitable solutions for broadband and fabrication-tolerant operation. A key original contribution of this thesis is the proposal and detailed analysis of a novel adiabatic thermo-optic switch based on smoothly tapered waveguides. The adiabatic design ensures gradual mode evolution, resulting in low optical loss and reduced sensitivity to wavelength and polarization variations. Simulation results demonstrate efficient switching for both TE and TM polarizations across the C- and L-bands, with low insertion loss, high extinction ratio, and moderate power consumption.

The optimized adiabatic switch is then used as a basic building block for the design of scalable optical switching matrices. Using an S-parameter-based modeling approach and system-level simulations, complete 2×2 and 4×4 switch matrices are designed and analyzed, demonstrating the feasibility of extending the architecture toward larger N×N configurations suitable for telecommunication applications. In parallel, an MMI-based Mach–Zehnder thermo-optic switch is designed, fabricated, and experimentally characterized. The fabrication process is developed and optimized in a cleanroom environment using silicon-on-insulator technology and laser-writer photolithography. To achieve high-quality waveguides, a Bosch deep reactive ion etching process is adopted, enabling accurate dimensional control and vertical sidewalls. Optical measurements confirm broadband operation and thermo-optic switching behavior in good agreement with simulations.

To overcome the speed limitations of thermo-optic devices, graphene-based electro-optic structures are also investigated. A graphene–insulator–graphene capacitor is fabricated and characterized, and its integration into photonic waveguides is studied through detailed modeling. By positioning graphene in regions of high optical field overlap and introducing a-Si:H as an additional guiding layer, enhanced electro-absorption modulation and high-speed operation are achieved in simulation. The proposed graphene-based devices demonstrate the potential to operate at data rates up to 40 Gb/s with compact footprints and reduced power consumption.

In conclusion, this thesis presents original device concepts, optimized fabrication strategies, and scalable design approaches for integrated photonic switches. The combination of adiabatic structures, MMI-based interferometers, and graphene-enabled electro-optic functionality provides a flexible and robust platform for future reconfigurable photonic integrated circuits and high-capacity optical communication systems.

Contents

Introduction

The rapid evolution of integrated photonics has established silicon photonics as a key enabling technology for modern optical communication and signal-processing systems. Leveraging the maturity of CMOS-compatible fabrication processes, silicon photonics allows the realization of compact, low-loss, and highly integrated optical devices with a level of scalability that is difficult to achieve with alternative material platforms. As a result, silicon-based photonic circuits have become a central focus of research for the implementation of complex optical functionalities, including switching, modulation, and routing.

Within this technological framework, integrated optical switches play a fundamental role as elementary building blocks for reconfigurable photonic circuits. A wide range of switching mechanisms and device architectures has been investigated in the literature, each offering distinct advantages and limitations in terms of bandwidth, footprint, power consumption, wavelength dependence, and fabrication complexity. Adiabatic devices, resonant structures, and multimode-based components represent some of the most widely explored solutions, highlighting the broad design space available for integrated optical switching on silicon.

Thermo-optic switching remains one of the most established approaches in silicon photonics due to its intrinsic robustness and compatibility with standard fabrication processes. By exploiting the temperature dependence of the silicon refractive index, thermo-optic devices enable reliable control of optical signals with relaxed fabrication tolerances and stable broadband operation. In this context, architectures based on multimode interference (MMI) couplers and adiabatic waveguide transitions have attracted particular interest, as they offer reduced sensitivity to wavelength and polarization while maintaining compact footprints and low insertion losses. These properties make such structures especially suitable for large-scale integration, where device uniformity and reproducibility are critical.

Alongside purely silicon-based solutions, hybrid integration with emerging materials has become an active research direction aimed at extending the performance limits of integrated photonic devices. Among these materials, graphene (Gr) has emerged as a promising candidate due to its electrically tunable optical properties and ultra-fast carrier dynamics. When integrated with silicon waveguides, graphene enables efficient electro-optic and electro-absorption effects that are not readily achievable with silicon alone. This hybrid approach provides additional degrees of freedom in device design and opens new possibilities for compact and high-speed photonic components.

This thesis addresses the analysis and development of integrated optical switching devices within the silicon photonics platform, combining numerical modeling, device design, fabrication considerations, and experimental characterization. Different switching concepts are investigated in order to evaluate their suitability for scalable photonic integration, with particular attention to broadband operation, polarization behavior, and fabrication tolerance. Both thermo-optic and graphene-assisted approaches are examined, allowing a comparative assessment of their respective performance and technological implications.

The remainder of this thesis is organized as follows. Chapter 1 presents the motivation of the project and defines the main objectives of the work. Chapter 2 introduces the theoretical background and fundamental concepts required for the analysis and design of the proposed devices, including silicon-

based waveguides, thermo-optic effects, multimode interference, adiabatic structures, and graphene-related electro-optic phenomena. Chapter 3 describes the technological tools, fabrication processes, and experimental techniques employed for device realization. Chapter 4 focuses on the design and numerical simulation of the proposed photonic devices, discussing their operating principles simulation results. Chapter 5 presents the fabrication and experimental characterization of the simulated devices, followed by a discussion of the measured results. Finally, the conclusions summarize the main outcomes of the thesis and outline possible directions for future work.

1. Motivation and Project Objectives

Fiber-to-the-Home (FTTH) is a broadband access technology designed to deliver high-speed internet connections directly to individual homes through optical fibers. It represents one of the most advanced solutions for modern telecommunication infrastructures, capable of providing large bandwidth, high reliability, and low signal attenuation over long distances. However, as the number of connected users and the demand for data continue to grow, conventional FTTH networks face increasing challenges in terms of flexibility, scalability, and energy efficiency. To address these limitations, this thesis focuses on the development of integrated optical switching technologies based on silicon photonics, aimed at improving the performance and reconfigurability of FTTH systems.

1.1 Current Fiber-to-the-Home network architecture

As illustrated in Fig. 1, the optical signal generated at the central office (OLT) is divided through several levels of optical splitters before reaching the end users. The first splitting level, called the Primary Flexibility Point (PFP), distributes the optical signal typically in a 1×4 configuration toward several Secondary Flexibility Points (PFS). Each PFS then performs a further 1×16 split, connecting hundreds of households (HH). The final distribution to individual buildings occurs at the building termination point (PTE), completing the FTTH link.

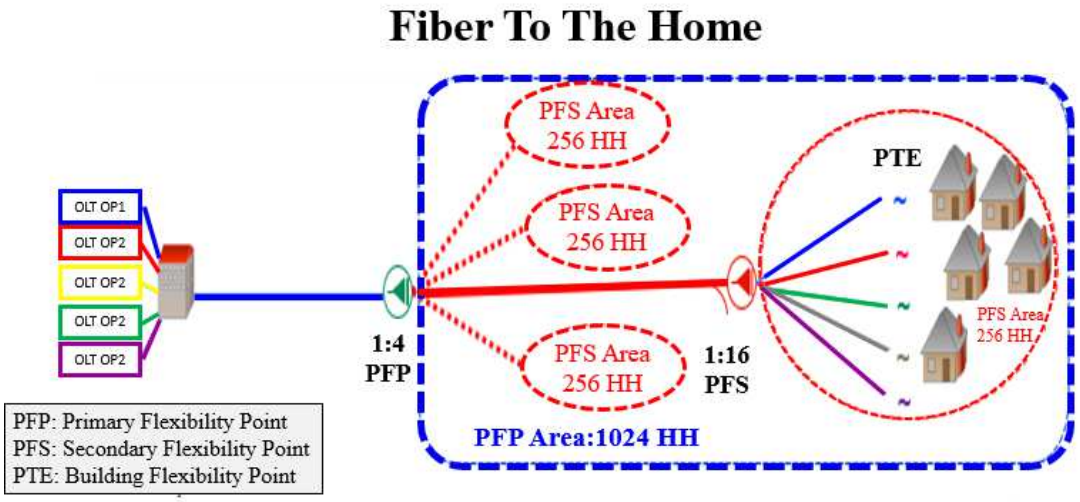

Figure 1. Architecture of a TDMA-PON network showing signal distribution from the central office to multiple users through passive optical splitters

1.2 Limitations of conventional FTTH architectures

While this structure is reliable and has enabled widespread deployment of FTTH systems, it also introduces important limitations. The main issue appears at the PFS level, where the interconnection between the feeder and distribution fibers is made in a static permutation area that contains passive splitters and connectors. Each time a new subscriber is added or an existing connection is modified, a technician must manually open the cabinet and reconnect fibers, as shown in Fig. 2. This procedure is

slow, expensive, and requires skilled personnel, making it difficult to scale and prone to human error. In addition, every passive 1×16 splitter divides the optical power among all users, introducing significant losses that limit both network reach and overall energy efficiency.

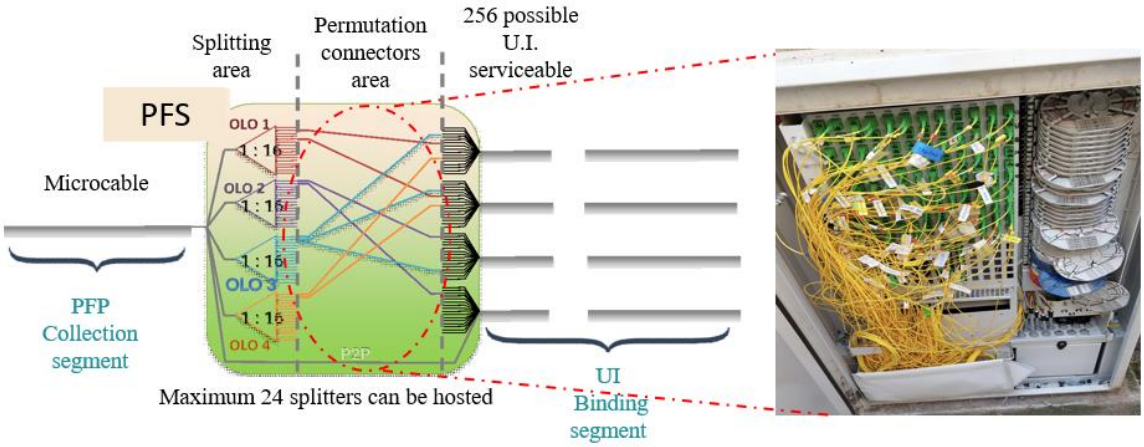

Figure 2. The secondary splitting level located inside the PFS/CNO street cabinet.

1.3 Motivation for silicon photonic switching matrices

To overcome these issues, this project proposes replacing the fixed permutation area with a reconfigurable active optical switch matrix integrated on a silicon photonic platform. This new design enables remote and dynamic routing between any Optical Line Terminal (OLT) and any user without physical intervention. The switch matrix functions as an intelligent optical node capable of electronically redirecting light paths, enabling faster service setup, easier maintenance, and improved scalability of the optical network.

The new architecture is based on an M×N optical switch, composed of multiple 1×2 switching elements connected together. For instance, an 8×8 matrix contains 121 individual 1×2 switches arranged in cascade, as illustrated in Fig. 3. Each small switch redirects the light by modifying the refractive index within a localized region of the silicon waveguide. By connecting these individual units together, the complete matrix can create flexible and non-blocking optical paths, allowing any input to be connected to any output without interfering with other active channels.

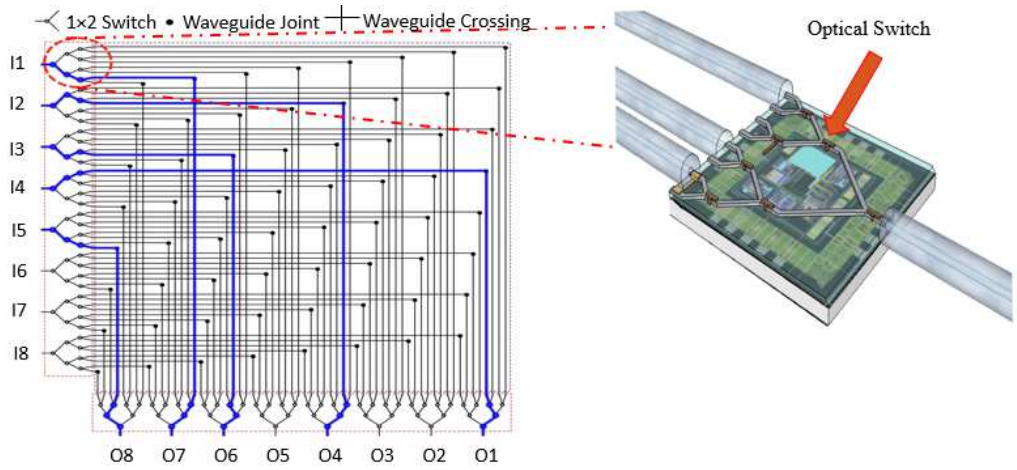

Figure 3. Schematic of the matrix for the realization of an 8 x 8 optical switch matrix composed of cascaded 1×2 and 2×1 integrated switches forming a scalable non-blocking routing structure [1].

To meet the performance goals, each 1×2 optical switch must combine compact size, low cost, low driving power, and broadband wavelengths performance for both TE and TM polarization modes. These parameters are essential to ensure that the devices can be integrated into large-scale switch matrices while maintaining low optical losses and stable operation. In addition, low polarization dependence, thermal stability, and fabrication tolerance are required to achieve high reliability and repeatability.

During this work, several types of photonic integrated optical switches were investigated through numerical simulation, including Mach–Zehnder interferometer (MZI), ring resonator, multimode interference (MMI), and adiabatic thermo-optic configurations. Each architecture presents specific advantages and limitations in terms of footprint, bandwidth, wavelength sensitivity, and fabrication tolerance. Based on a comparative performance analysis, two device structures were selected for further development and fabrication due to their simplicity, robustness, and compatibility with standard silicon photonic processes.

The first selected structure is the adiabatic thermo-optic switch, which guides light gradually from one branch to another by smoothly varying the waveguide geometry and the local temperature. This gradual transition avoids abrupt mode coupling and reduces optical losses, resulting in broadband, polarization-insensitive, and low-loss operation. At the end of simulation of these switches, the overall performance of this 1×2 optical switch have been exploited to investigate a full matrix switch.

The second selected structure is the thermo-optic Mach–Zehnder switch incorporating multimode interference (MMI) couplers. This architecture relies on controlled interference between optical modes propagating in a multimode section to split and recombine the optical field efficiently. MMIs are compact, broadband, and highly tolerant to fabrication variations, making them excellent candidates for integration in large-scale optical circuits.

Both approaches are fully compatible with silicon photonic foundry processes, allowing the realization of low-power (<2 mW) and fast-switching (<100 µs) devices with high reproducibility. Their combination offers an effective balance between compactness and broadband performance, enabling

the design of a reconfigurable, low-loss, and energy-efficient optical switch matrix.

In addition to the thermo-optic adiabatic and MMI-based switches, we have also investigated electro-absorption modulators based on double-layer graphene (DLG). These modulators are considered key components for future fiber-to-the-home (FTTH) systems because they offer high speed, low driving voltage, and broadband operation. As part of this work, the electrical behavior of the graphene capacitor embedded in the modulator was studied in detail, and its capacitance, including both geometric and quantum components, was extracted to understand how the applied voltage modifies the Fermi level of graphene and therefore its optical absorption. This analysis provides the basis for evaluating the modulation efficiency and the potential of graphene-based modulators for next-generation access networks.

This thesis was carried out within the framework of the GrapHICS project (Graphene/a-Si:H photonic Integrated Circuit Switch), a collaborative research initiative aimed at developing a novel photonic integration platform compatible with standard CMOS fabrication processes, funded under the Italian National Recovery and Resilience Plan (NRRP) of the NextGenerationEU partnership for "Telecommunications of the Future" (PE00000001—program "RESTART"—FP5 GraPHICs).

The project exploits the low cost and low thermal budget of hydrogenated amorphous silicon (a-Si:H), combined with the outstanding electro-optical properties of graphene, to enable active, scalable photonic devices. The project was proposed by Open Fiber and coordinated by the University of Naples Federico II, with the participation of the Consiglio Nazionale delle Ricerche (CNR) and the University of Mediterranea of Reggio Calabria.

In summary, this project focuses on the design and optimization of adiabatic and MZ-MMI thermo-optic switches as the key building blocks for a silicon photonic switching platform. These devices are intended to replace the fixed passive components in current FTTH cabinets, allowing remote and dynamic optical routing while improving flexibility, reliability, and overall network efficiency.

2. Background and theory

2.1 Silicon in Photonics

In recent years, the continuous growth in data traffic caused by cloud services, artificial intelligence, and the Internet of Things (IoT) has led to an increasing demand for faster and more energy-efficient communication systems. The constant evolution of telecommunication networks, combined with the limitations of traditional electronic interconnects, has accelerated the transition toward optical technologies capable of handling high-speed data transmission with minimal delay and low energy consumption. Within this context, silicon photonics has emerged as one of the most promising research areas for developing compact and high-performance optical systems, offering the possibility to integrate optical and electronic functionalities on the same chip. [2]

Silicon photonics leverages silicon as the primary material for guiding and manipulating light on an integrated platform. Owing to its transparency in the standard telecommunication wavelength range (1.3–1.6 μm) and its high refractive index contrast with silicon dioxide, silicon allows for strong light confinement in sub-micrometric structures. This property facilitates the realization of compact photonic integrated circuits (PICs) that integrate hundreds of optical components, including waveguides, couplers, and resonators, on a single substrate. The high level of integration achievable on silicon platforms has made it possible to design devices that combine low optical losses, broad bandwidth, and reduced footprint, ensuring compatibility with large-scale production processes. [3] [4]

Among the different applications of silicon photonics, optical switching represents one of the most critical functions in the development of reconfigurable optical networks and high-speed telecommunication systems. Optical switches allow the control of light propagation among different paths without converting the optical signal into an electrical one, ensuring higher speed and lower power consumption compared to traditional electronic switches. Various switching mechanisms have been explored, including electro-optic, thermo-optic, and all-optical effects. Among these, the thermo-optic effect stands out for its simplicity of implementation, high reliability, and excellent fabrication tolerance. It relies on the variation of the refractive index of silicon with temperature, enabling light to be efficiently redirected within integrated structures such as Mach–Zehnder interferometers (MZIs), multimode interference (MMI) couplers, and adiabatic waveguide couplers. Although the thermal response is slower than electro-optic modulation, the thermo-optic effect remains the most widely adopted approach in silicon-based optical switching, particularly for broadband and polarization-insensitive applications. [5]

Recent research efforts have also focused on enhancing the performance of silicon photonic switches by introducing novel materials with tunable optical properties. Among them, graphene has attracted exceptional attention due to its outstanding electrical and optical characteristics, including ultra-fast carrier dynamics, broadband absorption, and strong electro-refractive and electro-absorptive effects. Integration of graphene with silicon introduces an extra degree of tunability, allowing modulation of the refractive index or optical absorption through electrical control [6]. This hybrid approach enables the design of graphene-assisted silicon photonic switches, which combine the robustness and scalability of silicon technology with the superior optical tunability of two-dimensional materials. Furthermore, the deposition of graphene in buried or lateral configurations within the waveguide

structure enhances its interaction with the guided optical mode, improving switching efficiency and reducing insertion losses.

From a technological point of view, the silicon photonics industry has developed very rapidly in recent years, mainly due to the growth of dedicated foundries and the introduction of standardized fabrication platforms. Several major companies, such as Intel, Cisco, and Luxtera, have already demonstrated silicon photonic transceivers and optical switching modules capable of data transmission rates well above 100 Gb/s. As reported by Yole Développement (2021), the global silicon photonics market is expanding significantly during these years from about 87 million USD in 2020 to more than 1.1 billion USD by 2026, which corresponds to an average annual growth rate of nearly 49%. The main applications driving this growth are datacenter interconnects, 5G optical transceivers, and co-packaged optics, followed by photonic computing, automotive LiDAR, and biomedical and quantum technologies. The overall market forecast and distribution of application areas are illustrated in Fig. 4.

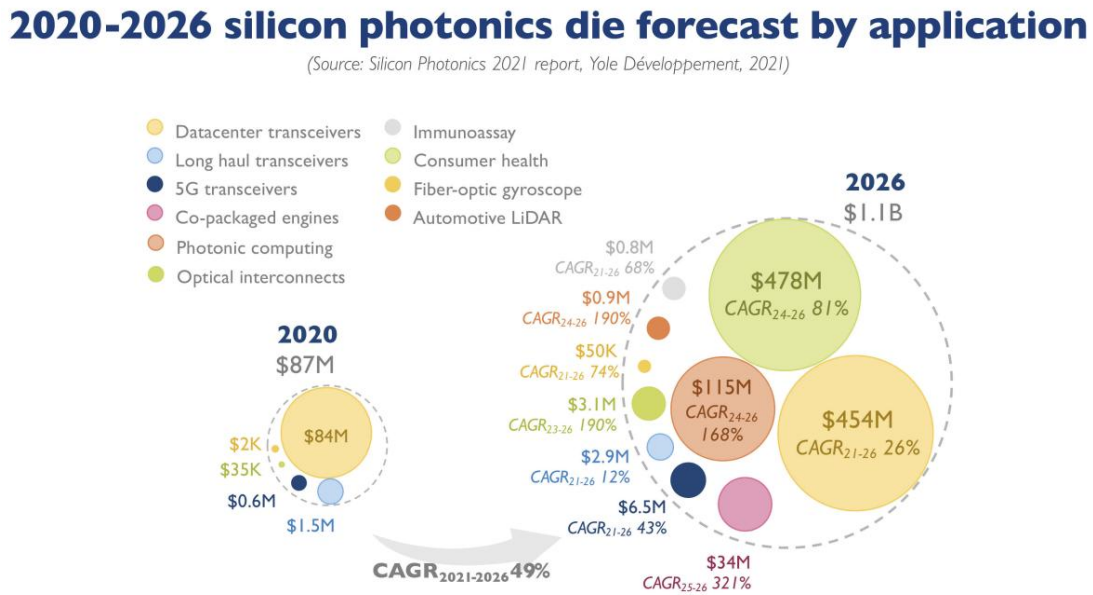

Figure 4. Global silicon photonics market forecast and main application sectors. Image taken from http://www yole.fr/Si_Photonics_Datacom_Sensing.aspx.

In conclusion, silicon photonics offers a mature and scalable technological platform for the implementation of thermo-optic switches and graphene based modulators. These devices combine the low-loss guiding capability of silicon with the dynamic tunability of emerging materials, ensuring efficient control of light propagation within integrated circuits. The continued advancement of this field is expected to play a key role in enabling high-speed, low-power, and broadband optical switching and modulation architectures for future telecommunication and data-processing systems.

This work mainly focuses on the use of thermo-optic tuning mechanisms on silicon, together with the previously developed adiabatic and MMI switch designs, representing a practical and efficient strategy for implementing high-performance integrated optical switches. The adiabatic configuration,

characterized by smooth transitions in the waveguide geometry, ensures high fabrication tolerance, low polarization sensitivity, and a broad operational bandwidth, which are essential for stable operation in real communication systems. By combining these thermo-optic switching principles with optimized silicon photonic structures, the developed devices achieve compact, broadband, and low-loss performance suitable for the requirements of modern telecommunication networks.

2.2 Optical integrated switches

2.2.1 Background

Over the last decade, the remarkable progress in microelectronic and photonic integration technologies has positioned integrated photonics as a key platform for high-speed data transmission and signal management. Optical systems offer transmission capacities and processing speeds far beyond those achievable with purely electronic technologies [7], [8]. Within this context, integrated photonic switches play a crucial role in routing optical signals among multiple channels under electrical control, offering high speed, low latency, and energy-efficient operation. [9] [10] [11]

Unlike the electronic components, photonic switches offer the advantage of low power consumption and wide bandwidth. These features are vital as data rates continue to increase and the limitations of electronic switching become more pronounced. The miniaturization of photonic switches on silicon platforms has further promoted their adoption, leveraging the established silicon photonics technology. This technology is enabled by the compatibility with existing semiconductor manufacturing processes, and allows micro-scale and cost-effective devices, covering the way for large-scale deployment. This integration also makes it possible to build compact photonic circuits directly on a chip, which can be easily combined with electronic microchips, enabling electronic–photonic hybrid devices with enhanced capabilities. [12] [13]

Most integrated photonic switches are based on Mach–Zehnder interferometers (MZI) [14], [15] or multimode interference (MMI) couplers [16], [17]. These structures manipulate light by inducing controlled phase shifts or modal interference through external actuation. The physical mechanism responsible for switching typically exploits either electro-optic [18], [19] or thermo-optic effects [20] [21], which locally modify the refractive index of the waveguide material. The application of an electrical signal alters the refractive index in a specific region of the device, redirecting the optical power between output ports. [20], [21]. Although MZI and MMI-based switches have been successfully demonstrated, they exhibit certain limitations. Their performance is often sensitive to wavelength and polarization, which can be problematic in systems where a wide spectral band must be routed simultaneously, such as in wavelength-division multiplexed (WDM) networks [22], [23], [24], [25]. To overcome these limitations, different types of switches have been employed for fabricating a complete switch matrix.

2.2.2 Comparison of Integrated Silicon Photonic Switches

Integrated optical switches on silicon photonic platforms have been developed in several configurations, each relying on different physical mechanisms and device geometries. The most common structures include microring resonators (MRRs), Mach–Zehnder interferometers (MZIs), and multimode-interference (MMI)–based switches, together with a range of hybrid designs that combine

more than one mechanism. These devices modulate light by inducing a controllable phase shift inside the switching region. From a physical perspective, two main phase-shifting mechanisms are used in silicon:

A: Thermo-optic (TO) tuning, where the refractive index is modified by localized Joule heating through metallic heaters;

B: Electro-optic (EO) tuning, where the carrier-dispersion effect inside a PIN or PN junction changes the refractive index under an applied electrical bias.

Each mechanism provides different advantages. TO-based switches typically allow compact geometries and broad wavelength operation, while EO-based devices offer lower power consumption and much faster switching speeds, although the achievable refractive-index change is smaller, often requiring longer devices. Both TO and EO effects are non-latching, meaning that continuous electrical power is required to maintain the switched state.

MRR-based switches exploit resonance effects and can achieve very compact footprints, but they are inherently wavelength-selective and sensitive to fabrication tolerances. MZI-based switches provide broadband performance and high extinction ratios, at the cost of longer device length. MMI-based structures represent a strong alternative since they rely on self-imaging and are less sensitive to polarization or wavelength variations, making them suitable for broadband thermo-optic switching. In this work, we have particularly focused on MMI-based and adiabatic thermo-optic switches due to their tolerance to fabrication variations and compatibility with our cleanroom process constraints.

Overall, silicon-integrated photonic switches span a wide design space, each solution characterized by specific trade-offs in speed, power consumption, footprint, wavelength dependence, and fabrication complexity. In this thesis, we primarily investigate MMI-based thermo-optic switches and adiabatic structures, which provide broadband operation, fabrication tolerance, and compatibility with our processing capabilities, while also exploring graphene-based approaches for future high-speed and low-power switching applications.

2.3 Adiabatic structures

One of the 1×2 optical switch architectures investigated in this work is the adiabatic switch, which was selected for fabrication based on its favorable performance characteristics. In this section, the theoretical background and design development of adiabatic switches are presented, along with a review of relevant studies from the literature to provide a comprehensive understanding of their operating principles and advantages.

The adiabatic concept provides a method for designing optical components that are inherently broadband and polarization-insensitive. In adiabatic devices, the refractive index profile or waveguide geometry changes gradually along the propagation direction, allowing the optical field to remain in the same mode throughout the transition. This ensures that if the fundamental mode is excited at the input, all the optical power continues to propagate in that mode without coupling to higher-order modes or radiating into the cladding [26], [27], [28], [29], [30]. As a result, adiabatic devices exhibit stable and efficient performance over a wide wavelength range, with reduced dependence on

fabrication tolerances.

2.3.1 Theory

In general, a physical process is considered adiabatic if it occurs sufficiently slowly such that no transitions take place between different energy levels. This principle can be translated into the integrated optics domain by assuming that the propagating modes do not change even if the waveguide structure changes along the optical path. This means that, if a given mode (e.g., the fundamental one) is initially excited, all power remains in that mode as the waveguide geometry changes. As a result, no power is transferred to other modes or lost through radiation. The main advantage of adiabatic devices in integrated optics is that their performance does not rely on critical dimensions, such as the precise length of a resonator or a directional coupler. As a result, adiabatic devices show low sensitivity to wavelength and polarization variations and offer increased tolerance to fabrication imperfections. This leads to more relaxed technological requirements during fabrication. However, a common drawback of adiabatic devices is their relatively larger footprint compared to resonant or interference-based structures. For example, an asymmetric Y-splitter (-3 dB) can be made adiabatic if the angle between the two branches is sufficiently small, as (2.1) shows [31], [32]:

$$\theta < \Delta\beta / 0.43\gamma \tag{2.1}$$

Where Δβ is the difference in the propagation constant between the two lowest order normal modes when the arms of the branch are well separated, and γ is the transverse propagation constant in the cladding region between arms. It turns out that the design of short devices imply either a large splitting between the two modes, or a strong coupling between the waveguides (low γ values). Such devices work well even when the technology used for fabrication has large minimum feature sizes, although this implies longer tapers. Using minimum feature sizes can further reduce the device length; for example, an adiabatic power splitter with a minimum feature size of 30 nm has demonstrated a coupling length as short as 5 μm. [33]

2.4 Multi-Mode interference structure

Another type of switch that has been studied and designed in this work for the realization of a 1×2 optical switch is based on multimode interference (MMI). The MMI concept is one of the most reliable and well-established approaches for optical power splitting and combining in integrated photonics.

How It Works: The Self-Imaging Effect

The principle of operation relies on self-imaging, a phenomenon that occurs when the input optical field is reproduced at periodic intervals along a multimode waveguide section. The use of this effect allows for the design of compact, broadband, and fabrication-tolerant devices suitable for high-performance optical switches. [34]

When light from a single-mode waveguide enters a wider multimode section, several guided modes

are excited simultaneously. Each mode travels with a different speed, defined by its propagation constant (β_m), and when all the modes combine, they create an interference pattern that changes gradually as the light moves along the waveguide. At certain distances, known as imaging lengths, the phase relationship between the modes causes the field to reconstruct one or more copies of the input field. This effect is known as self-imaging and is the main working principle behind MMI devices.

For a multimode region of width W, the propagation constants are determined by the effective refractive indices of the supported modes. Here, n_{eff} refers to the effective refractive indices of the guided modes in the multimode section, and the approximation is typically derived considering the fundamental and first-order modes, which primarily govern the self-imaging process. The difference in propagation constants between these modes can be approximated as (2.2):

$$\Delta\beta = \beta_0 - \beta_1 \approx \frac{\pi^2}{2n_{eff}W^2}\lambda \tag{2.2}$$

The beat length L_π/N, which defines the periodicity of the modal interference, is given by (2.3):

$$L_\pi = \frac{\pi}{\Delta\beta} = \frac{4n_{eff}W^2}{3\lambda} \tag{2.3}$$

Where λ is the operating wavelength. [35]

At distances equal to L_π/N (where N = 1, 2, 3, …), specific field distributions are formed corresponding to single or multiple self-images. The imaging condition for a 1×2 MMI coupler occurs when two identical self-images of the input field are formed at the output plane. The optical power is then equally distributed between the two output ports.

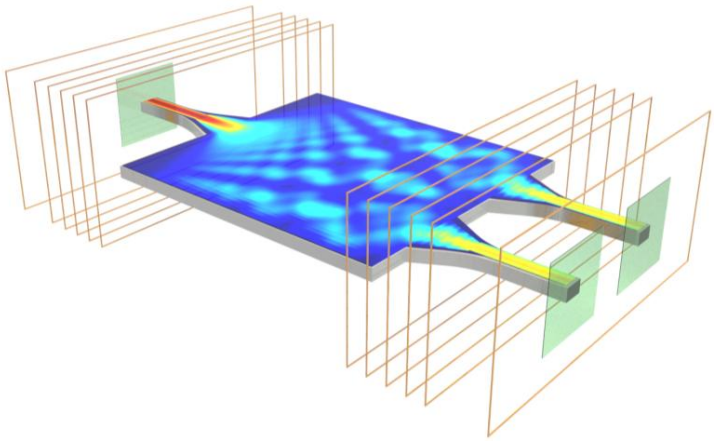

Figure 5. A schematic representation of the field distribution in a 1×2 MMI passive splitter. Image taken from https://optics.ansys.com/hc/en-us/articles/360042305194-Multi-Mode-Interference-MMI-Coupler

A schematic representation of the field distribution in a 1×2 MMI device in Fig. 5 shows how the single input field excites a multimode pattern that reproduces itself as two equal-intensity outputs after a defined propagation distance. The imaging distance can be adjusted by changing the width or length of the multimode region. The optical field amplitude at any point z along the propagation can be expressed as the sum of the guided modes: [36]

$$E(x,z) = \sum_m a_m \psi_m(x) e^{-i\beta_m z} \tag{2.4}$$

Where a_m represents the excitation coefficient of the m^{th} mode and $\psi_m(x)$ is the normalized transverse field distribution.

Self-imaging occurs when the accumulated phase differences between the excited modes satisfy the following condition: [34]

$$(\beta_m - \beta_0) L_{im} = 2m\pi \tag{2.5}$$

Which ensures that all modes recombine constructively to reproduce the input field.

The number of output images and the power distribution can be controlled by the input position and symmetry of the MMI structure. For example, when a single input waveguide is placed at the center of the multimode region, it produces two symmetric output with equal power. However, if the input waveguide is slightly shifted to one side, the output power can generate asymmetric splitting ratios. These characteristics make MMI structures very flexible and useful for many optical applications, including splitters, couplers, multiplexers, and optical switches.

MMI advantages

Compared with other types of optical power splitters, MMI devices present several advantages. Their operation is based purely on geometrical modal interference, not on resonant or interferometric effects, which means that they exhibit low wavelength sensitivity, polarization independence, and high fabrication tolerance. Additionally, MMI devices have a simple geometry and can be easily fabricated with standard lithography processes without requiring critical alignment or long interferometric arms or very small resolution.

The design of an MMI coupler generally involves defining the multimode section width and length to achieve the desired imaging condition. For a 1×2 splitter, the first two self-images occur approximately at $3L_\pi/8$ and $5L_\pi/8$. Where L_π is the beat length of the multimode waveguide, defined as the propagation distance over which the phase difference between the fundamental and first-order modes equals π. The total device length LMMI is typically chosen close to $3L_\pi/8$, which provides equal power distribution between the two outputs. The output waveguides are positioned symmetrically at the locations where the two self-images are formed. Because of their geometrical nature, these devices remain effective across a wide spectral range (typically 1300–1650 nm) and for both TE and TM polarizations.

MMI applications

To realize switching functionality, the MMI structure can be combined with active tuning mechanisms. The most common approach is the thermo-optic effect, where micro-heaters are placed above the multimode region or near one of the output arms. By locally increasing the temperature, the refractive index in that region changes, slightly altering the phase relation between the propagating modes [37] [38]. This results in a shift of the self-imaging pattern, allowing light to be directed preferentially toward one output port. The switching speed is determined by the thermal response time, which typically ranges from tens to hundreds of microseconds, depending on the device size and heater design.

In addition to thermo-optic tuning, electro-optic modulation can also be used for MMI switches. This can be achieved by embedding doped p–n junctions within the multimode region or integrating an active material, such as graphene, on the surface of the waveguide. This enables electro-absorption and electro-refraction effects that can control light intensity and phase within the MMI section. [39]

In this thesis, a Mach-Zehnder switch which consist of a 1×2 and 2×2 MMI has been designed as one of the key building blocks of the optical switch matrix. The device combines the multimode interference principle with active tuning based on thermo-optic effects. By controlling the refractive index locally within the multimode section, it is possible to redistribute the optical power between the two output arms, achieving broadband, compact, and low-power switching. This design provides a reliable and fabrication-tolerant solution for integration in silicon photonic platforms, suitable for next-generation reconfigurable optical networks.

2.5 Ring resonator switch

Ring resonators are widely used in integrated photonics because they are compact, wavelength selective, and very sensitive to changes in refractive index. These characteristics make them suitable for filtering, routing, and switching optical signals within a small chip area. Because the optical response of a ring strongly depends on its resonance condition, even a small refractive-index change can shift the resonance wavelength and redirect the light. This allows efficient optical switching with relatively low power consumption and makes ring resonators attractive for highly integrated and reconfigurable photonic circuits.

2.5.1 Theory

A ring resonator consists of a closed-loop waveguide evanescently coupled to a straight bus waveguide. When the effective optical path length of the ring satisfies the resonance condition:

$$m\lambda = n_{eff} L \tag{2.6}$$

Where, m is the resonance order, n_{eff} is the effective refractive index of the guided mode, and L is the physical round-trip length of the ring resonator.

The circulating optical field in the ring constructively interferes with itself, leading to strong resonance and the appearance of characteristic dips or peaks in the transmission spectrum at the output port, as shown in Fig. 6. Small variations in the effective refractive index n_{eff} of the ring or in the coupling

coefficient between the ring and the bus waveguide shift the resonance wavelength and modify the transmission. This property makes ring resonators effective building blocks for modulators, filters, and optical switches.

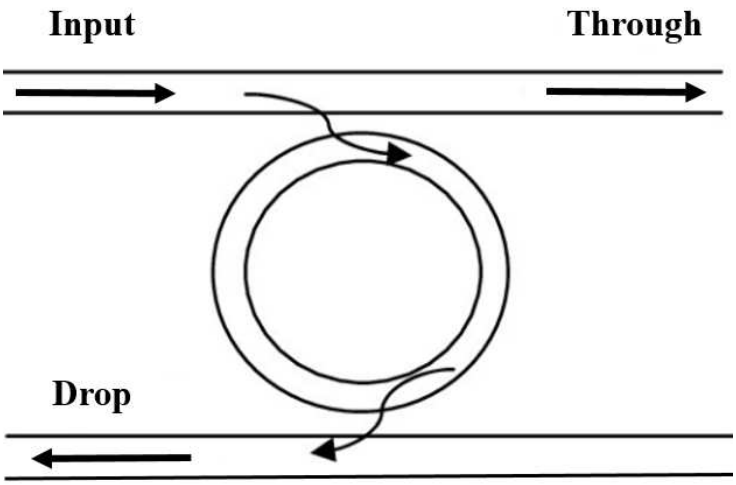

Figure 6. Schematic of a microring resonator coupled to bus waveguides, showing the input signal, the through port for non-resonant wavelengths, and the drop port where resonant wavelengths are extracted.

2.5.2 Application

Ring resonators therefore play a significant role in photonic switching applications. By modifying the effective refractive index of the ring waveguide, for example through thermal tuning using integrated heaters or through electrical control mechanisms such as carrier injection or depletion, the resonance condition of the ring can be dynamically shifted. This change alters the spectral position of the resonance and redistributes the optical power between the through and drop ports. Consequently, the device can be switched between different output states in a controlled manner. This tunability enables ring resonators to act as compact and energy-efficient optical switches, where signal routing is achieved through refractive-index modulation rather than physical reconfiguration of the photonic circuit.

Graphene can also add an additional degree of freedom to this structure because its optical properties are electrically tunable. When a voltage is applied to a graphene layer, the Fermi level shifts, leading to a change in its complex optical conductivity. These changes directly influence both the absorption (imaginary part of the refractive index) and the phase response (real part of the refractive index). As a result, integrating graphene with a ring resonator allows dynamic control of the resonant wavelength and the transmission at the output ports.

2.6 Graphene material

In the proposed devices, graphene has been proposed as the active material in a high-speed electro-absorption modulator and in a silicon electro-optic micro ring switch incorporating a graphene modulation layer. Therefore, to provide a clear understanding of the physical principles behind these devices, the theoretical background of graphene and its optical properties is presented in the following

section.

Graphene is a two-dimensional allotrope of carbon formed by a single atomic layer of carbon (Ca) atoms arranged in a honeycomb lattice. [40] It was first obtained in 2004 through mechanical exfoliation of the graphite by the two scientists Geim and Novoselov [41] that won the Nobel Prize in 2010 for their findings. Each C atom has three σ-bond shared with three nearest atoms (the length of the bonds is about (0.142nm) laying on a plane and π orbital perpendicular to the sheet (Fig. 7). The π orbitals hybridize together to form bands where electrons are free to move free-moving electrons, providing to Gr notable electronic properties.

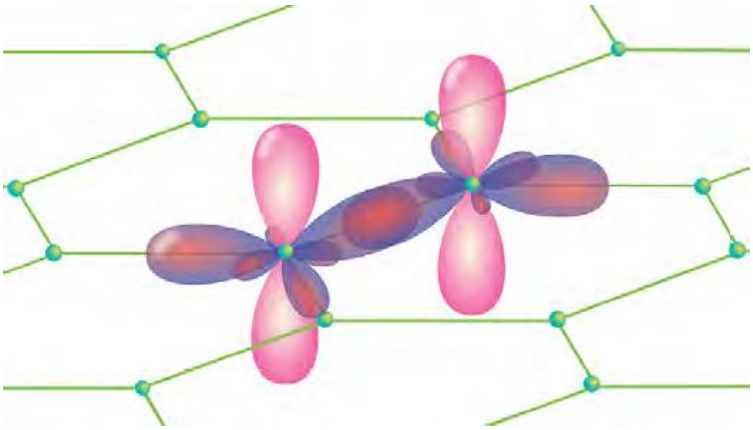

Figure 7. σ-bonds are arranged on the sheet's plane, conversely π bonds are perpendicular to the plane

After some consideration regarding the atomic bonds the energy dispersion relation (2.7) is obtained from the diagonalization of the Hamiltonian (Fig. 8): [42]

$$E(k) = \pm\gamma_0\sqrt{1+4\cos^2\frac{1}{2}\alpha k_y + 4\cos\frac{1}{2}\alpha k_y \cos\frac{\sqrt{3}}{2}\alpha k_z} \tag{2.7}$$

Where γ0 = 2.8 eV is the hopping energy and α = 0.246nm is the lattice constant.

The electronic band structure of graphene can be derived from the tight-binding model. The conduction and valence bands touch at specific points in the Brillouin zone, called Dirac points, located at the corners of the hexagonal lattice. By developing the expression (44) for allowed momenta k in this point, a linear dependence of the energy from the momentum is obtained: [43]

$$E_{\pm}(\delta k) = \pm\hbar v_F \left|\delta K\right| \tag{2.8}$$

Where $\hbar$ is the reduced Planck constant and $v_F \approx 106$m/s is the Fermi velocity. This linear dispersion produces carriers that behave as massless Dirac fermions, leading to extremely high carrier mobility and ultrafast response. The conical energy structure, illustrated in Fig. 8, explains graphene's unique electronic behavior and its ability to operate efficiently at high frequencies.

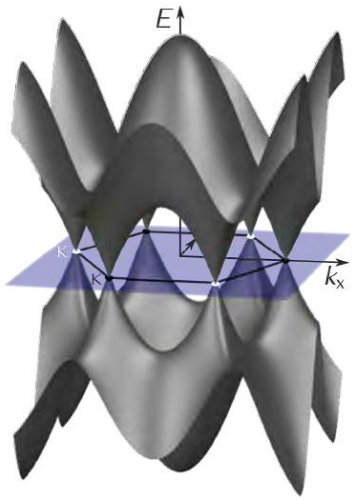

Figure 8. Energy dispersion near the Dirac points showing linear E–k relation. (Reproduced from [42]).

.Despite being only one atom thick, graphene exhibits strong and broadband optical absorption. A single layer absorbs about 2.3% of incident light across the visible and infrared regions, corresponding to a transmittance of approximately 97.7%, which is determined by the fine-structure constant $a = e^2/\hbar c$. This constant absorption results from its gapless band structure, which allows continuous interband transitions. The optical conductivity of graphene is the sum of intraband and interband contributions: [44]

$$\sigma(\omega,\Gamma,\mu_c,T) = \sigma_{\text{intra}}(\omega,\Gamma,\mu_c,T) + \sigma_{\text{inter}}(\omega,\Gamma,\mu_c,T) \tag{2.9}$$

with:

$$\sigma_{\text{intra}}(\omega,\Gamma,\mu_c,T) = \frac{-ie^2}{\pi\hbar^2(\omega+i2\Gamma)}\int_0^\infty \xi\left(\frac{\partial f_d(\xi)}{d\xi} - \frac{\partial f_d(-\xi)}{d\xi}\right)d\xi \tag{2.10}$$

$$\sigma_{\text{inter}}(\omega,\Gamma,\mu_c,T) = \frac{ie^2(\omega+i2\Gamma)}{\pi\hbar^2}\int_0^\infty \frac{f_d(-\xi)-f_d(\xi)}{(\omega+i2\Gamma)^2-4(\xi/\hbar)^2}d\xi \tag{2.11}$$

Where:

ω: angular frequency;

Γ: scattering rate;

μ_c: chemical potential;

T: temperature;

e: electronc charge;

h: reduced plank constant;

k_B: Boltzmann constant;

And

$$f_d(\xi) \equiv \frac{1}{exp((\xi - \mu_c)/(k_B T)) + 1} \tag{2.12}$$

Is also the Fermi Dirac distribution.

Both intraband and interband components depend on the Fermi–Dirac distribution and can be modified by electrical gating or chemical doping, allowing dynamic control of the optical response. This tunability is at the core of graphene-based modulators and switches. When a voltage is applied, the Fermi level shifts, altering the probability of optical transitions between the valence and conduction bands. As illustrated in Fig. 9, when $h\nu < 2|\mu_c|$ the absorption is suppressed due to Pauli blocking, while for $h\nu > 2|\mu_c|$ strong interband absorption occurs. By adjusting the gate voltage, it is therefore possible to control the absorption and transmission of light in graphene, enabling electro-absorption modulation.

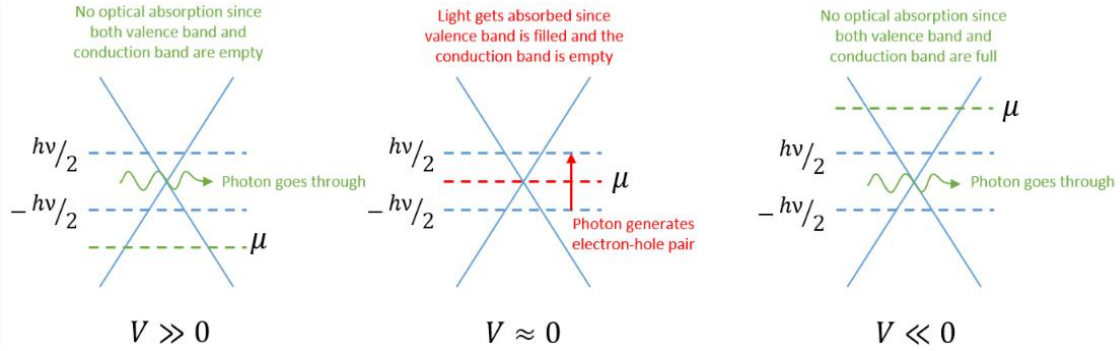

Figure 9. Modulation in graphene's optical absorption with applied bias voltage.

The Fermi level shift is given by (2.13): [45]

$$\mu_c = \mathrm{sgn}(n)\hbar v_F \sqrt{\pi |n|} \tag{2.13}$$

Where n is the carrier density controlled by the applied voltage. This voltage-dependent optical absorption forms the basis for graphene modulators and graphene-assisted switches, allowing compact and broadband electro-optic control.

2.6.1 Graphene applications

The integration of graphene with silicon photonics has become an important approach for developing compact, high-speed, and energy-efficient optical devices. Graphene offers unique advantages such as electrically tunable conductivity, ultrafast carrier dynamics, broadband optical response, and compatibility with CMOS fabrication. When combined with silicon waveguides, these properties enable a new class of active photonic components that cannot be achieved with silicon alone.

Graphene has been successfully employed in several key photonic applications. Examples include graphene-based electro-absorption modulators, electro-refractive phase modulators, high-speed photodetectors, optical switches, ring resonator modulators, and Mach–Zehnder interferometers with graphene heaters. Additionally, structures such as graphene/insulator/graphene (GIG) capacitors

provide strong electrostatic control over the Fermi level and are used for high-speed modulation and tunable absorption. Graphene has also been used in plasmonic modulators, broadband absorbers, optical sensors, and tunable filters due to its large optical nonlinearity and controllable refractive index.

In this thesis, these capabilities of graphene are exploited to design and study graphene-based optical switches and modulators integrated on a silicon platform, where graphene acts as the active layer enabling fast and efficient electro-optic control.

2.7 Graphene based capacitor

2.7.1 Monolayer of graphene

A monolayer graphene based capacitor takes advantage of the exceptional electronic properties of graphene to achieve fast, compact, and highly tunable electro optic functionality. In this structure, a single graphene sheet is placed over a dielectric layer and paired with a metal or graphene counter electrode to form a parallel plate capacitor. When an external voltage is applied, the carrier concentration in the graphene changes and the Fermi level shifts. This shift directly modifies graphene's surface conductivity and both the real and imaginary parts of its refractive index.

Compared to conventional semiconductor capacitors, monolayer graphene capacitors benefit from very high carrier mobility, wide electrostatic tunability, and ultrafast electrical response due to the two dimensional nature of graphene. They also exhibit quantum capacitance effects at low carrier densities, which provide an additional level of control over the electrical and optical behavior of the device. These characteristics make monolayer graphene capacitors suitable for high speed electro optic modulators, tunable absorbers, and compact photonic switches.

2.7.2 Multi-layer graphene (MLG)

Compared to standard metal oxide semiconductor capacitors, GIG structures offer several advantages, including lower driving voltage, faster response, and excellent compatibility with silicon photonic platforms. Their planar and transparent design makes them particularly well suited for integration on top of optical waveguides, where graphene can strongly interact with the guided optical mode. For these reasons, GIG capacitors are widely considered promising building blocks for next generation electro optic modulators, photonic switches, active filters, and reconfigurable optical circuits.

Materials with high k dielectrics such as TiO_2, Al_2O_3, or HfO_2 are commonly used to maximize the geometric capacitance and ensure low leakage current. Thin films, typically 5–20 nm thick, are deposited by thermal evaporation or atomic layer deposition (ALD) to achieve good uniformity and interface quality without damaging the graphene. The resulting capacitors are characterized through capacitance–voltage (C–V) measurements, which allow the extraction of the quantum capacitance and the corresponding Fermi level as a function of the applied voltage.

Unlike conventional capacitors, the total capacitance of a GIG structure is influenced by both the dielectric material and the finite density of electronic states in graphene. The total capacitance (C_{total})

is given by the series combination of the geometric capacitance of the dielectric (C_{geom}) and the quantum capacitances ($C_{Q,top}$) and ($C_{Q,bottom}$) of the two graphene layers: [46]

$$\frac{1}{C_{total}} = \frac{1}{C_{geom}} + \frac{1}{C_{Q,top}} + \frac{1}{C_{Q,bottom}} \tag{2.14}$$

The geometric capacitance depends on the dielectric thickness and permittivity:

$$C_{geom} = \frac{\varepsilon_0 \varepsilon_r A}{d} \tag{2.15}$$

Where ε_0 is the vacuum permittivity, ε_r the relative dielectric constant, A is the capacitor area, and d is the dielectric thickness.

2.7.3 Quantum Capacitance

Another important property is the quantum capacitance, which represents the variation of electrical charge ρ in respect of the electrochemical potential:

$$C_Q = \frac{d\rho}{dE_F} \tag{2.16}$$

Where ρ=e(p - n) and E_F is the Fermi level. The quantum capacitance can also be expressed as: [47]

$$C_Q = \frac{2e^2 k_B T}{\pi(\hbar \nu F)^2} \ln\left[2(1+\cosh\frac{eV_{ch}}{k_B T})\right] \tag{2.17}$$

Where $V_{ch} = E_F/e$ is the potential of graphene. When $eV_{ch} >> k_B T$, equation reduces to:

$$C_Q = \frac{2e^2 |E_F|}{\pi(\hbar \nu_F)^2} \tag{2.18}$$

The quantum capacitance of graphene reaches its minimum value near the Dirac point, where the density of states is very low, and increases almost linearly with the channel voltage (V_{ch}) as the Fermi level moves away from this point, with a slope of about 23 $\mu F \cdot cm^{-2} \cdot V^{-1}$. This behavior is symmetric around the Dirac point and plays an important role in defining the electrostatic properties, modulation depth, and speed of graphene-based electronic and photonic devices.

2.7.4 Graphene-based modulators

An optical modulator is a device that is used to modulate a steady light wave beam, propagating either in free space or along an optical waveguide [48]. These devices can modify one or more parameters of the optical beam, falling into different categories such as amplitude, phase or polarization

modulators [49]. Moreover, they can be classified as either electro-refractive or electro-absorbing, depending on whether variation of the real part or of the imaginary part of the refractive index is exploited [50]. Being insensitive to wavelength, electro-absorption (EA) waveguide-coupled modulators, with their ultra-high speed, low-drive voltage, and hysteresis-free operation, may play a crucial role in next-generation optical transceivers. [51]

On the other hand, Graphene, with its high carrier mobility and broadband absorption characteristics, shows interesting and promising physical attitudes in enabling the design of extremely fast, compact and wide-bandwidth electro-optic devices [52]. The development of Gr-based modulators started with Liu et al. [53], who reported an electro-absorption (EA) modulator exploring a single layer of Gr (SLG) on top of a Si-waveguide achieving a modulation depth of 0.1 dB/μm and an optical bandwidth of 1.2 GHz. Subsequently, Dalir et al. demonstrated a TM mode in planar structure-integrated modulators, with a double-layer of Graphene (DLG), achieving a bandwidth of 35 GHz and a small footprint of 18μm^2; however, high contact resistance and high driving voltage have been estimated [54]. Fan et al. proposed a Gr-based EA modulator based on a double-stripe silicon nitride (SiN) waveguide [55]. By embedding two Gr-on-Gr (GOG) layers inside the double-stripe SiN waveguide, and by properly designing the electrodes, the total metal-Gr contact resistance was highly reduced leading to a theoretical modulation bandwidth of 30 GHz. The calculated extinction ratio was estimated to be 0.165 dB/μm.

Giambra et al. reported a C-band DLG EA modulator on a passive Silicon-on-insulator (SOI) platform showing 29 GHz 3dB-bandwith and extinction ratios ranging from 1.7 dB at 10 Gb/s to 1.3 dB at 50 Gb/s [56]. The total length was 120μm. The fabrication method was CMOS-compatible, demonstrating how Gr technology can meet the highest performances required by the market.

A similar concept was proposed in [57], where a stack composed of hydrogenated amorphous Silicon (a-Si:H), DLG, and crystal Silicon (c-Si) was considered for the waveguiding-core, with two (hexagonal Boron Nitride)-Graphene-(hexagonal Boron Nitride), h-BN−Gr−h-BN, stacks separated by a layer of Hafnium Oxide (HfO_2) as dielectric for the DGL capacitor. The modulation speed was estimated by simple calculations of the RC constant of the device, leading to an optimistic bandwidth in excess of 150 GHz for a high-k dielectric spacer between the Gr plates. A Gr capacitor-embedded waveguide-integrated modulator was also reported in [58].

2.8 Thermo-optic and electro-optic effects

In the design of the proposed switches, two main theoretical concepts are primarily employed: the electro-optic and thermo-optic effects. These mechanisms enable both optical switching and modulation within the developed devices.

2.8.1 Thermo-optic effect

The thermo-optic effect describes the change of a material's refractive index as a function of temperature. When the temperature of a medium varies, its electronic Polarizability and lattice parameters are modified, leading to a measurable change in its optical properties. The dependence of the refractive index on temperature can be expressed as: [59]

$$n(T) = n_0 + (\frac{dn}{dT})(T - T_0) \quad (2.19)$$

Where n(T) is the refractive index at temperature T, n_0 is the refractive index at a reference temperature T_0 and $\frac{dn}{dT}$ is the thermo-optic coefficient.

For most dielectric and semiconductor materials, this coefficient is positive, meaning that the refractive index increases with temperature. Crystalline silicon has a relatively large thermo-optic coefficient, approximately 1.86×10^{-4} K^{-1} at the wavelength of 1.55 μm, which is nearly twenty times higher than that of silica (≈ 1×10^{-5} K^{-1}). [60] This strong dependence makes silicon particularly suitable for thermo-optic modulation and switching in integrated photonics.

In integrated photonic devices, the thermo-optic effect is exploited to control light propagation by locally modifying the refractive index. This is usually achieved through metallic micro-heaters placed above or beside the optical waveguide. When current flows through the heater, Joule heating produces a local temperature rise, which changes the refractive index of the waveguide core and therefore the optical path of the guided mode. The induced phase shift can be expressed as:

$$\Delta\phi = \frac{2\pi L}{\lambda}(\frac{dn_{eff}}{dT})\Delta T \quad (2.20)$$

Where L is the length of the heated portion of the waveguide, λ is the operating wavelength, and ΔT is the temperature difference between the heated region and the ambient. [61]

The response time of the thermo-optic effect is influenced by thermal diffusion, typically ranging from a few tens to hundreds of microseconds. Although slower than electro-optic modulation, this mechanism provides broadband operation, high stability, and low wavelength sensitivity, which are essential for optical switches, variable couplers, and filters. The achievable refractive-index variation in silicon is on the order of 10^{-3} for a temperature change of about 10 – 20 K, which is sufficient to enable efficient optical switching in compact devices.

Due to its simplicity and stability, the thermo-optic effect is one of the most reliable mechanisms in silicon photonics. It does not require complex doping profiles or special materials and is fully compatible with standard CMOS fabrication. By optimizing heater geometry, thermal isolation, and waveguide design, thermo-optic devices can achieve low power consumption and stable performance, making them ideal for reconfigurable optical networks and integrated switching systems.

2.8.2 Electro-optic effect

The electro-optic effect describes the variation of the refractive index of a material when an external electric field is applied. The electric field interacts with the electronic distribution of the atoms, producing a distortion in the dielectric constant of the material. As a result, both the real and imaginary parts of the refractive index are modified, allowing the control of the phase and the amplitude of the propagating optical wave.

The relation between the change in the refractive index and the applied electric field can be expressed,

generally, through the modification of the optical impermeability tensor as: [62]

$$\Delta(\frac{1}{n^2})_{ij} = \sum r_{ijk} E_k \tag{2.21}$$

Where n is the refractive index of the medium, r_{ijk} the electro-optic tensor coefficient, and E_k is the applied electric-field component. This equation represents the linear electro-optic effect, also known as the Pockels effect, in which the change in the refractive index is directly proportional to the applied electric field. For a given propagation direction, this can be simplified as (2.22):

$$\Delta n = \frac{1}{2} n^3 r E \tag{2.22}$$

Where r is the effective electro-optic coefficient. This effect occurs only in materials without inversion symmetry, such as lithium niobate ($LiNbO_3$), gallium arsenide (GaAs), and other III–V or ferroelectric compounds.

In materials exhibiting inversion symmetry, such as crystalline silicon or silica, the linear term is absent, and the quadratic electro-optic effect, or Kerr effect, becomes dominant. In this case, the refractive-index variation depends on the square of the applied electric field and can be written as (2.23):

$$\Delta n = \frac{1}{2} n^3 K E^2 \tag{2.23}$$

Where K is the Kerr constant of the material. Although it is weaker than the Pockels effect, the Kerr effect can still produce measurable modulation under strong electric fields and is often used in combination with other mechanisms in integrated devices.

The most commonly used EO effect in silicon is by far the free-carrier dispersion. Since crystalline silicon is a centrosymmetric material and does not exhibit a linear Pockels effect, modulation of its optical properties is mainly achieved by varying the concentration of free electrons and holes. As described by Soref and Bennett [62], changes in carrier density modify both the real and imaginary parts of the refractive index through free-carrier absorption, band filling, and plasma effects. At telecommunication wavelengths, these carrier-induced refractive-index variations are sufficiently strong to enable efficient electro-optic modulation, making free-carrier dispersion the fundamental mechanism underlying silicon-based modulators, phase shifters, and optical switches.

In addition to these classical mechanisms, materials such as graphene or other two-dimensional semiconductors can be used, as already seen, to modify both the refractive index and optical absorption of a silicon waveguiding region. This enables simultaneous phase and amplitude modulation of the optical signal within the same structure, providing a strong and broadband electro-optic response.

The electro-optic effect, in all its forms, provides the physical foundation for the operation of optical modulators and switches. It allows the refractive index of the waveguide to be controlled by an electrical signal, enabling high-speed and efficient modulation of light in integrated photonic systems.

3. Manufacture process

3.1 Clean room facility

The fabrication work presented in this thesis was carried out in the Micro–Nano Fabrication Laboratory (µNF Lab) at ISASI–CNR, Naples, shown in Fig. 10. The facility is a modern cleanroom environment equipped for the development of Micro-scale and Nano-scale photonic, optoelectronic, and microelectronic devices. The laboratory operates at ISO 5–7 cleanliness levels and provides all the necessary tools for wafer processing, device prototyping, and material deposition.

Figure 10. Micro–Nano Fabrication Laboratory (µNF Lab) at ISASI–CNR, Naples.

The Micro-Nano Fabrication Laboratory (µNF Lab) is organized into three main technological areas including Thin Film Lab, Wet Process Lab, and Optical Lithography Lab which covers the full process step that are required for integrated photonic device fabrication. The Thin Film Lab hosts PECVD systems for a-Si:H and dielectric deposition, sputtering and evaporation tools for metallization, and ICP-RIE and DRIE systems for deep silicon etching. The Wet Process Lab is dedicated to RCA cleaning, wet etching, and lift-off steps. The Optical Lithography Lab includes a Karl Suss MA6 mask aligner and a high-resolution ML3 BabyPlus laser writer, enabling maskless photolithography down to the sub-micrometer scale. Together, these facilities provided all the fabrication steps required for this work, including thin-film deposition, photolithography, dry etching, metallization, and post-processing, enabling the realization of the silicon photonic switches and graphene-based devices discussed in this thesis.

3.2 Fabrication steps

In this section, the fabrication methods and procedures used to realize the designed photonic devices are described in detail. The discussion includes the equipment utilized and the detailed fabrication steps followed for different structures such as Mach–Zehnder interferometers, multimode interference (MMI) switches, graphene-based modulators, adiabatic switches, and other related devices developed during this work.

3.2.1 Photolithography

The photolithography process was one of the most important fabrication steps for the realization of the integrated photonic devices, including the multimode interference (MMI) switch and other optical structures developed in our cleanroom facility. All processes were carried out on silicon-on-insulator (SOI) wafers using a direct-write laser lithography system and standard cleanroom techniques to define the optical waveguides and device geometries with micrometer precision. The individual steps of this process are reviewed in the following section.

3.2.1.1 Wafer Preparation and Cleaning

The fabrication process of the integrated photonic devices, including the multimode interference (MMI) switch and other optical components, was carried out on silicon-on-insulator (SOI) wafers. The SOI wafers used in this work consisted of a 1.5µm silicon device layer on top of a 2 µm buried oxide (BOX) layer. The wafers were first diced into smaller pieces suitable for processing and then cleaned to remove all surface contaminants and residues.

The cleaning process followed a standard RCA procedure to prepare the wafer surface before lithography and etching. First, the wafers were cleaned using a piranha solution (a mixture of H_2SO_4 and H_2O_2 in a 3:1 ratio) at 90°C to remove any organic dirt or residue. After rinsing the samples with deionized (DI) water, they were placed in an SC1 solution (NH_4OH:H_2O_2:H_2O in a 1:1:5 ratio), which helps remove small particles and some metallic impurities.

Next, a short HF dip (1–2% hydrofluoric acid) was performed to remove the thin oxide layer created during the previous steps with hydrogen termination. To remove any remaining metal ions, the wafers were then placed in an SC2 solution (HCl:H_2O_2:H_2O in a 1:1:6 ratio), which effectively cleans away transition metal contaminants. Finally, another quick HF dip was carried out to ensure a clean, smooth, and hydrophobic silicon surface. This careful cleaning sequence ensured that the wafers were completely free of organic, metallic, and particulate contaminants, making them ready for high-quality lithography and etching steps.

3.2.1.2 Adhesion and Photoresist Coating

To promote proper adhesion between the photoresist and the silicon surface, a thin layer of HMDS (Hexamethyldisilazane) was spin-coated at 5000 rpm for 60 seconds as it is shown in Fig. 11. Immediately after, a positive photoresist (FujiFilm OIR 906-12) was applied using the same spin speed and duration, forming a uniform layer of approximately 1.3 µm in thickness.

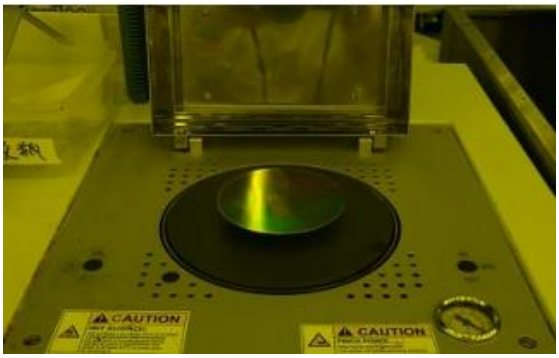

Figure 11. Spin coater used for photoresist coating (Karl Suss Delta 80 model). The system distributes the photoresist uniformly on the wafer surface through controlled high-speed rotation.

The coated wafer was placed on a hotplate and soft-baked at 90 °C for one minute to evaporate residual solvent and stabilize the resist layer. Figure. 12 illustrates the different baking systems that can be used during wafer processing, including hot plates, convection ovens, and microwave ovens.

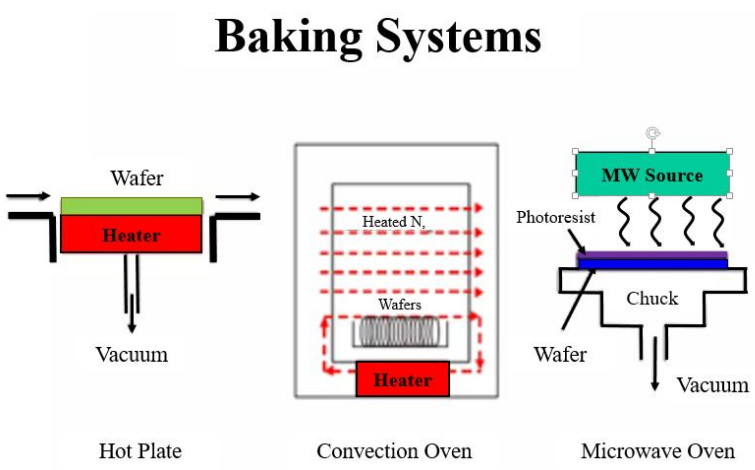

Figure 12. Different baking systems used for wafer processing, including a hot plate, convection oven, and microwave oven, employed for photoresist soft-bake and hard-bake steps during photolithography.

The photosensitive materials used in lithography are generally divided into two categories: positive and negative photoresists. (Fig. 13) In a positive photoresist, the areas exposed to light become soluble and are removed during the development process. Therefore, light is exposed around the waveguide so that the waveguide itself remains on the substrate. In contrast, in a negative photoresist, the areas exposed to light harden and remain after development. In this case, light must be shone directly on the waveguide region so that the surrounding areas are removed while the waveguide pattern stays undamaged.

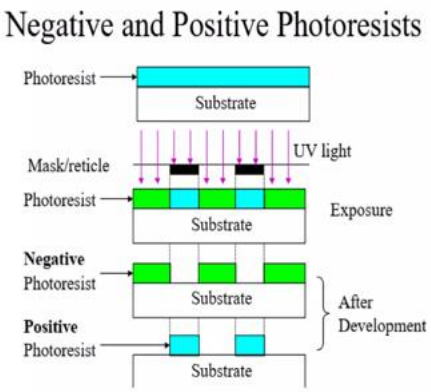

Figure 13. Schematic illustration showing the difference between negative and positive photoresists in the photolithography process. In positive resists, the exposed regions are removed during development, whereas in negative resists, the exposed areas remain after development.

3.2.1.3 Exposure Process (Mask Aligner and Laser Writer)

After coating and baking, the photoresist was exposed to ultraviolet light to define the photonic structures [63]. Depending on the pattern complexity and size, two different exposure techniques were used: mask aligner lithography and direct-write laser lithography.

a) Mask Aligner Exposure

As it can be seen in Fig. 14 the Karl Suss MA6 mask aligner was used for exposing large or repeated patterns which includes reference marks and electrical contact regions. The mask aligner allows precise alignment between the mask and wafer using microscope alignment systems with UV light at wavelength of 365 nm. The exposure dose was normally set between 100–150 mJ/cm² in hard-contact mode to achieve sharp pattern edges.

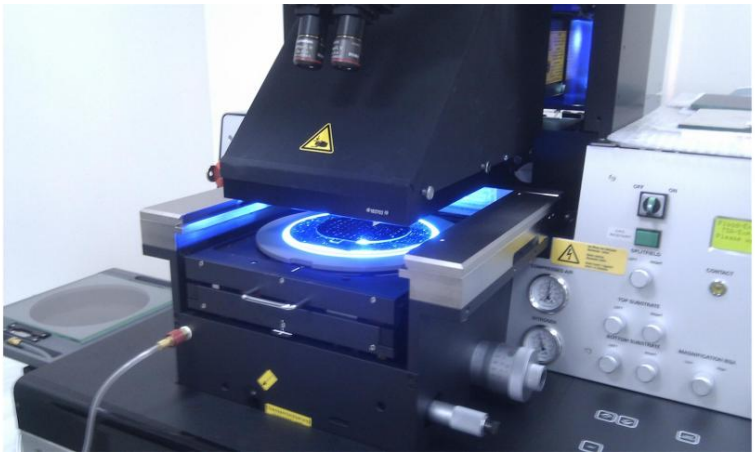

Figure 14. The Karl Suss MA6 mask aligner system. That has been used for exposure process.

b) Laser Direct-Write Lithography

For small and detailed structures such as waveguides, MMI regions, and adiabatic tapers, a laser writer system (MicroWriter ML3 Baby Plus – Quantum Design) was used, as shown in Fig. 15. This system enables Maskless lithography, directly writing digital patterns onto the photoresist using a focused UV laser beam. The technique allows high-precision patterning and rapid prototyping, achieving a resolution of around 1 µm. The resolution of approximately 1 µm is mainly limited by the characteristics of the direct laser writing system and the photoresist used in the fabrication process. In particular, the laser spot size and the diffraction limit define the minimum feature size that can be achieved. In addition, factors such as resist sensitivity, exposure conditions, and development process can further affect the pattern resolution. Achieving sub-micron resolution would require the use of more advanced lithography techniques such as electron-beam lithography, which offer higher resolution but at the expense of longer processing time and higher cost.

To achieve the best lithography results, an optimization procedure was carried out. First, the same structure was written several times on a single sample while varying the laser dose over a wide range to identify the approximate exposure window that produced the clearest features. In the second stage, fine-tuning was performed around this optimal dose to ensure consistent feature definition and reliable pattern transfer. Once the ideal exposure parameters were identified, the process was fixed, and lithography was successfully performed on the actual sample. After confirming the pattern accuracy, we proceeded to the next fabrication steps.

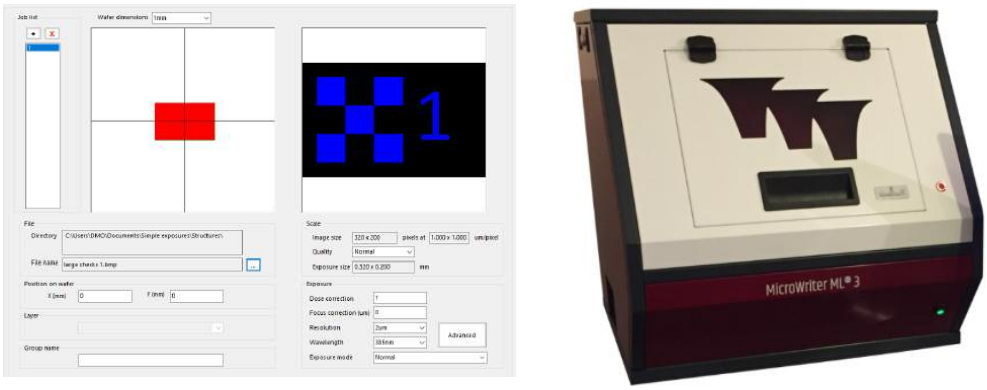

Figure 15. MicroWriter ML3 BabyPlus (Quantum Design) direct laser writing system and corresponding software interface used for maskless photolithography and pattern design during device fabrication.

3.2.1.4 Hard Bake

After exposure, a hard bake was performed on the wafer at 110 °C for 1 minute to stabilize the pattern. (Fig. 16) This bake increase the mechanical strength of the photoresist and enhance its resistance during the etching process. This also helps to improve adhesion between the resist and substrate and prevents peeling or deformation during plasma exposure.

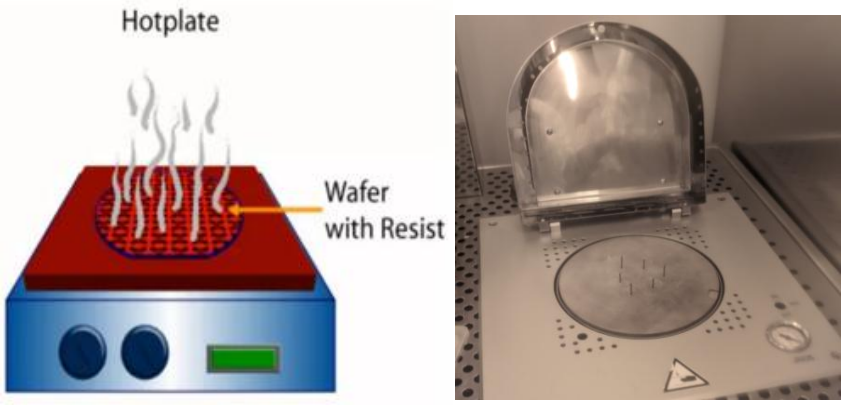

Figure 16. Hotplate system used for soft-bake and hard-bake processes during photolithography.

3.2.1.5. Development

Following exposure, the wafer was developed in OPD 4260 developer solution for 45 – 60 seconds, depending on the resist thickness and laser exposure dose. During this step, the exposed regions of the positive resist were dissolved, leaving the protected areas intact and forming the required photonic structures on the wafer. (Fig. 17)

The wafer was then rinsed in deionized water for 30 seconds and dried with nitrogen gas. Optical microscopy inspection was carried out after development to confirm the completeness of the pattern and ensure there were no residues or unexposed areas remaining.

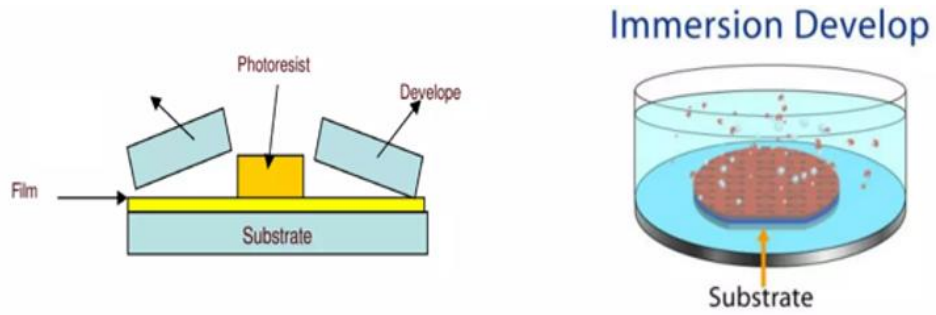

Figure 17. Illustration of the development step in the photolithography process.

3.2.1.6. Etching Process (Wet and Dry Etching)

After the lithography step, the next stage was to transfer the patterned design into the silicon device layer using the etching process. The basic principle of this process is illustrated in Fig. 18. Depending on the material and required precision, both wet and dry etching techniques were used.

a) Wet Etching

Wet etching was mainly used to remove oxide layers or to clean the surface before the deposition

steps. In this process, the samples were immersed in a Buffered Oxide Etchant (BOE) or hydrofluoric acid (HF) solution, which selectively dissolves the SiO_2 layer without damaging the underlying silicon. This method is isotropic, meaning that it etches in all directions equally, providing good uniformity over large surfaces but with limited control near edges due to possible undercut. After etching, the wafer was thoroughly rinsed in DI water and dried with nitrogen.

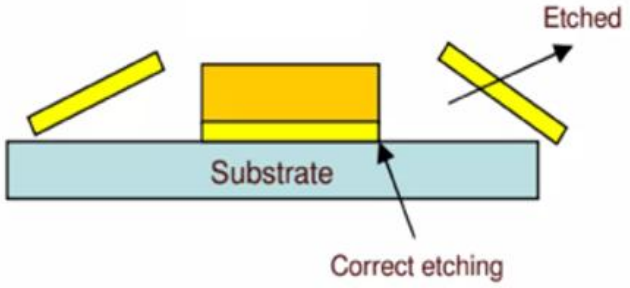

Figure 18. Schematic representation of the etching step in the photolithography process.

b) Dry Etching

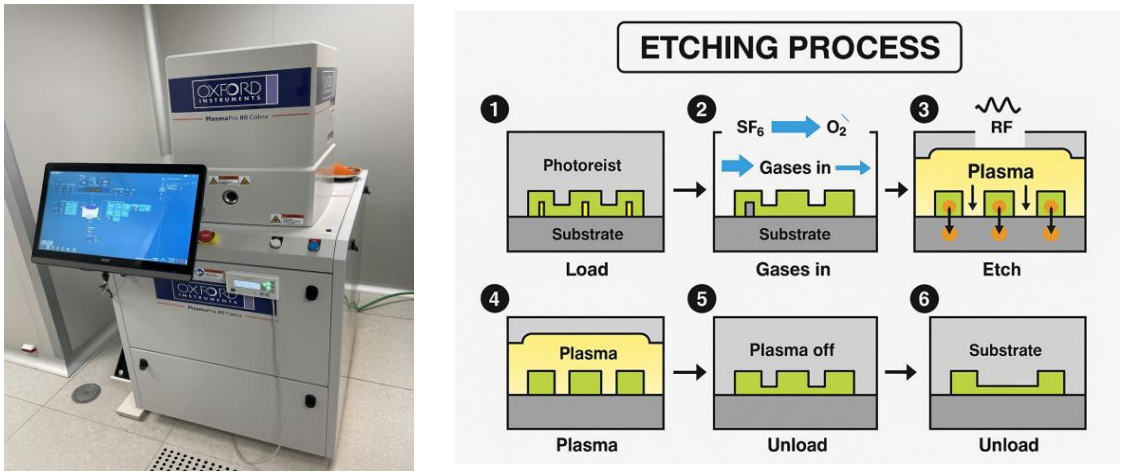

(a) (b)

Figure 19.(a) Oxford PlasmaPro 80 system used for reactive ion etching (RIE), (b) Schematic representation of the dry etching process illustrating the main steps.

For the precise pattern transfer of silicon waveguides and MMI structures, Reactive Ion Etching (RIE) was performed using an Oxford PlasmaPro 80 system as it is shown in Fig. 19.a. In this process, the wafer with the photoresist pattern is placed inside the chamber, and the air is completely removed to create a vacuum then two gases, SF_6 and C_4F_8, are introduced into the chamber. When radio-frequency (RF) power is applied, these gases turn into a plasma that contains energetic ions. The ions move toward the surface of the wafer and remove the unprotected silicon areas. The SF_6 gas helps to chemically etch the silicon, while the C_4F_8 gas creates a thin protective layer on the sides of the structures to keep the edges smooth and vertical. By carefully controlling the gas flow, RF power, and etching time, the process removes only the silicon in the desired regions and stops before reaching the oxide layer. After etching, the plasma was turned off and the chamber was vented. The whole process is shown in Fig. 19.b.

Finally the wafer was cleaned in acetone followed by oxygen plasma to remove any residues and leave smooth, well-defined structures.

3.2.2 Thermal Evaporation

Thermal evaporation is one of the most common and reliable techniques used for depositing thin metallic films in micro- and nanofabrication processes. It is a physical vapor deposition (PVD) method in which the material to be deposited is heated inside a vacuum chamber until it reaches its evaporation temperature. The evaporated atoms travel through the vacuum and condense onto the surface of the substrate, forming a uniform thin film.

This technique is typically used when high-quality metallic layers such as Ti, Cr, Au, or Al are required for electrical contacts, heaters, or reflective coatings. In our fabrication process, thermal evaporation was employed to deposit the metallic layers used as micro-heaters and contact pads for the thermo-optic switches. The method provides good control over the film thickness and purity, and it ensures strong adhesion when followed by an appropriate adhesion layer (for example, titanium beneath gold). The process follows a standard four-step recipe as described below:

Step 1 – Chamber Preparation and Pump-Down

The substrate is mounted on the holder facing the metal source, and the chamber is sealed. The vacuum pump is started, and the pressure is reduced to about 10^{-6} mbar. Achieving high vacuum is essential to prevent contamination and ensure that the evaporated atoms travel freely to the substrate without hitting with gas molecules.

Step 2 – Source Heating and Stabilization

The source material (for example, titanium or gold pellets) is placed in a tungsten boat or boat with other material depending on the metal source. The deposition thickness and current applying to the boat must be set. A high current is gradually applied to heat the boat through the Joule effect. Once the material begins to evaporate, the deposition rate is monitored using a quartz crystal microbalance (QCM).The current is adjusted to reach the desired deposition rate, typically between 0.1–1 nm/s, and kept stable before starting the deposition.

Step 3 – Film Deposition

When the rate is stable, the shutter is opened to expose the substrate to the vapor flux. The evaporated atoms condense on the surface and form a thin metallic film. The thickness is controlled in real time by the QCM and is adjusted according to the process requirements. In this project, a thin adhesion layer (10 nm nickel) was first deposited, for the pads of electrical contacts of thermo optic switches.

Step 4 – Cool down and Venting

After reaching the target thickness, the shutter is closed and the current is gradually reduced to stop

evaporation. The system is allowed to cool under vacuum to prevent oxidation. Once cooled, the chamber is vented slowly with dry nitrogen, and the samples are removed for further processing, such as lift-off or patterning. Figure. 20.a and b shows thermal evaporation machine and principle process behind of it.

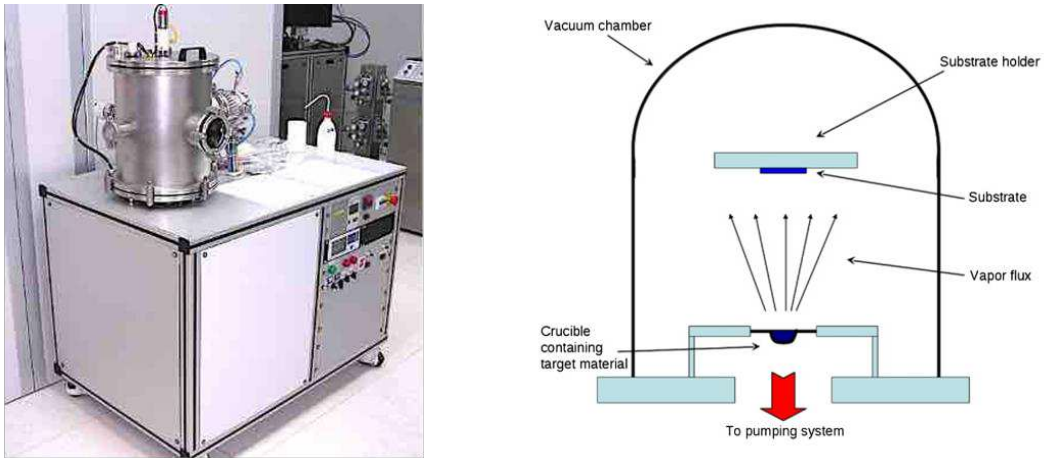

(a) (b)

Figure 20. (a)Thermal evaporation system, (b) schematic diagram of the physical vapor deposition (PVD) process.

3.2.3 Graphene Deposition

For the devices, such as the graphene-based modulator and graphene ring switches, it was essential to understand how a monolayer of graphene can be accurately transferred onto the substrate.

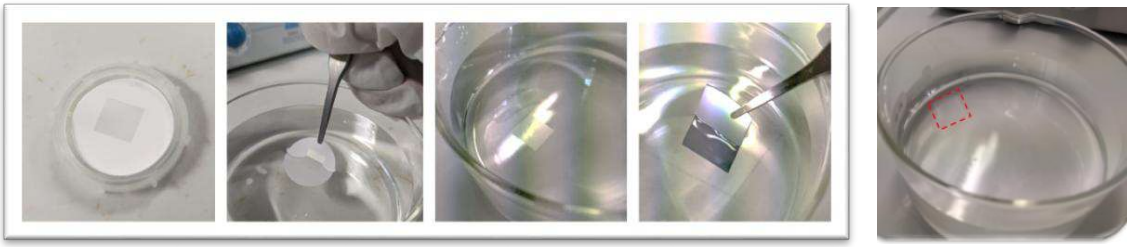

(a) (b) (c) (d) (e)

Figure 21. Steps of the Gr transfer: (a) Gr on the polymer substrate, (b) Immersion of the Gr layer in the DI water, (c) Gr layer floating o the DI water and (d) Gr transfer in the silicon substrate (e)graphene monolayer floating on the water.

The graphene used in this work was supplied by Graphenea Company and provided on a sacrificial substrate with an additional thin polymer protection layer to preserve its structural integrity during handling and transfer. To begin the process, the sample is placed slowly on the surface of deionized (DI) water. The water penetrates between the supporting film and the sacrificial layer, causing the sacrificial layer and graphene to detach from the support. Once released, the graphene/sacrificial layer film floats freely on the water surface.

After the graphene film is floating on the water surface, the target substrate (in our case, the silicon

photonic device) is inserted below the floating graphene and carefully lifted up to catch it from underneath. The substrate is tilted at approximately 45°C during this step to ensure a smooth and bubble-free transformation. The step-by-step process of graphene transfer and deposition is shown in Fig. 21. a to e.

Once the graphene/sacrificial layer is positioned on the substrate, it is allowed to dry naturally in air for about 30 minutes. To improve adhesion, the sample is then annealed at 150 °C for 1 hour on a hotplate. After annealing, the samples are stored under vacuum for at least 24 hours before the next step. This storage step helps remove residual moisture and ensures that the graphene adheres firmly to the substrate, minimizing the risk of delamination during the cleaning process.

The final step is the removal of the sacrificial layer that supported the graphene during transfer. The sample is immersed in hot acetone (≈ 50 °C) for 1 hour to dissolve the sacrificial layer. After that, it is rinsed in isopropyl alcohol (IPA) for another 1 hour to remove any remaining residues. Finally, the sample is dried with nitrogen (N_2).

3.2.4 PECVD

For the deposition of hydrogenated amorphous silicon (a-Si:H) on the fabricated devices, the PlasmaLab 80 system was used, as shown in Fig. 22. The process is based on Plasma Enhanced Chemical Vapor Deposition (PECVD), a widely employed technique for depositing high-quality amorphous silicon and dielectric thin films at relatively low substrate temperatures. PECVD is particularly suitable for photonic and electronic applications because it allows good control of film thickness (few nanometers precision), uniformity, and hydrogen content, while maintaining compatibility with other materials already present on the chip. [64]

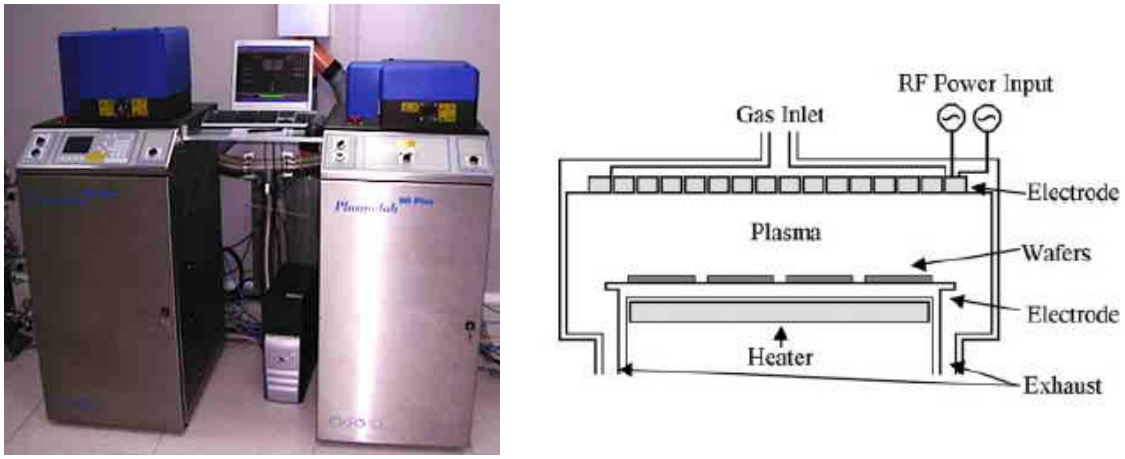

Figure 22. PlasmaLab 80 system by Oxford Instruments and schematic diagram of the PECVD reactor, illustrating the plasma generation, gas flow, and heating configuration used for hydrogenated amorphous silicon (a-Si:H) deposition.

In PECVD, a plasma is generated by applying radio-frequency (RF) power to a low-pressure gas mixture inside a vacuum chamber. The plasma dissociates the precursor gases into reactive species such as radicals and ions, which then deposit onto the substrate surface to form a thin solid film.

For a-Si:H deposition, the main precursor gases are Silane(SiH_4) and hydrogen (H_2). The plasma breaks the Silane molecules into silicon and hydrogen radicals. These radicals react and condense on the substrate surface, forming a silicon network that incorporates a controlled amount of hydrogen. The hydrogen atoms play an important role by passivating the dangling bonds in the amorphous silicon matrix, improving optical quality and reducing defects.

3.2.5 Atomic Force Microscope (AFM)

Atomic Force Microscopy (AFM) is a highly precise technique used to analyze the surface morphology and roughness of fabricated photonic devices. It operates by scanning a sharp probe tip over the sample surface and detecting the interaction forces between the tip and the material. [65] The resulting deflection of the cantilever is measured by a laser beam reflected onto a photodiode, allowing a detailed reconstruction of the surface topography. AFM can operate in several modes depending on the sample properties. In contact mode, the tip remains in constant contact with the surface, providing high-resolution imaging but risking damage to softer materials. In tapping mode, the tip oscillates and briefly touches the surface during scanning, reducing lateral forces and minimizing sample deformation. Finally, in non-contact mode, the tip oscillates close to the surface without direct contact, using weak attractive forces to map the topography while preserving both the probe and the sample.

In this work, AFM was employed to characterize the surface thickness quality of the fabricated silicon photonic structures, including etched waveguides and deposited thin films. The measurements provided essential information about surface uniformity and fabrication precision, helping to optimize etching and deposition parameters for improved optical performance.

3.2.6 Scanning Electron Microscope (SEM)

The Scanning Electron Microscope (SEM) is used to obtain high-resolution images of the surface and cross-sectional structures of fabricated photonic devices. It works by scanning a focused beam of electrons over the sample surface and detecting the emitted signals to form detailed images. SEM allows precise inspection of waveguide profiles, etch quality, and surface morphology, which are essential for verifying fabrication accuracy. In addition, it helps identify fabrication defects such as sidewall roughness or residue from lithography. The information obtained from SEM analysis is crucial for optimizing process parameters and improving device performance.

4. Device concept and simulation

4.1 Switch based on an adiabatic structure

One of the switch designs selected for fabrication is the adiabatic thermo-optic switch, which represents a substantially novel device. The design combines adiabatic waveguide transitions with thermo-optic phase control to achieve a compact structure, broadband operation, and low sensitivity to polarization. In this section, the design and numerical simulation of the adiabatic thermo-optic switch are presented and compared with other existing switching approaches. Then the main performance parameters obtained from these studies to be used for extending the design toward a complete optical switching matrix composed of multiple identical switches for telecommunication applications, as introduced in Section 1.

To the best of our knowledge, this specific configuration and its intended use within a reconfigurable optical switching matrix have not been previously reported, constituting an original contribution of this work. A complete CAD layout of the device was developed and prepared for fabrication through an external silicon photonics foundry. The switch operates based on the thermo-optic effect and is designed to function efficiently for both TE and TM polarizations. Its structure relies on an adiabatic configuration employing tapered waveguides, which ensures smooth mode evolution, reduced optical losses, and stable broadband performance across the C-band (1530–1565 nm) and L-band (1565–1625 nm) commonly used in optical communication systems.

4.1.1 Adiabatic geometry design

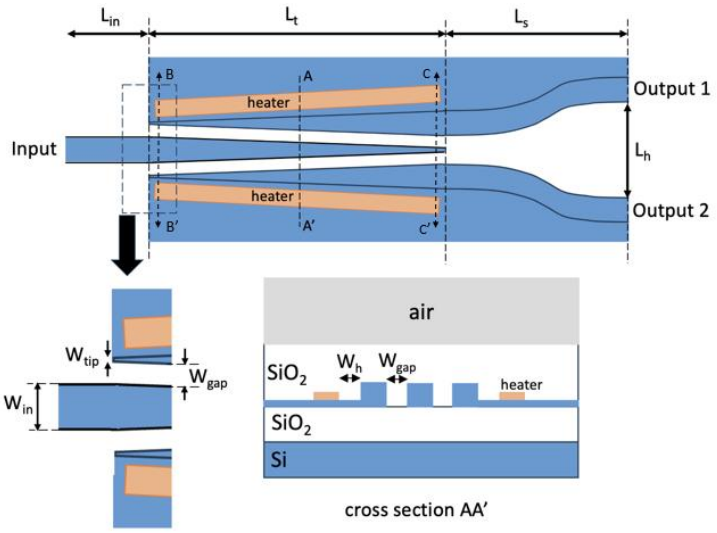

Figure 23. Geometry of an adiabatic thermo-optic switch with all relevant parameters

The adiabatic structure is shown in Fig. 23. It consists of a rectangular cross section waveguide at the input, three parallel tapered waveguides, and two S-bent waveguides at the output. The structure is fabricated in silicon (n=3.4732) with SiO_2 under- and over-cladding. It follows the design of a passive adiabatic Y-splitter [26], but with modifications: the central waveguide has a rectangular cross section, while the two outer waveguides include thin slabs (100 nm) at their outer sides. These slabs are

essential for enhancing heat diffusion from nearby heaters, which are positioned far enough away to avoid disturbing the propagating optical field. The Si waveguides have a thickness of 310 nm, which aligns with some current technology standards [66] and ensures good propagation performance for both TE and TM modes. The main geometrical parameters of the design are summarized in Table 1.

Table 1. Geometrical parameters of the switch (Fig. 23)

Parameter	Value	Description
W_{in}	500 nm	Waveguide width
W_{tip}	100 nm	Tip width of tapered waveguide
W_{gap}	250 nm	Gap between external and middle waveguides
L_{in}	10 µm	Length of input waveguide
L_t	50 – 250 µm	Length of tapered waveguides
L_s	20 µm	Length of bent waveguides
L_h	2 µm	Distance between the bent waveguides
h_1	310 nm	Thickness of silicon device layer
W_h	700 nm	Gap between heaters and side waveguides
W_{heat}	750 nm	Width of heater

4.1.2 simulation of passive adiabatic splitter

At a uniform temperature of 300 K, the device operates as a symmetric splitter. This behavior is illustrated in Fig. 24.a and Fig. 24.b, which show the electric field propagation for the TE and TM modes, respectively. Fig. 24.c and 24.d present the normalized transmission at Output 1 and Output 2 for both polarizations over the wavelength range of 1.5 to 1.65 µm. The transmitted power at each output remains around −3.20 ± 0.02 dB across the entire wavelength range, demonstrating a stable and well-balanced performance of the splitter.

4.1.3 Active adiabatic thermo-optic switch

4.1.3.1 Thermal Simulation

Building on the passive splitter described earlier, steady-state thermal simulations were performed using a 2D heat propagation numerical solver of the Lumerical software to analyze the temperature distribution when heat is applied to one of the 100 nm-thick titanium (Ti) heaters placed laterally on the device. The thermal parameters used in the simulations are provided in Table 2, including the thermo-optic coefficients of silicon (Si), silicon dioxide (SiO_2) and Titanium (Ti). The handle layer of the SOI platform is considered at the constant temperature of 300 K, while the lateral boundaries are adiabatic. The top SiO_2 cladding is exposed to air, where heat is removed by convection. The ambient temperature is 300 K.

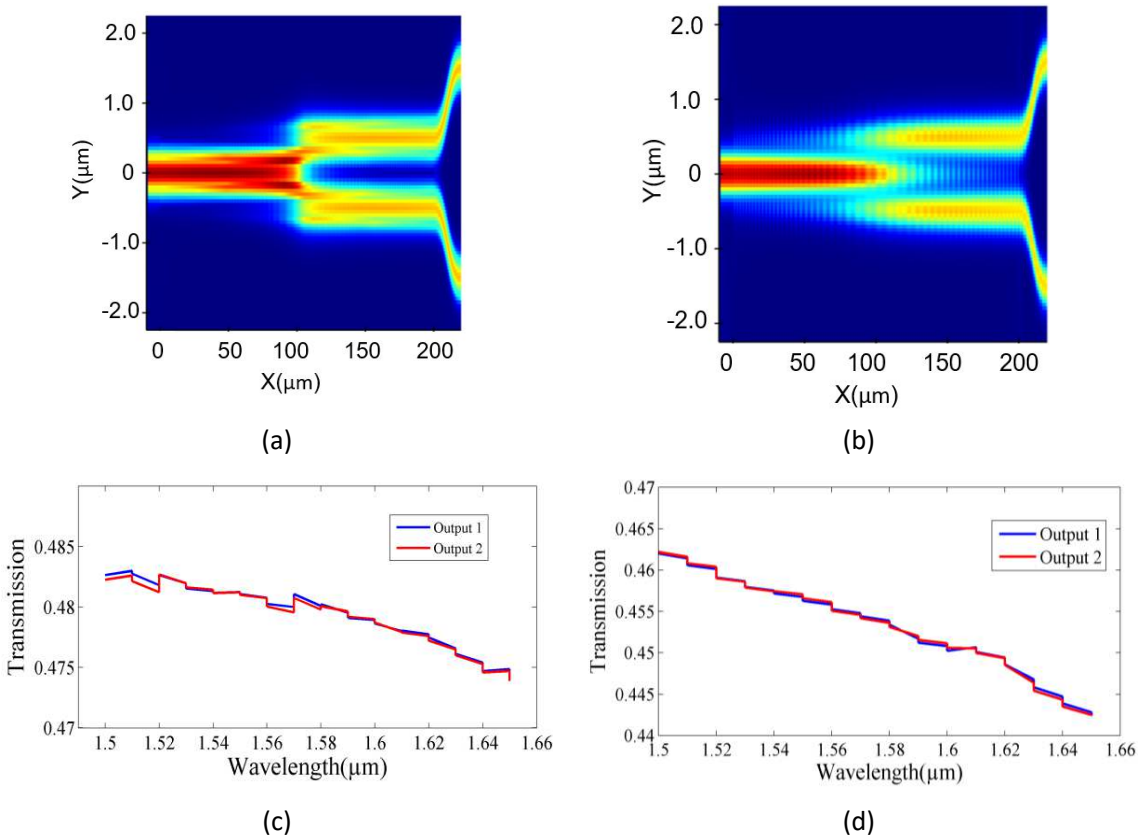

Figure 24. Electric field propagation at uniform temperature (T=300 K) for: (a) TE mode; (b) TM mode, showing the 50% splitting action at λ=1.55 μm. (c) Transmission as a function of wavelength for TE mode and (d) TM mode without applying heating.

Table 2. Thermal properties of materials

Material	Thermal conductivity (W/ m·K)	Thermo-optic coefficient (K^{-1})
Silicon (Si)	148 [67]	2.01×10^{-4} [68]
Silicon dioxide (SiO_2)	1.38 [69]	8.4×10^{-6} [70]
Titanium (Ti)	11.4 [71]	3.7×10^{-4} [72]

Figure. 25.a illustrates the temperature distribution at half length of the switch (section A-A' of Figure 23) when a power dissipation of 0.5 mW per unit length (μm) is applied to the right-side heater. Figure. 25.b shows the calculated temperature profile across the X-X' cut line at half length of the three tapered regions under the same power input of 0.5 mW/μm. Figure. 25.c shows the temperature of the three waveguides as a function of applied power. It can be seen that, due to the high thermal conductivity of silicon, each waveguide is in fact isothermal. The temperature profiles are passed to the quasi 3D Finite Difference Time Domain (FDTD) simulator to compute the propagating optical field. Results were also verified through Eigenmode Expansion (EME) simulations, which provided comparable results.

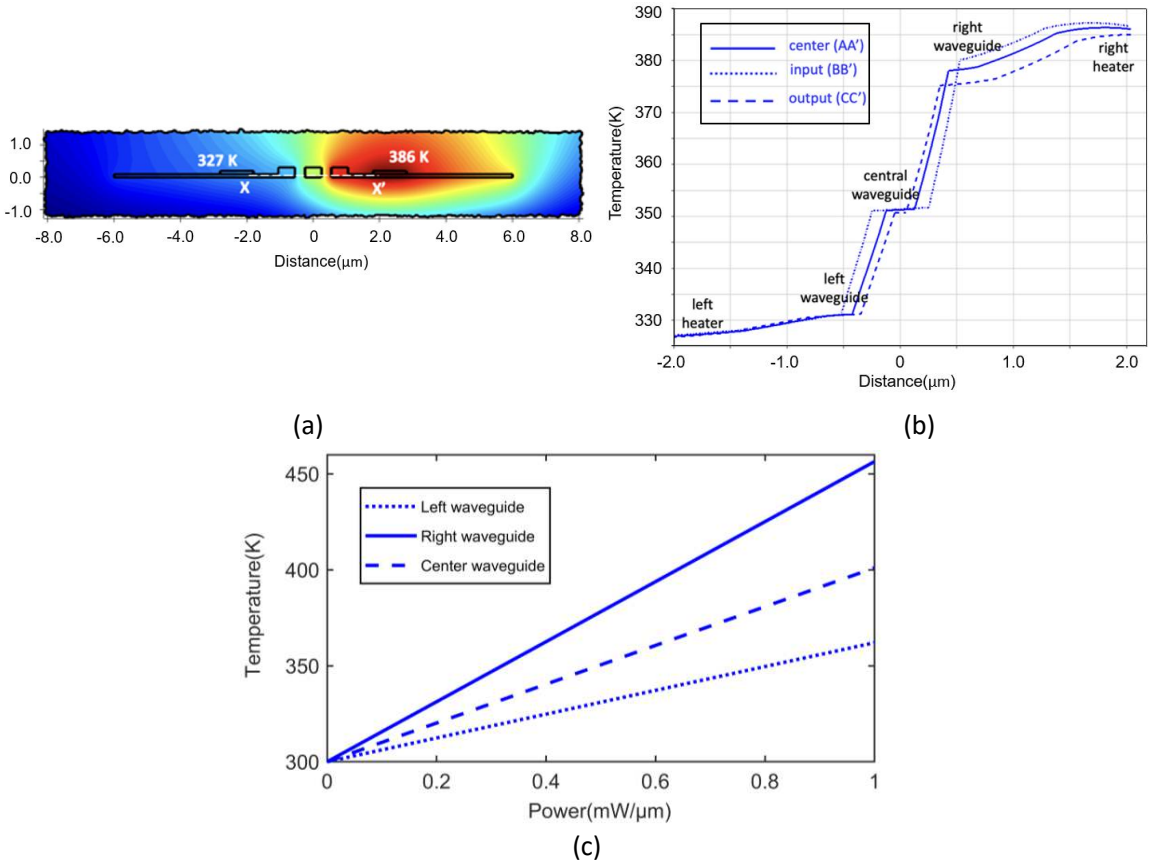

Figure 25. (a) Temperature distribution at the switch center (A-A' of Fig.1) with a generated heat of 0.5mW per unit length (μm) of the right heater; (b)Temperature profile along X-X' cut line at the three cross sections A-A', B-B' and C-C' of Figure 23, for the same generated heat; (c) Temperature at waveguide center as a function of power.

4.1.3.2 Optical Simulation

Figure. 26 shows how varying the applied power and extending the tapered waveguide length from 50 μm to 250 μm affects the extinction ratio for both TE and TM modes across the studied wavelength range. As the waveguide length increases, a clear improvement in switching performance is observed. With an applied power of 1 mW/μm, the extinction ratio for the TE mode increases from 1.05 dB to 12.15 dB at 1.525 μm and from 1.9 dB to 20.33 dB at 1.625 μm. Similarly, for the TM mode, the extinction ratio rises from 5.8 dB to 19.64 dB at 1.525 μm and from 7.36 dB to 14.27 dB at 1.625 μm. These results confirm that longer tapered waveguides significantly enhance switching efficiency for both polarizations.

The impact of varying the applied power to the lateral heater, up to a maximum of 1 mW/μm, which is a level of practical interest for thermo-optic switches, is also evident in the graphs. Figure. 27 shows the electric field distribution at the two output ports as the applied electrical power is varied from 0 mW/μm to 1 mW/μm. When no power is applied, the optical field is directed predominantly to Output 1, as shown in Fig. 27.a. By increasing the applied power to 1 mW/μm, the induced refractive-index change causes the optical field to switch to Output 2, as illustrated in Fig. 27.b.

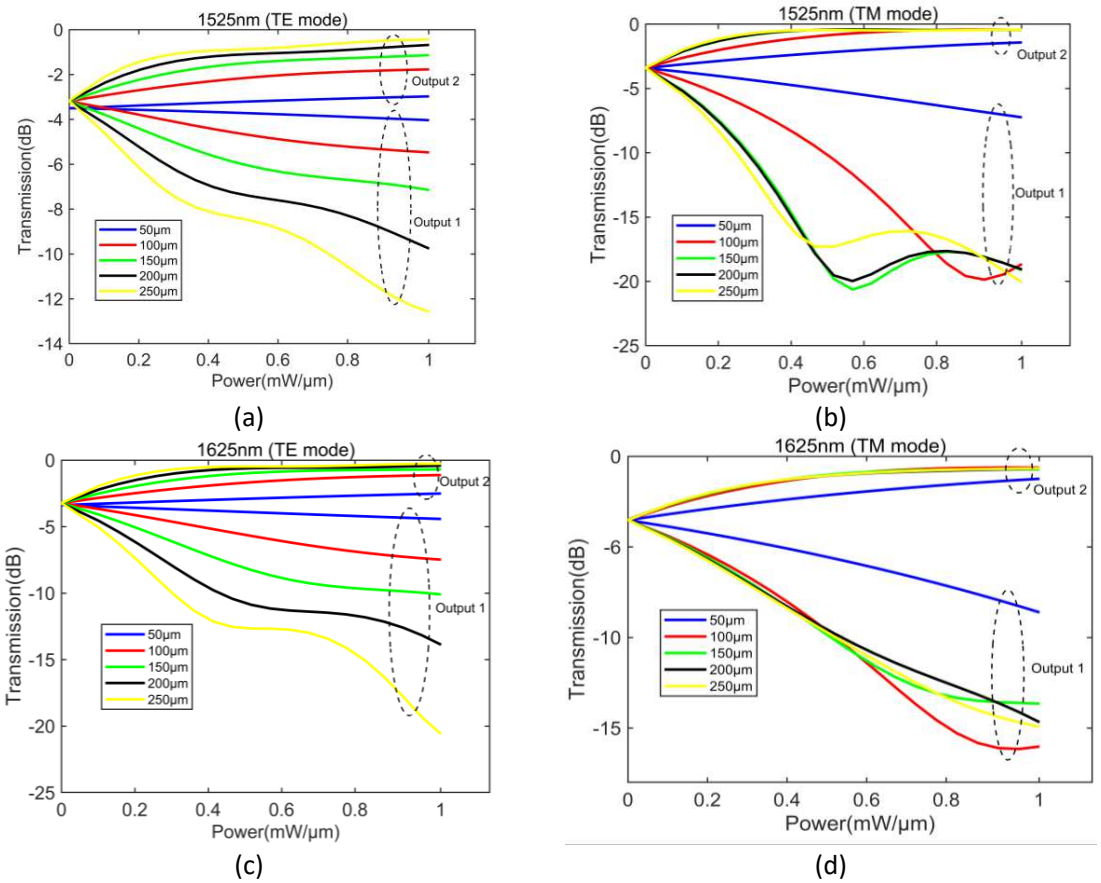

Figure 26. Transmission at the switch output ports as a function of power for different lengths of the tapered waveguides (Lt): (a) TE mode at λ=1.525 μm; (b) TM mode at λ=1.525 μm; (c) TE mode at λ=1.625 μm; (d) TM mode λ=1.625 μm.

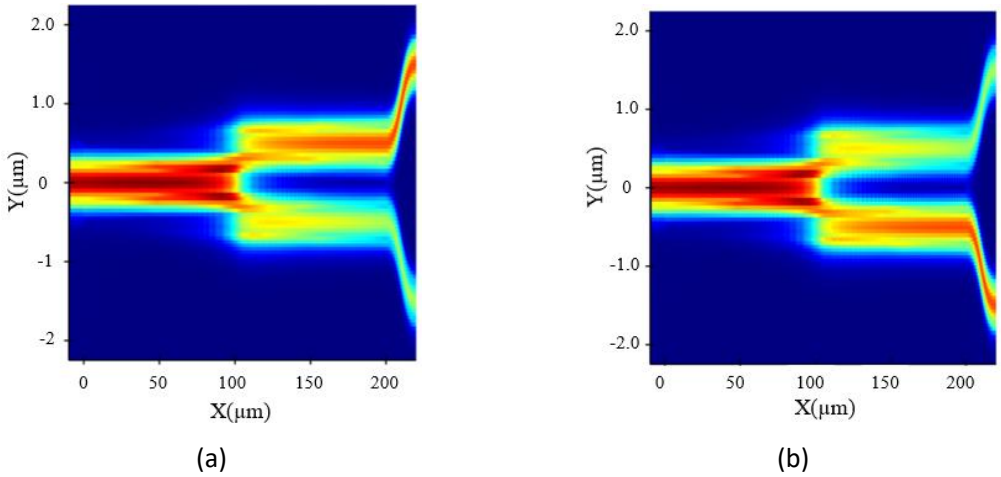

Figure 27. Electric field distribution of the switch for two applied electrical power levels: (a) 0 mW/μm, where the optical power is routed to Output 1, and (b) 1 mW/μm, where the induced refractive-index change redirects the optical power to Output 2.

Figure. 28 displays the extinction ratios (ER) across different wavelengths for both TE and TM modes when the taper length is 250 µm. The average ER values are 14.25 dB and 17 dB for the TE and TM modes, respectively. The device insertion losses (IL) were estimated by measuring the optical power loss between the device's input and output. The average IL values are 0.37 dB and 0.52 dB for the TE and TM modes, respectively, across the specified wavelength range. These values are very promising compared to other devices, also thanks to the waveguide thickness of 310 nm.

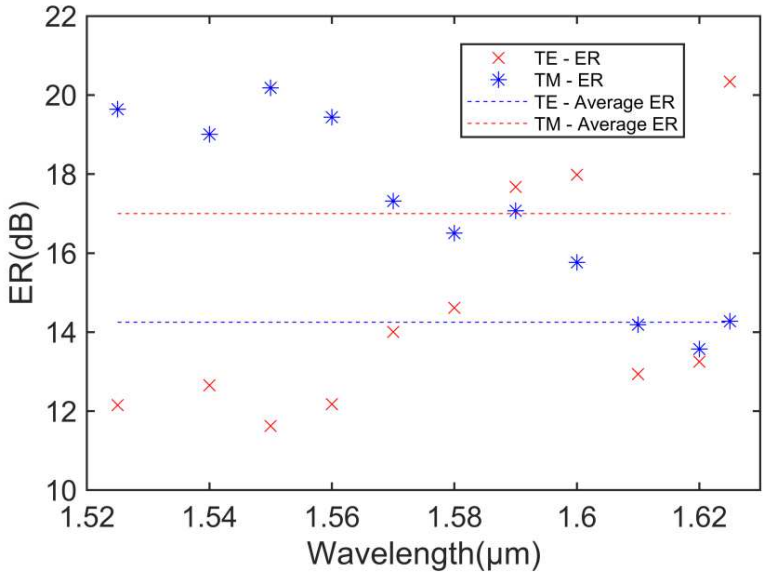

Figure 28. Extinction ratio at different wavelength for TE and TM modes with a taper length L_t=250µm and dissipated power P=1mW/µm.

The extinction ratio of the proposed switch depends on the polarization, as observed in the simulation results. Different values are obtained for TE and TM modes. This is mainly due to the different field distributions and confinement of the two polarizations inside the waveguide. Since the thermo-optic effect changes the effective refractive index, the induced phase shift is slightly different for TE and TM modes. In addition, structural asymmetries, fabrication tolerances, and small variations in waveguide dimensions can further increase this polarization dependence.

It is important to clarify that the basic structure of the device includes a 3 dB splitter, which divides the optical power equally between the two arms when no electrical power is applied. In this case, the output power is equally distributed between the two output ports. The switching operation is achieved by applying electrical power to the heater integrated on one arm of the device. This creates a local temperature change, which modifies the refractive index through the thermo-optic effect and introduces a phase difference between the two arms. As a result, constructive interference occurs at one output port and destructive interference at the other, allowing the optical power to be switched from one output to the other. By controlling the applied heating power, the phase difference can be tuned to achieve full switching between the two output ports.

4.1.4 Comparison

As shown in Table 3, a comparison of simulated adiabatic thermo-optic switch with similar devices reveals that, while the extinction ratios are comparable to those of other thermo-optic switches, the proposed device performs, at the same time, a wide bandwidth, good extinction ratio, and compactness. Additionally, it has the advantage of operating in both TE and TM modes.

We investigated a thermo-optic switch capable of operating for both polarizations. The device exploits the advantages of an adiabatic design with tapered waveguides to perform flat responses across the C and L bands of optical communications. With an overall length of 250 µm and power dissipation of 1 mW/µm, the switch achieved extinction ratios of 12.15 dB and 20.33 dB for the TE mode at wavelengths of 1.525 µm and 1.625 µm, respectively, and 19.64 dB and 14.27 dB for the TM mode at the same wavelengths. The switch exhibited low insertion losses with average values of 0.37 dB and 0.52 dB for the TE and TM modes, respectively.

The optimized structure exhibits compact size, low power consumption, and low insertion losses while maintaining a high extinction ratio for both polarizations. The simulation results confirm that the switch provides efficient and stable operation over a wide wavelength range, with very small dependence on polarization.

Table 3. Characteristics of integrated optical switches.

Ref	Scale	structure	Material	Footprint (µm2)	Power (mW)	Power / channel (mW)	IL (dB)	BW (nm)	ER (dB)	Mode	Year
[73]	1 × 8	MMI	Silica	18669 × 1754	1830	228.7	2.74 – 3.69	2	16.7	TE	2024
[74]	1 × 8	MMI	Silica	25854 × 1754	315.8	39.5	3.4 ~ 3.6	120	15.6	TE and TM	2024
[75]	2 × 2	MZS	Silicon	118.8×1.97	18.5	9.25	1 ~ 4	35	20	TE and TM	2018
[76]	2 × 2	MZI	Lithium niobate	~5450 × 140	~7.3	3.65	< 2	75	16	TE	2022
[77]	2 × 2	MZS	Silicon	1015 × 682	146.3	73.15	0.2 ~ 4.3	35	14	TE and TM	2022
[78]	1 × 2	MMI	Silicon Nitride	2335× 30	57.4	28.7	13.1	120	10	TE and TM	2023
[79]	2 × 2	MMI	Silicon	---	40	20	---	60	30	TE	2023
This work	1 × 2	Adiabatic	Silicon	280×8	250	125	0.52	100	17	TE and TM	2024

These results demonstrate that adiabatic structures implemented on silicon-on-insulator (SOI) platforms are highly suitable for thermo-optic switching applications. The design offers high stability, broadband operation, and fabrication tolerance, making it a robust solution for large-scale integrated optical systems. Moreover, the ability to fine-tune key parameters such as waveguide thickness, taper length, and coupling gap provides flexibility for performance optimization and adaptation to various photonic applications.

As shown in Table 3, the thermo-optic switch reported in [75] operates with a significantly lower driving power of 18.5 mW compared to the proposed adiabatic switch in this work, which requires approximately 250 mW. This difference is mainly related to the device structure and operating mechanism. The MZI-based switch in [75] relies on interference over a relatively short interaction length, allowing efficient phase tuning with lower thermal power. In contrast, the adiabatic switch proposed in this work is based on gradual mode evolution along a longer tapered waveguide, which requires heating over a larger region and therefore leads to higher power consumption. However, this design provides important advantages such as lower insertion loss (around 0.52 dB), broadband operation, and reduced sensitivity to wavelength and fabrication variations. Therefore, the proposed device represents a trade-off between higher power consumption and improved optical performance and robustness.

4.1.5 Interconnect simulation of the whole NxN matrix adiabatic switch

The next step of this work focuses on the design and simulation of complete 2×2 and 4×4 switching matrices based on the optimized thermo-optic adiabatic switch. This stage represents the final step toward a scalable architecture suitable for fabrication. The previously optimized single switch elements are used as a fundamental building block to construct larger N×N switching matrices, allowing the evaluation of their routing capability, insertion loss, and scalability.

4.1.5.1 S-parameter based model of the adiabatic switch

The whole switch matrix is composed of N×N switches, which cannot be "physically" simulated at the same time, due to the huge dimension of the problem. For this reason, we adopted a different approach, consisting in the extraction of the S-parameters of a switch and subsequent formulation of the simulation task in terms of the combination of the "concentrated parameters" models.

S-parameters (or scattering parameters) are a fundamental concept in RF, microwave, and photonic system analysis. They describe how electrical signals behave in multi-port networks, capturing how power is transmitted and reflected at each port. Each S-parameter, $S_{i/j}$, represents the ratio of the outgoing wave at port i to the incident wave at port j: [80]

$$S_{i/j} = \frac{output\ wave\ at\ port\ i}{input\ wave\ at\ port\ i} \tag{4.1}$$

In particular, in the example case of an optical 2-ports device:
S_{11} is the reflection coefficient at port 1,
S_{21} is the forward transmission from port 1 to port 2,
S_{12} is the reverse transmission from port 2 to port 1,
S_{22} is the reflection at port 2.

In photonic systems, these parameters are measured with an optical analyzer. Alternatively, they can be estimated by means of numerical simulations of the propagating waves.

In the case of a 2×2 optical switch (two input ports, two output ports), the S-parameter matrix can be:

$$S = \begin{bmatrix} S_{11} & S_{12} & S_{13} & S_{14} \\ S_{21} & S_{22} & S_{23} & S_{24} \\ S_{31} & S_{32} & S_{33} & S_{34} \\ S_{41} & S_{42} & S_{43} & S_{44} \end{bmatrix} \quad (4.2)$$

4.1.5.2 S-parameter in simulation

For the simulation of the 2×2 adiabatic switch matrix, an individual adiabatic switch was first designed and simulated using the VARFDTD module in Lumerical. To export the S-parameter data from the adiabatic switch simulated in VARFDTD (Lumerical), frequency-domain monitors were placed at the input and output ports to record transmission and reflection coefficients across the wavelength range. The software then computed the scattering matrix (S-matrix), which was exported in Touchstone (.snp) format, including frequency, amplitude, and phase data for each port. The file later imported into Lumerical INTERCONNECT, where a complete matrix switch consisting of four adiabatic switches was modeled and analyzed to study its overall optical performance.

4.1.5.3 Interconnect simulation tool

INTERCONNECT is a photonic circuit simulator in Ansys Lumerical used for system-level modeling and analysis of integrated optical circuits. It allows designers to connect multiple components through their S-parameters and simulate the overall circuit behavior in both the time and frequency domains. In this work, Interconnect was used to model and analyze the adiabatic switch matrix, enabling accurate evaluation of its optical performance, without the need for full electromagnetic simulations.

4.1.5.4 Schematic of the simulated switch matrix

Figure. 29 shows the schematic of the 2×2 matrix switch, which is composed of four optimized adiabatic switches, labeled A, B, C, and D, and one waveguide crossing element (WX_1), which is used to route the optical signals between intersecting paths while minimizing insertion loss and crosstalk. The input width for switches C and D was set to 530 nm, while for switches A and B, it was kept at 500 nm. This adjustment was made because switches C and D showed improved performance in the reverse direction for wavelengths between 1.52 µm and 1.62 µm with the wider input width. This matrix structure is designed to operate bidirectionally:

Forward Direction: This mode functions at wavelengths between 1.52–1.62 µm. The input is applied to switches A or B, and by applying heat, we can route the signal between their output ports. The signal then passes through switches C and D, directing the output based on the applied heating pattern, as seen in Fig. 29.a.

Backward Direction: This mode operates at wavelengths of 1.3–1.36 µm, where the input is applied to switches C and D, and the output is directed through switches A and B, as shown in Fig. 29.b.

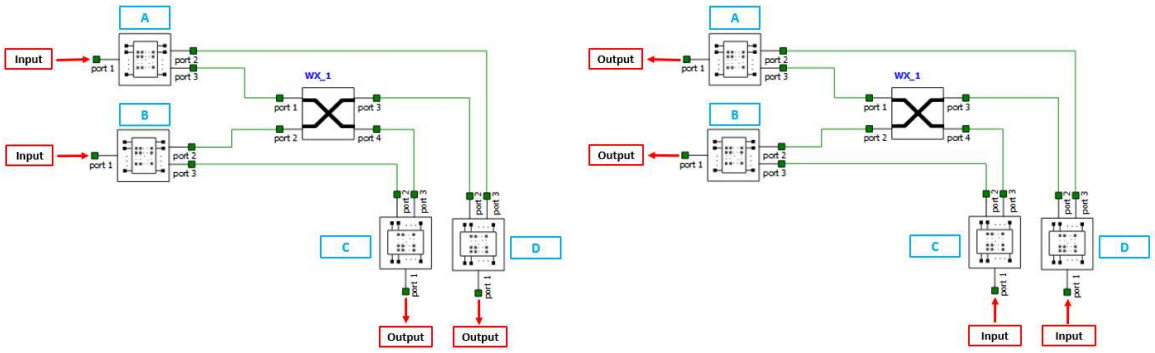

Figure 29. (a) Schematic of the simulated 2×2 switch matrix in the forward direction, where the signal propagates from switches A or B to C or D within the wavelength range of 1.52–1.62 µm. (b) Schematic of the switch matrix in the backward direction, where the signal propagates from switches C or D to A or B within the wavelength range of 1.3–1.36 µm.

4.1.5.5 Optical adiabatic switch in the opposite direction

As observed in the 2×2 switch array, the optical switches are designed to operate efficiently in both directions. When heat is applied to the device arms, the temperature of the tapered waveguides in the adiabatic switches varies between 300 K and 456 K, depending on the position of the heater. Figure 30 illustrates the geometry of the switch operating in the opposite direction. It is important to note that switches A and B have an input width of 530 nm, while switches C and D use an input width of 500 nm, selected to achieve optimal performance during bidirectional operation.

Although the device is reciprocal from a physical point of view, the geometrical parameters of switches A and B are slightly different from those of switches C and D. This is related to the bidirectional operation of the matrix. In the forward and backward directions, the optical signal enters the switches under different conditions in terms of mode profile and waveguide transitions. For this reason, the input widths of A/B (530 nm) and C/D (500 nm) were independently optimized to achieve the best performance in each propagation direction. Therefore, this difference in design does not violate reciprocity, but results from the need to optimize the adiabatic transition for both directions under realistic operating conditions.

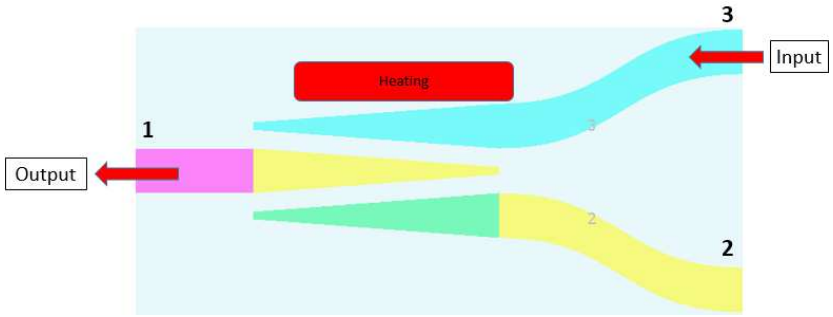

Figure 30. Geometry of an adiabatic switch in the opposite direction.

Figure. 31 shows the backward transmission (from port 3 to port 1) of switches A or B and C or D as a function of wavelength for both TE and TM modes when heating is applied to the arm of the adiabatic

switch. The relevant transmission is for the wavelength range 1300-1360 nm for ports A and B, while it is calculated in the range 1520–1620 nm for Ports C and D.

As seen in the results, the average of insertion loss for switches A and B at the wavelength range of 1.3–1.36 µm is 0.8 dB for the TE mode and 0.36 dB for the TM mode. Similarly, for switches C and D at the wavelength range of 1.52–1.62 µm, these values are 0.5 dB and 0.36 dB, respectively.

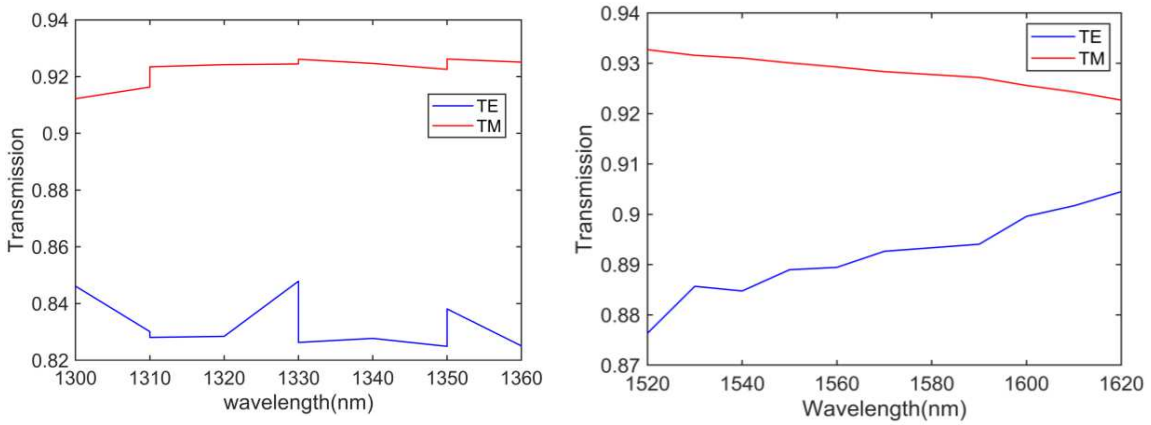

(a) (b)

Figure 31. (a) Transmission of switches A and B from port 3 to port 1 as a function of wavelength. (b) Transmission of switches C and D as a function of wavelength from Port 3 to Port 1.

4.1.5.6 Simulation result of the 2×2 matrix switch

As shown in Fig. 32, the transmission characteristics of the switch matrix are plotted as a function of wavelength for two operating ranges, considering both TE and TM polarizations. Figure. 32.a presents the switch operating in the forward direction from switches A and B toward switches C and D within the 1.52–1.62 µm range. The average insertion loss is approximately 0.7 dB for the TE mode and 0.91 dB for the TM mode, demonstrating good optical performance with minimal loss. In contrast, Fig. 32.b shows the switch operating in the reverse direction, where light travels from switches C and D toward switches A and B within the 1.3–1.36 µm wavelength range. In this case, the average insertion loss is about 1.7 dB for the TE mode and 1.3 dB for the TM mode, indicating slightly higher loss.

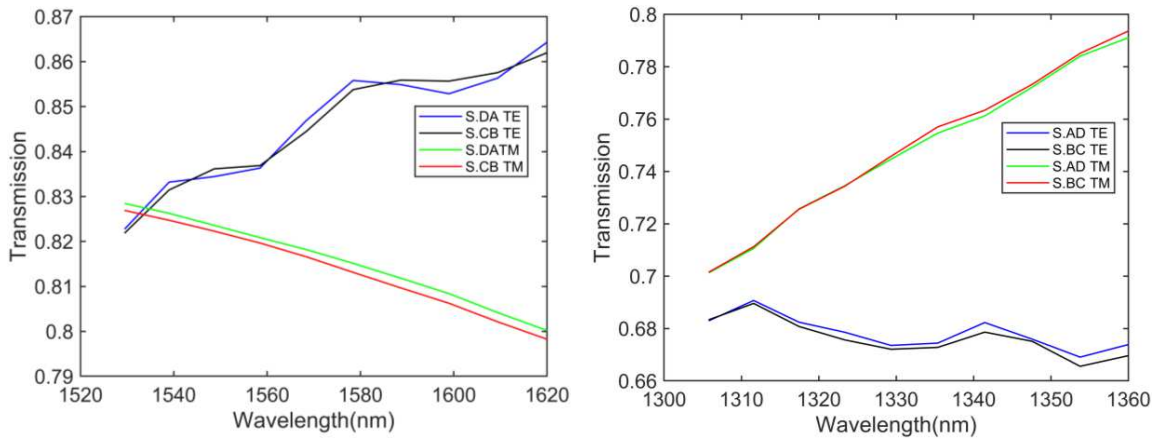

Figure 32. (a) Transmission as a function of wavelength for a 2×2 switch in the forward direction (download wavelength range in PONs). (b) Transmission as a function of wavelength for a 2×2 switch in the backward direction (upload wavelength range in PONs).

4.1.5.7 Simulation of the 4×4 switch matrix

In the final part, the performance of a 4×4 adiabatic switch matrix was analyzed to evaluate the scalability and behavior of the system on a larger scale. This investigation is an important step toward the final goal of our project, which is to design scalable and efficient optical switch networks such as 16×16 matrices that can be used in future communication systems. These larger switches are intended to support technologies like fiber-to-the-home (FTTH), where high-speed internet connections are delivered directly to users through optical fiber, improving connection and reliability of the network.

As illustrated in Fig. 33, the 4×4 switch matrix is composed of 24 adiabatic switches, arranged so that every three switches form a 1×4 switch, labeled A, B, C, D, E, F, G and H. Similar to the 2×2 configuration, this matrix is designed for bidirectional operation, with the forward direction operating within the 1.52–1.62 µm wavelength range and the reverse direction functioning between 1.3–1.36 µm. The complete structure was simulated using the Lumerical Interconnect tool to analyze its optical transmission and switching performance under realistic operating conditions.

We analyzed the simulation results for both the longest and shortest optical paths within the 4×4 switch matrix, specifically from switch A and D to switches H and E vice versa for backward direction. As shown in Fig. 34, in the forward direction (1.52–1.62 µm wavelength range), the average insertion loss is approximately 1.55 dB for the TE mode and 1.8 dB for the TM mode. In the reverse direction, the insertion loss increases slightly, reaching 3.6 dB for the TE mode and 2 dB for the TM mode.

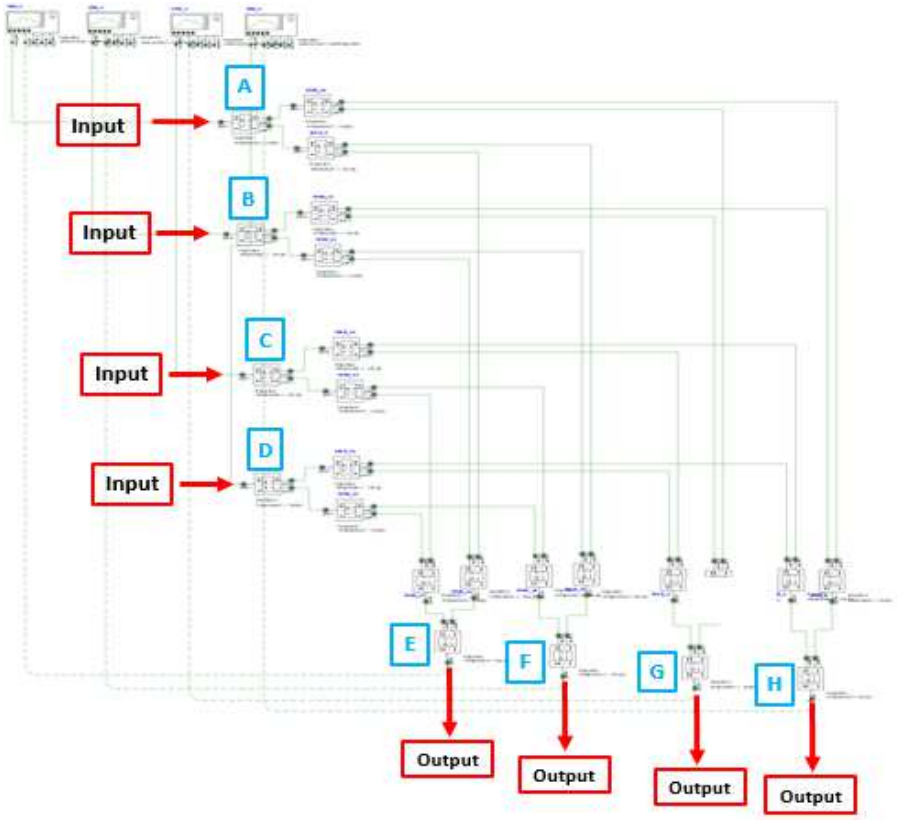

Figure 33. Schematic of the simulated 4×4 switch matrix in the forward direction, where the signal propagates from switches A or B or C or D to the switches E or F or G or H within the wavelength range of 1.52–1.62 µm.

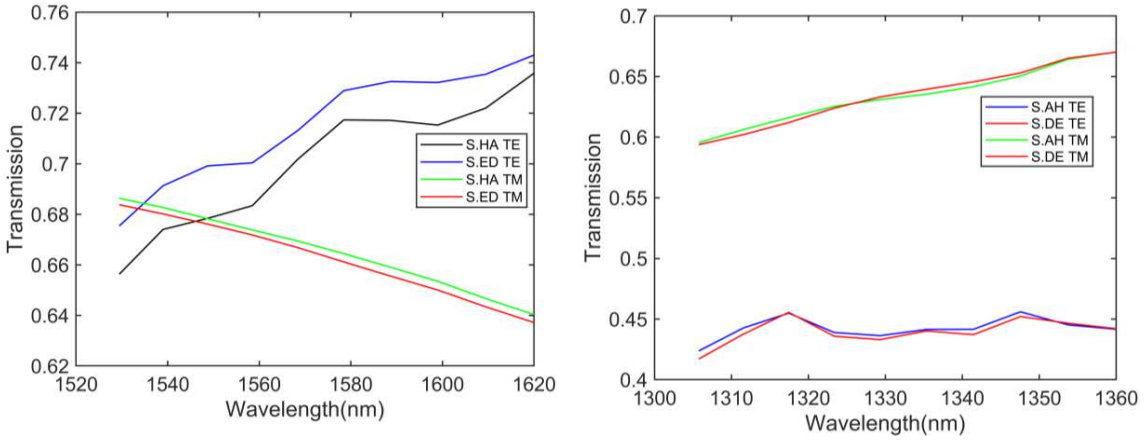

(a) (b)

Figure 34. (a) Transmission as a function of wavelength for a 2×2 switch in the forward direction. (b) Transmission as a function of wavelength for a 2×2 switch in the backward direction.

4.1.6 Conclusion

In this section, a novel adiabatic thermo-optic switch has been designed, simulated, and validated as a fundamental building block for scalable optical switching matrices. The results demonstrate that the proposed adiabatic architecture provides broadband, polarization-insensitive operation with low insertion loss, compact footprint, and good fabrication tolerance on an SOI platform. By exploiting smooth mode evolution through tapered waveguides and efficient thermo-optic control, the switch achieves stable performance across the C- and L-bands. Furthermore, the successful extension of the single-device concept to 2×2 and 4×4 matrix configurations using an S-parameter–based approach confirms the scalability and suitability of this design for large-scale reconfigurable photonic switching networks targeting telecommunication applications.

In addition, the extinction ratio was evaluated with respect to the other output ports of the switch in order to quantify the suppression of unwanted signals. Based on the simulation results of the adiabatic switch, extinction ratio values in the range of about 12–20 dB for TE mode and 14–19 dB for TM mode were obtained. These results show that the optical power at the non-selected ports is sufficiently suppressed. When extending the design to the switching matrix, a similar behavior is expected, although the overall extinction ratio can be slightly affected by the accumulation of losses and crosstalk from multiple stages. Overall, the obtained values confirm that the proposed structure provides adequate isolation between the output ports for switching applications.

4.2 Multi-Mode Interference (MMI) Mach–Zehnder Interferometer for Thermo-Optic Switching

Another promising switch configurations selected for the final design is based on a Multimode Interference (MMI) Mach–Zehnder interferometer. The structure consists of a 1×2 MMI splitter at the input, which divides the optical power equally between the two arms of the interferometer, followed by a 2×2 MMI coupler at the output. By applying heat to one of the two arms, the thermo-optic effect induces a phase shift between them. This phase difference leads to constructive or destructive interference in the second MMI, enabling optical switching between the two output ports. In this way, the output of the device can be controlled simply by heating one arm of the Mach–Zehnder.

In the first step, a 1×2 MMI splitter was designed and simulated to achieve efficient passive power splitting. The geometry was optimized to ensure good optical performance while taking into account the fabrication constraints of our cleanroom, particularly the 1 µm lithography resolution.

After establishing the passive splitter design, a full MMI-based Mach–Zehnder thermo-optic switch was simulated. In this configuration, a 2×2 MMI coupler and a controlled phase shift between the two arms were used to evaluate the switching behavior at the output ports. Finally, an asymmetric Mach–Zehnder structure using the same MMI components was also investigated. In this case, intentional length differences between the two arms were introduced, and the impact of this asymmetry on switching performance across different wavelength ranges and arm-length variations was analyzed.

The geometry of the complete MMI-based Mach–Zehnder switch, featuring one input, two outputs, two thermo-optic phase shifters, and the two interferometer arms, is shown in Fig. 35.

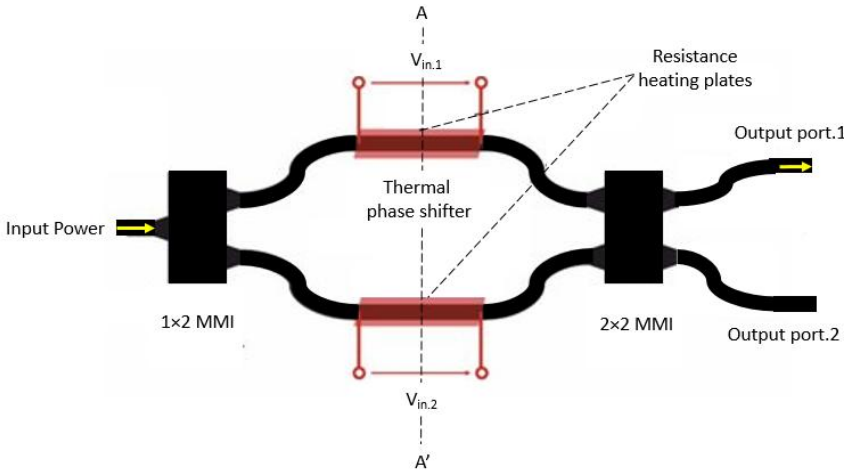

Figure 35. Schematic of the complete MMI-based Mach–Zehnder thermo-optic switch, including the 1×2 and 2×2 MMI structures and the metal resistive heaters fabricated above the waveguide arms. The thermal phase shifters enable controlled phase modulation between the two arms, allowing optical switching between the output ports.

MMI structures were selected for their broadband response and high fabrication tolerance, which make them ideal components for integrated photonic circuits. Unlike directional couplers, MMIs operate based on the self-imaging principle [34] rather than precise coupling lengths, enabling them to maintain stable performance even in the presence of minor fabrication tolerances. These characteristics make MMI-based switches highly reliable, compact, and fully compatible with standard silicon photonics fabrication processes. [61]

4.2.1 MMI passive splitter

As a first step toward realizing the complete MMI thermo-optic switch, a 1×2 MMI splitter was carefully designed, and simulated. This splitter serves as the fundamental building block of the full device, making it essential to validate its performance before proceeding with the complete switch. To determine the optimal geometry, a series of Finite-Difference Time-Domain (FDTD) simulations were carried out in Lumerical, focusing on maximizing the transmission performance while ensuring that all parameters remain compatible with the fabrication constraints of our cleanroom, which has a resolution limit of 1 µm. The geometry of the simulated 1×2 MMI splitter is shown in Fig. 36.

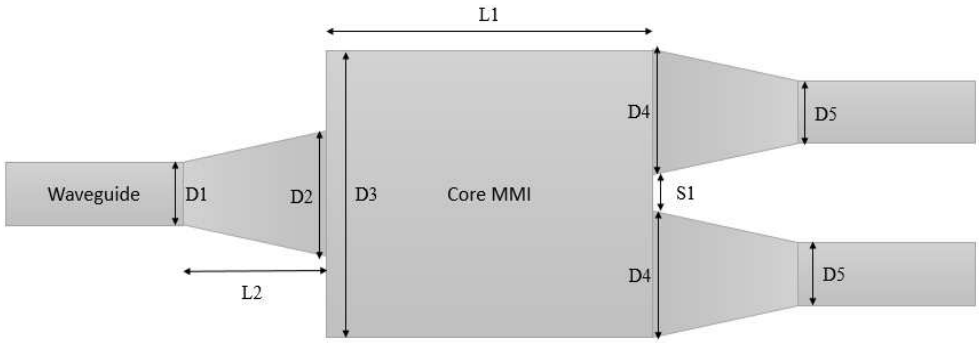

Figure 36. Schematic geometry of the 1×2 MMI splitter, showing all key design parameters.

Figure. 37.a shows the simulated transmission at the output ports of the splitter while sweeping the length of the MMI core (L_1). As observed, the best optical performance occurs at a core length of approximately 44 µm, where the insertion loss is minimized (0.65 dB). Figure. 37.b illustrates the transmission at the two output ports as a function of the MMI width. As can be seen, selecting a width of 6 µm provides the best transmission performance. The power imbalance between the two output ports is effectively zero, meaning that both outputs exhibit perfectly matched transmission, as expected for an ideal 1×2 MMI splitter. Table 4 summarizes the optimized design parameters obtained from these simulations.

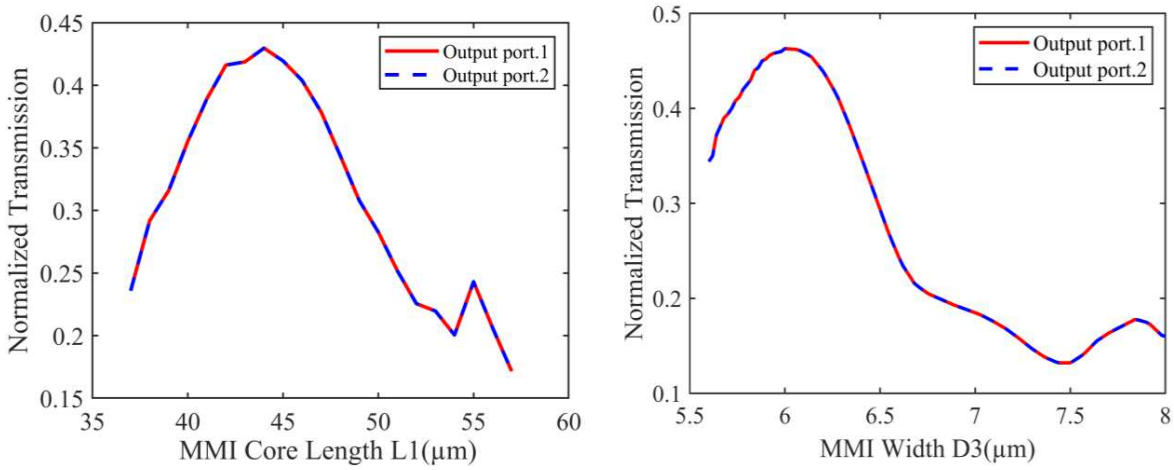

(a) (b)

Figure 37. (a)Normalized transmission as a function of MMI core length (L_1). (b) Normalized transmission as a function of MMI width (D_3). The simulation results show that for a wavelength of 1.55 µm, the transmitted optical power is equally divided between the two output ports, achieving zero power imbalance at the optimized parameters.

Table 4. Optimized parameters for 1×2 and 2×2 MMI geometry

Parameters	1×2 MMI Passive splitter	2×2 MMI geometry
L1	44 µm	56 µm
L2	12 µm	---
D1	1 µm	1 µm
D2	2 µm	1 µm
D3	6 µm	6 µm
D4	1 µm	1 µm
D5	1 µm	1 µm
S1	1.8 µm	1.8 µm
S2	---	1.4 µm
MMI Thickness	1.5 µm	1.5 µm

Figure. 38.a presents the simulated transmission at the two output ports as a function of wavelength. The figure also shows that the transmission varies between 0.39 and 0.42 over the simulated wavelength range, corresponding to an average insertion loss of approximately 0.77dB. Figure. 38.b

illustrates the simulated electric field distribution of the TE mode at a wavelength of 1.55 µm, corresponding to the optimized design parameters obtained from the simulation.

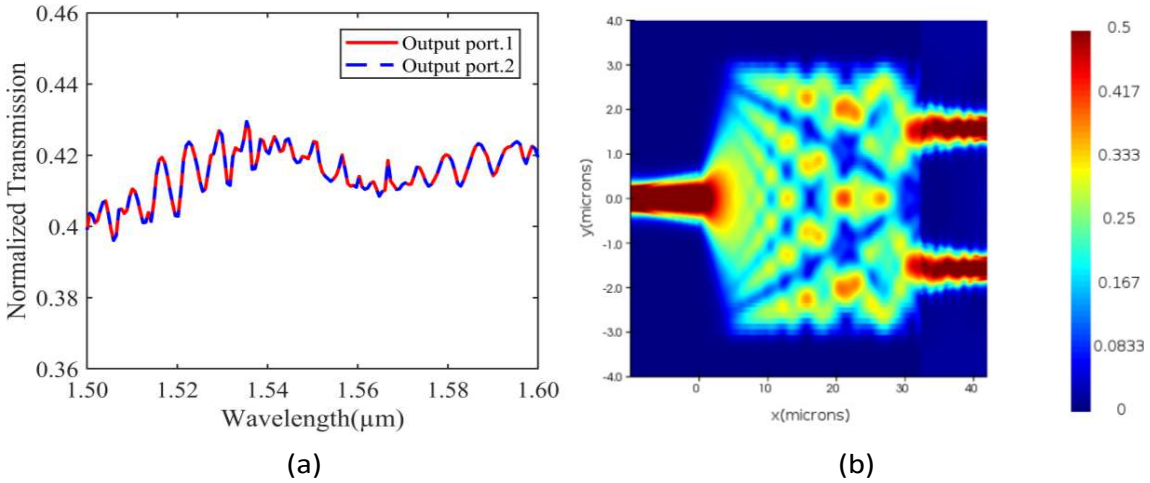

Figure 38.(a) Normalized transmission as a function of wavelength for the 1×2 MMI splitter. The transmission at the two output ports is nearly identical, indicating equal power distribution and confirming the absence of any phase shift between the outputs. (b) Simulated electric field distribution of the TE mode at the wavelength of 1.55 µm.

After finalizing the simulation of the 1×2 MMI passive splitter, we proceeded to simulate the next part of the complete switch.

Information on the refractive index, thermo-optic coefficient and thermal conductivity of the materials employed in this simulation is summarized in Table 5. All parameters are evaluated at an operating wavelength of 1.55 µm, based on the Palik model, and are used consistently throughout the simulation presented in this thesis.

Table 5. Material properties using in simulation of MMI splitter and switch.

Material	**Refractive Index (n)**	**Thermo-optic coefficient (K^{-1})**	**Thermal conductivity (W/ m·K)**
Silicon (Si)	3.48	1.86×10^{-4} [68]	148 [67]
Silicon dioxide (SiO_2)	1.44	8.4×10^{-6} [70]	1.38 [69]
Nickel (Ni)	3.38	10^{-4}	91 [71]

4.2.2 Active Mach-Zehnder thermo-optic switch with MMI structure

For simulating a complete symmetric Mach–Zehnder switch, a 2×2 MMI is used to direct the light to one of the two outputs depending on the phase shift imposed by the MZI. Figure. 39 shows the 2×2 MMI structure along with all the geometrical parameters.

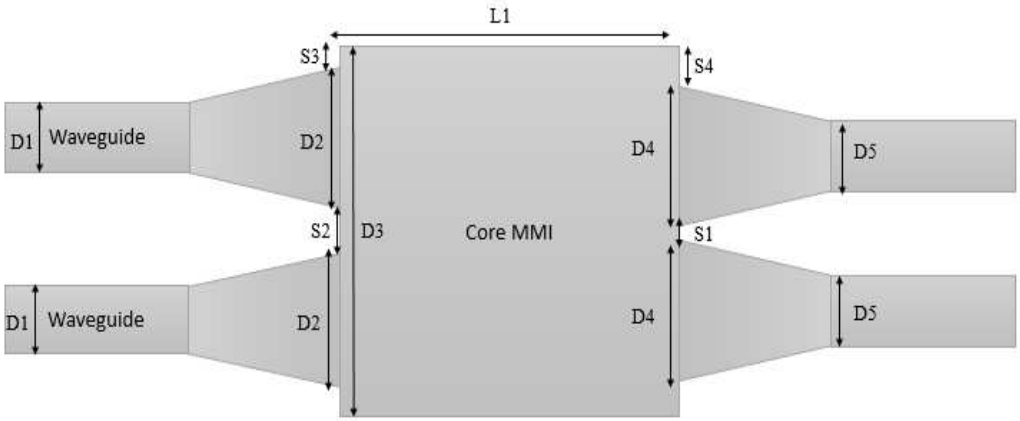

Figure 39. Schematic geometry of the 2×2 MMI structure, showing all key design parameters.

At first, the optical signal was launched into one of the input ports, and the output transmission was analyzed while optimizing all design parameters to achieve the best possible transmission with minimum insertion loss. All of the optimized parameters for the switch are listed in Table 4. Figure. 40.a shows the effect of the MMI core length (L_1) on the transmission characteristics. The optimal core length was found to be 56 µm, where a minimum insertion loss of approximately 0.44 dB was obtained, indicating efficient power transfer and low propagation loss in the splitter.

After optimizing the parameters of the 2×2 MMI, the optical power was equally launched into both input ports of the structure. To create an interference effect, a phase shift was applied to one of the input waveguides, gradually varying from 0 to 2π, in order to introduce a controlled phase difference between the two arms of the symmetric Mach–Zehnder interferometer. The transmission at the output ports was then analyzed to evaluate the switching performance of the device.

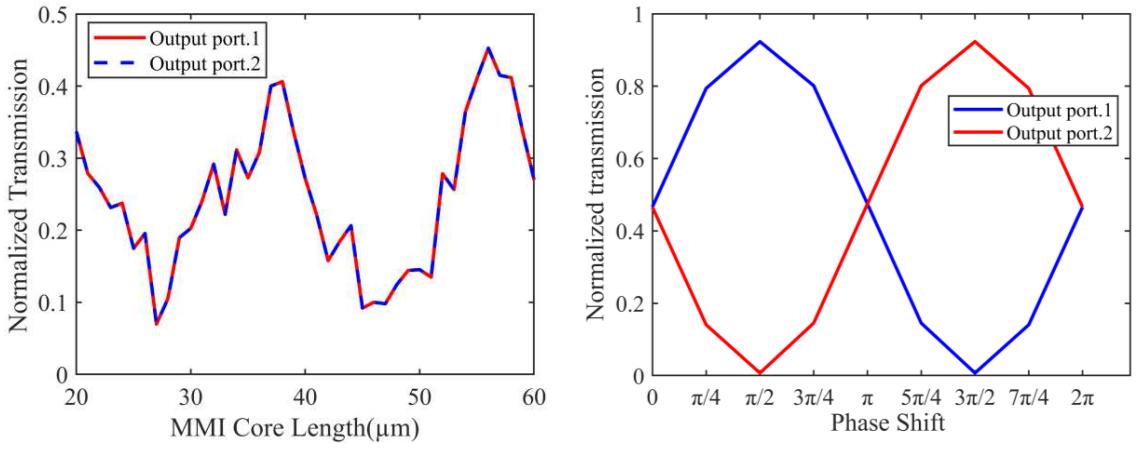

(a) (b)

Figure 40. (a) Simulated normalized transmission as a function of MMI core length (L_1) for the 2×2 MMI structure. The transmission at the two output ports is nearly identical, indicating equal power splitting in the absence of a phase shift. (b) Normalized transmission at the two output ports as a function of the phase shift between the interferometer arms, demonstrating complementary switching behavior due to constructive and destructive interference.

As shown in Fig. 40.b, at a wavelength of 1.55 µm, when the phase shift increases from π/2 to 3π/2, the output power at Port 1 rises from 0.7% to 92%, while the transmission at Port 2 correspondingly decreases from 92% to 0.7%. This clear and complementary behavior between the two output ports confirms the correct operation of the MMI-based Mach–Zehnder switch, which toggles between the two output ports through phase modulation control. The switching effect results from constructive and destructive interference, achieved by varying the phase difference between the two arms of the interferometer.

4.2.2.1 Thermal simulation

We can calculate the effective index change in silicon that corresponds to the required phase shift using the following relation: [62]

$$\Delta\phi = \frac{2\pi}{\lambda} \cdot \Delta n_{eff} \cdot L \tag{4.3}$$

Where λ is the operating wavelength and L is the length of the Mach–Zehnder interferometer arm, as in Fig. 35. By choosing L=250 µm and λ=1.55 µm, a phase shift of π/2, which is needed for complete switching between the output ports, requires a refractive index change of approximately Δn = 0.00155. Considering the thermo-optic coefficient of silicon:

$$\frac{\Delta n_{eff}}{\Delta T} = 1.86 \cdot 10^{-4}\ K^{-1} \tag{4.4}$$

In this formulation, the refractive index variation should be considered in terms of the effective index n_{eff} rather than the bulk material index. This is because the optical mode is not fully confined in the silicon core, but is partially distributed in the surrounding materials. Therefore, the effective thermo-optic response depends on the modal confinement. By taking into account the confinement factor, the effective index variation becomes larger than the value estimated using only the material thermo-optic coefficient. As a result, the required phase shift can be achieved with slightly lower temperature variation compared to the initial estimation.

A temperature increase of approximately 8.3 °C is required to achieve this refractive index change.

Figure. 41 shows a schematic cross-sectional view of the simulated geometry along the A–A' cutline of Fig. 35, used for the two-dimensional thermal simulation. The structure includes two heaters positioned above and below the Mach–Zehnder arms, separated from the waveguides by a thin silicon slab with a thickness of 0.01 µm. This thin silicon layer is introduced to enhance heat transfer to the waveguide arms, since thermal conduction in silicon is significantly more efficient than in air. At the same time, its thickness is kept sufficiently small to avoid perturbing the optical mode or altering the direction of light propagation. The thermal analysis was performed using the HEAT solver in the Lumerical software, operating in steady-state boundary-condition mode. A minimum mesh size of 0.02 µm was used to ensure adequate spatial resolution of the temperature distribution.

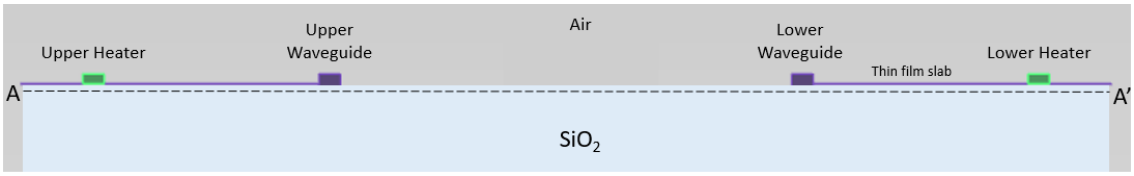

Figure 41. Schematic cross-sectional view of the simulated structure along the X-X' cutline, showing the upper and lower waveguides with their corresponding thermo-optic heaters used in the two-dimensional thermal analysis.

Figure. 42.a presents the thermal simulation results which shows how the temperature distribution in the silicon waveguide arms changes when electrical power is applied to the heaters shown in Fig. 41. Nickel was chosen to realize these heaters because it's relatively high resistivity ($\rho \approx 20 \times 10^{-8}$ Ω•m for thin films) allows efficient Joule heating, and it can be easily deposited and patterned using standard evaporation and lift-off processes.

As shown in Fig. 42.b, , when 0.191 mW/µm of power is applied to the heater placed at a distance of 5 µm from one of the waveguide arms, the temperature in that arm increases by approximately 8.3 °C. Because the two arms of the Mach–Zehnder interferometer are separated by 100 µm, the second arm remains almost unaffected by the applied heat, ensuring the required temperature difference to induce the desired phase shift for switching.

The heater is intentionally positioned at a certain distance from the waveguide rather than directly on top of it in order to reduce optical absorption losses caused by the metal heater overlapping with the optical mode. By maintaining this separation, efficient thermal tuning can be achieved while minimizing additional propagation losses. In this design, the waveguide width is approximately 500 nm, which ensures single-mode operation and is consistent with the design parameters used throughout this work.

This temperature variation provides the required π/2 phase shift, confirming that by applying 0.191 mW/µm of electrical power, the switch can effectively toggle the optical signal between the two output ports of the MMI-based Mach–Zehnder interferometer.

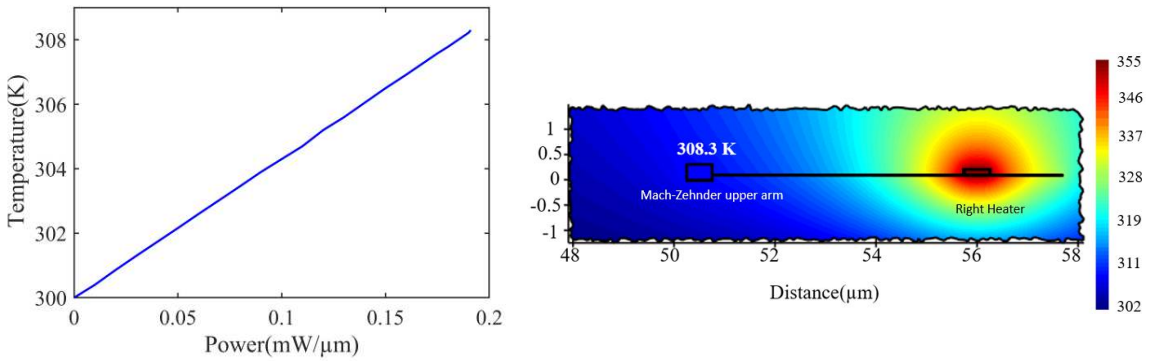

(a) (b)

Figure 42. (a) Temperature variation in the right arm of the Mach–Zehnder thermo-optic switch as a function of the applied heating power to the metallic heater. (b) Temperature distribution map of the switch waveguide arm when 0.191 mW/µm of heat power is applied to the right heater.

4.2.3 Asymmetric Mach-Zehnder Interferometer with MMI structure

In this section, an asymmetric Mach–Zehnder interferometer switch (AMZIS) was simulated using MATLAB. In a symmetric Mach–Zehnder interferometer, both arms have equal length and no phase difference appears unless an external mechanism is applied. In an asymmetric MZI, the two arms have different lengths, creating a built-in phase shift that makes the device naturally wavelength-dependent.

MATLAB was chosen for this simulation because the building blocks of the device, including the 1×2 MMI splitter and the 2×2 MMI coupler, were already defined in the previous section. Therefore, the only remaining task was to determine the appropriate ΔL between the two arms, which can be evaluated quickly through MATLAB simulations. The length difference introduces a phase shift between the two optical paths, and when the beams recombine, this phase shift creates constructive or destructive interference at the output ports.

The asymmetric configuration was selected because the inherent optical path difference, combined with thermo-optic tuning, enables controlled switching between the two output ports. This design provides improved tuning flexibility and a stronger wavelength-dependent response compared to the symmetric structure. [81]

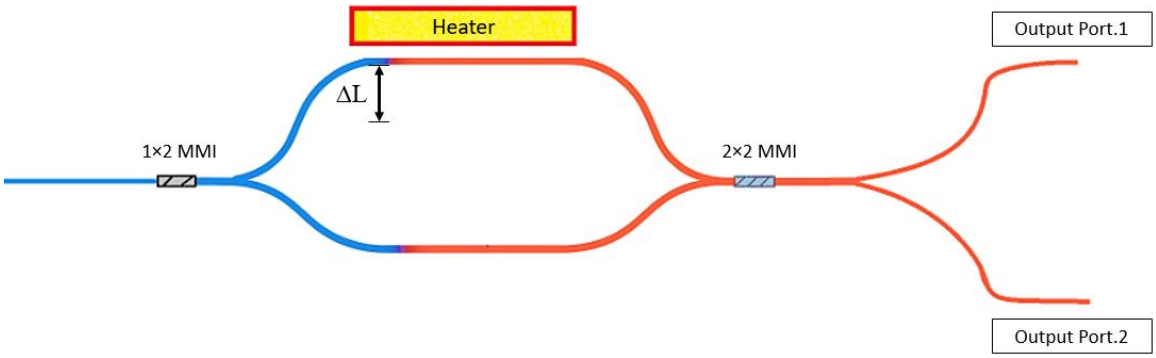

Figure 43. Schematic geometry of the asymmetric Mach–Zehnder thermo-optic switch (AMZIS) based on MMI structures. The device consists of one 1×2 MMI and one 2×2 MMI coupler connected by two interferometer arms of unequal lengths (ΔL), with an integrated heater placed above one arm to induce a controlled phase shift.

As shown in Fig. 43 the simulated asymmetric Mach–Zehnder device is composed of one 1×2 MMI splitter and one 2×2 MMI coupler, both previously optimized with insertion losses of 0.65 dB and 0.44 dB, respectively. After passing through the 1×2 MMI, the optical signal is divided into two arms. Because the two arms have different lengths, a built-in phase shift is introduced. A thin 10 nm nickel heater is placed near one of the waveguides to further control this phase shift through the thermo-optic effect. When the two optical fields recombine in the 2×2 MMI, they interfere and produce the final outputs at the two output ports.

To investigate the effect of asymmetry, simulations were performed for three different arm-length differences of 50 µm, 60 µm, and 70 µm. For each configuration, the heating power applied to the nickel heater was varied from 0 to 0.24 mW/µm, which modifies the effective refractive index of the

heated waveguide through the thermo-optic effect. Figure. 44 shows the normalized transmission at the two output ports over the wavelength range of 1.55–1.65 µm for all three arm-length differences. These results allow us to clearly observe how the thermo-optic phase shift affects the output distribution and how the level of asymmetry influences the overall switching behavior of the device.

4.2.4 Conclusion

In this section, an MMI-based Mach–Zehnder thermo-optic switch was designed and investigated through numerical simulations. The results confirm that MMI couplers provide efficient power splitting, broadband operation, and high tolerance to fabrication imperfections, making them well suited for integrated thermo-optic switching. Both symmetric and asymmetric Mach–Zehnder configurations demonstrated clear and controllable switching behavior based on thermally induced phase shifts, with low insertion loss and high extinction ratio. Based on their stable performance and compatibility with standard silicon photonics processes, these designs were selected for fabrication and experimental validation. Overall, the MMI-based approach offers a compact, robust, and CMOS-compatible solution for thermo-optic switching, representing a reliable alternative to adiabatic structures for integrated photonic circuits.

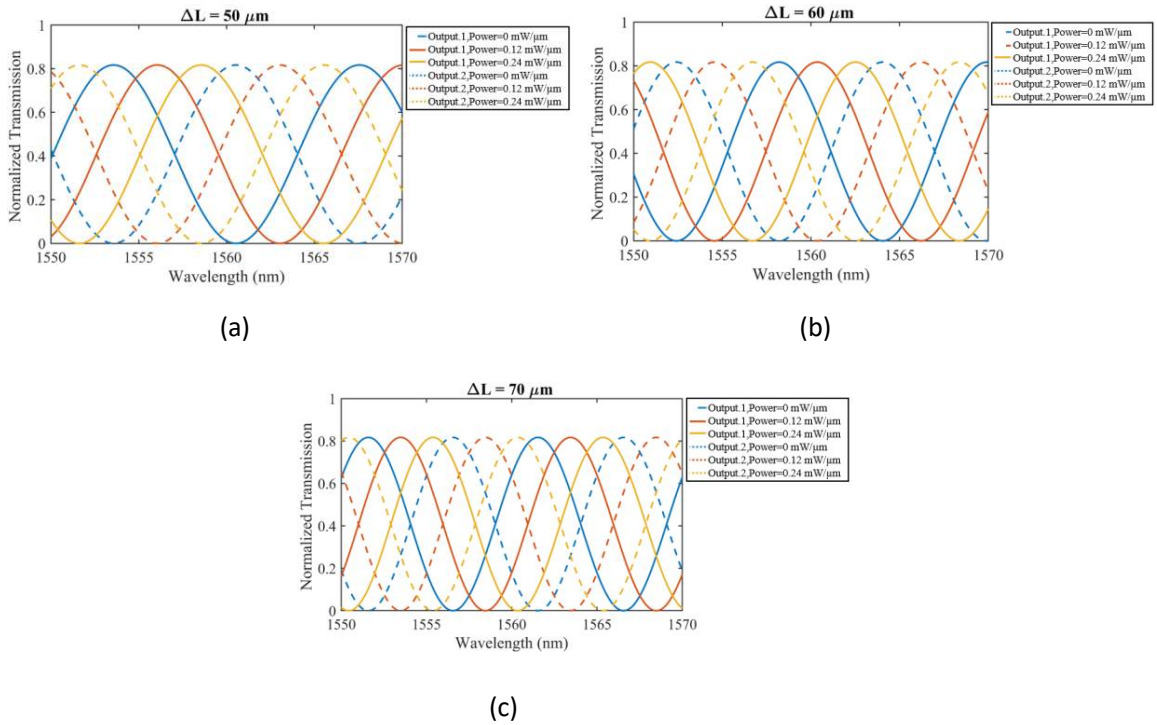

Figure 44. Normalized transmission of the two output ports of the asymmetric Mach–Zehnder thermo-optic switch as a function of wavelength for different arm length differences (ΔL). Results are shown for (a) ΔL = 50 µm, (b) ΔL = 60 µm, and (c) ΔL = 70 µm. Each plot illustrates the switching behaviour at various applied heating powers ranging from 0 to 0.24 mW/µm, showing the wavelength-dependent interference pattern and thermo-optic phase modulation effect in the device.

4.3 Electro-optic microring switch with a graphene modulating layer

4.3.1 Introduction

Another type of optical switch investigated in this work is the graphene-based electro-optic ring switch, which exploits the electrically tunable optical properties of graphene to control the transmission characteristics of a microring resonator. Building upon the operating principles of conventional ring modulators, this architecture leverages graphene's high carrier mobility and broadband optical response to enable efficient electro-optic control with a compact footprint.

Conventional Mach–Zehnder modulators (MZMs) suffer from inherent limitations, including relatively large device footprints and reduced suitability for dense photonic integration. To overcome these constraints, alternative resonant structures such as microring resonators [82] [83] and photonic crystals [84] have been extensively investigated. These resonant devices offer enhanced modulation efficiency and significantly reduced size, making them attractive candidates for high-speed and large-scale photonic integrated circuits. However, their performance is often limited by factors such as finite photon lifetime and restricted modulation bandwidth, motivating further research into improved device concepts.

In parallel, the integration of emerging materials such as graphene into photonic structures has opened new opportunities for the development of advanced electro-optic devices. Owing to its high electron mobility and broadband optical absorption, graphene enables strong and fast modulation of light with reduced power consumption. Early demonstrations of graphene-integrated photonic devices have confirmed the feasibility of combining compact dimensions with broadband and high-speed operation, highlighting the potential of graphene-based ring switches as promising alternatives to conventional silicon photonic modulators and switches. [85] [86]

By optimizing both the device design and the fabrication processes, this work aims to address the limitations of conventional silicon-based modulators and to introduce a new class of high-speed graphene-based optical switches. In contrast to thermo-optic switches, which rely on heat-induced refractive index variations and are therefore inherently limited by relatively slow response times, the proposed graphene-based switch operates through electro-optic modulation of the graphene layer. This mechanism enables substantially faster switching speeds while simultaneously reducing power consumption, making the device a promising candidate for next-generation ultrafast and energy-efficient optical communication systems. [87]

However, due to fabrication limitations and relatively low transmission efficiency compared to other proposed switches, this device was not selected for the current fabrication phase. Nonetheless, the graphene ring switch remains a promising candidate for future research and development, where advanced fabrication techniques could further enhance its performance.

4.3.2 Principle of operation

The physical geometry of a ring switch is shown in Fig. 45.a. The proposed device is composed of two main sections: a ring resonator structure coated with a graphene monolayer placed on top of an Al_2O_3 (aluminum oxide or alumina) dielectric layer, and a set of straight silicon waveguides without graphene. On the bottom of the graphene layer a dielectric material called Al_2O_3 is deposited. This dielectric material not only provides electrical insulation between the graphene and underlying conductive layers, preventing short circuits, but also influences graphene's optical properties, such as its refractive index and absorption. These effects can significantly enhance the modulation efficiency and optical response of photonic devices like modulators and sensors.

The full stack structure consists of a silicon (Si) layer on top of silicon dioxide (SiO_2), followed by a thin layer of amorphous silicon (a-Si:H) above the silicon core. Amorphous silicon was chosen because it can be deposited at lower temperatures, making it compatible with a wider variety of substrates, including those sensitive to heat. Moreover, it offers lower fabrication cost and ease of integration compared to crystalline silicon, while maintaining adequate optical performance for integrated photonic applications. At telecommunication wavelengths around 1.55 µm, hydrogenated amorphous silicon exhibits a high refractive index, typically in the range of n≈3.5 with relatively low optical absorption, enabling strong optical confinement. These optical properties ensure efficient overlap between the guided mode and the graphene modulating layer, making a-Si:H well suited as the top waveguiding layer in the electro-optic microring switch.
The key parameters used in the design of the graphene-based ring switch are summarized in Table 6, and the overall device geometry is illustrated in Fig. 45.b. The structure was chosen to be a rib waveguide because, by properly selecting the width and thickness of the crystalline silicon and hydrogenated amorphous silicon layers, it is possible to achieve a polarization-independent configuration while ensuring single-mode operation for the TE polarization. These parameters define the structural dimensions and material properties essential for achieving optimal optical confinement, resonance behavior, and efficient modulation performance of the device.

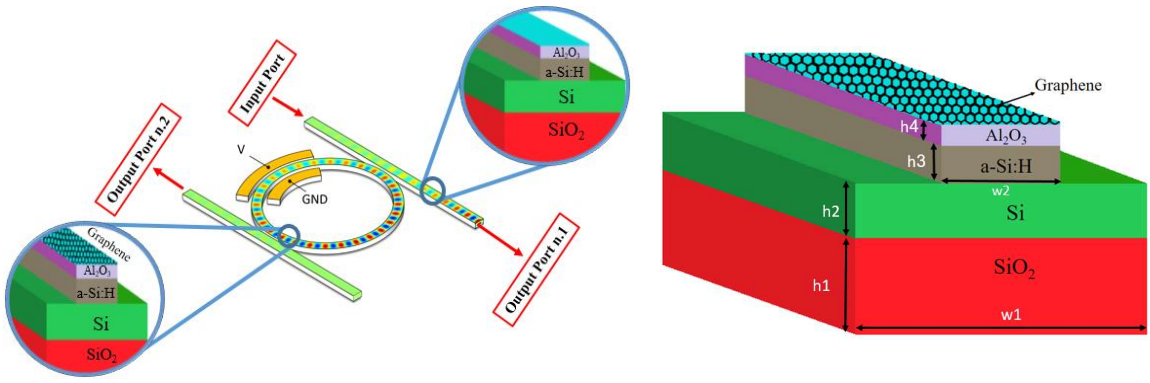

(a) (b)

Figure 45. (a)The geometry of a ring switch. The straight waveguide does not contain graphene, while the ring has a graphene material on a top layer to apply electro-optic effects to the switch. (b)Parameters that are used in a geometry.

Table 6. Parameters of an adiabatic switch

parameter	value	Description
h_1	500 nm	SiO_2 thickness
h_2	100 nm	Si thickness
h_3	120 nm	Amorphous silicon thickness
h_4	50 nm	Al_2O_3 thickness
h_5	0.340 nm	Graphene thickness
W_1	10 µm	SiO_2 width
W_2	450 nm	Amorphous silicon width
Gap	300 nm	Gap distance between straight and bend waveguide

4.3.3 Simulation steps

To simulate the ring switch, we first modeled the coupling between rectangle and ring waveguide in Lumerical using the FDTD method. This step provides the power coupling coefficient between the straight waveguide and the ring over the wavelength range 1.50–1.60 µm (TE mode). Figure. 46.a reports the extracted coupling coefficient for two different gaps. As expected, reducing the gap increases the coupling, since the modal overlap between the bus and ring is stronger at smaller separations; conversely, a larger gap lowers the coupling. This calibrated coupler model is then used in the full ring-resonator simulation for the intended switching behavior.The next step involves obtaining the spatial distribution of charge carriers in the graphene layer as a function of the applied bias voltage. When an external voltage is applied, the Fermi level of graphene shifts, resulting in changes to its optical conductivity and refractive index, as illustrated in Fig. 46.b. This voltage-dependent tunability is what enables active electro-optic modulation in the device.

To model this effect, simulations were performed using the CHARGE and FDE solvers in Lumerical. The CHARGE solver calculates the carrier distribution under different bias voltages, while the FDE solver determines the corresponding changes in the effective refractive index of the optical mode. The resulting data are then used to analyze how the applied voltage influences the optical transmission characteristics of the ring switch.

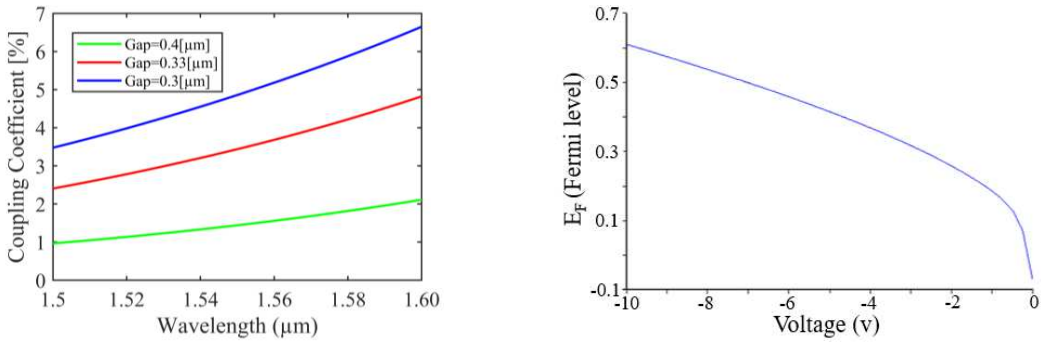

(a) (b)

Figure 46. (a)The coupling coefficient as a function of the wavelength for two different gaps between straight and ring waveguides. (b) Fermi level of graphene monolayer sheet as a function of applied voltage.

In the proposed graphene-based ring switch, a monolayer graphene sheet is integrated on top of the ring waveguide and separated from the silicon core by a thin high-$k$dielectric layer, such as Al_2O_3 or HfO_2.

Together with a metallic electrode, the graphene layer forms a capacitor whose carrier concentration can be controlled electrically. Applying an external bias voltage shifts the Fermi level of graphene, thereby modifying its complex refractive index n_g=n+ik. This change affects both the absorption coefficient and the effective refractive index experienced by the circulating optical mode in the ring. Because the resonance condition of the ring is highly sensitive to variations in the effective refractive index, even small changes in n_{eff} lead to measurable shifts in the resonance wavelength, described by the condition $m\lambda$=$n_{\text{eff}}L$, where m is the resonance order and L is the ring circumference. As a result, the optical power is redistributed between the through and drop ports: when the ring is tuned into resonance with the input wavelength, light couples into the ring and is absorbed or redirected, while detuning the resonance allows the signal to propagate through the bus waveguide with minimal loss. This electrically controlled resonance tuning enables compact and reconfigurable optical switching without requiring physical modification of the waveguide geometry.

Finally, a compact model of the graphene-based ring switch was built in Lumerical INTERCONNECT by integrating the data obtained from the previous simulation steps into the corresponding circuit components. Using an optical network analyzer, the optical transmission at the output ports was analyzed while varying the applied voltage.

As shown in Fig. 47.a, the normalized transmission of the two output ports was simulated for wavelengths range between 1.58 µm and 1.60 µm at a 300 nm coupling gap and 0 V bias. Figure. 47.b illustrates the device performance under different bias voltages. When the applied voltage changes from –10 V to – 6 V, the output power at Port 1 increases from 0.18 to 0.81, while at Port 2 it decreases from 0.83 to 0.21. This opposite behavior clearly demonstrates the electro-optic switching capability of the device, confirming that modulation of the graphene's Fermi level effectively controls the light transmission through the ring.

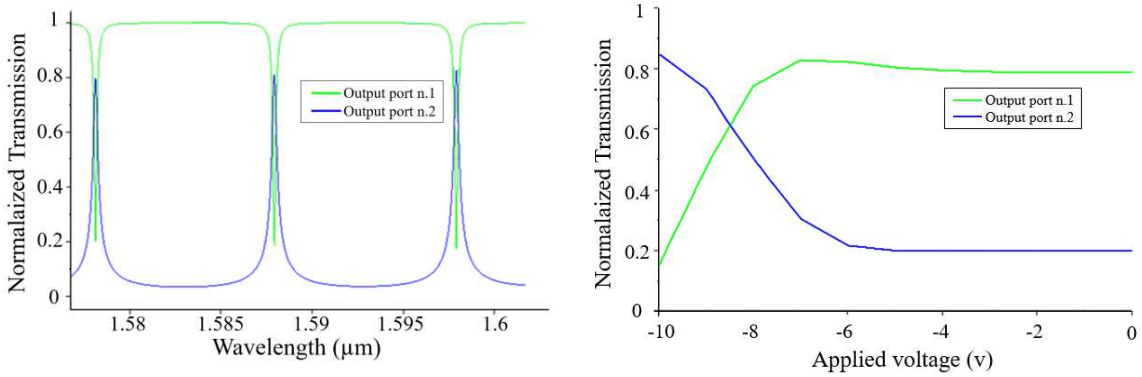

Figure 47. (a)Transmission of two output ports at different wavelengths when gap is 300 nm (b)Transmission at output ports as a function of applied voltage for two output ports at wavelength of 1.55 µm.

4.3.4 Conclusion

To conclude, this study investigated the potential of graphene-based electro-optic ring switches utilizing a narrow waveguide configuration for efficient control of optical signal propagation. The simulation results demonstrate the device's ability to achieve dynamic signal routing by tuning the applied voltage, which directly modulates the optical properties of graphene. These findings confirm the effectiveness and feasibility of such switches, highlighting their promise for next-generation high-speed and low-power photonic systems. However, this design was not advanced to the fabrication stage due to its lower transmission performance compared to the other proposed switches and the increased complexity of the fabrication process. These challenges make the realization of the graphene-based ring switch more demanding with the current cleanroom capabilities, though it remains a promising candidate for future studies as fabrication techniques continue to improve.

4.4 Double layer graphene modulator

With the increasing demand for faster data transmission and higher bandwidth, silicon photonics has emerged as a leading platform for developing compact, low-power, and cost-effective optoelectronic devices. Among these, optical modulators play a crucial role by controlling the amplitude, phase, or polarization of light, enabling advanced signal processing in integrated photonic systems.

In particular, graphene-based electro-absorption modulators have attracted significant attention due to their high modulation speed, low driving voltage, and broadband operation, positioning them as strong candidates for next-generation optical communication systems. In this section, we present the simulation and analysis of a high-efficiency hydrogenated amorphous silicon (a-Si:H) electro-absorption modulator incorporating double-layer graphene. This structure leverages graphene's tunable optical properties and the favorable integration characteristics of a-Si:H to achieve efficient, fast, and compact modulation performance.

4.4.1 Device Structure

The proposed modulator operates as an electro-absorption (EA) device that incorporates a double-layer graphene (DLG) structure embedded within the waveguide core. Technologically, this can be achieved by fabricating the waveguide using both crystalline silicon (c-Si) and hydrogenated amorphous silicon (a-Si:H), with the graphene capacitor positioned between them. This configuration ensures that light strongly interacts with the graphene layers within the core, unlike conventional designs where graphene is placed on the top or bottom surfaces of the waveguide and interacts only with the weak evanescent optical field.

Moreover, high-quality a-Si:H films can be deposited directly on graphene using the Plasma-Enhanced Chemical Vapor Deposition (PECVD) technique at relatively low temperatures (150–300 °C) [88] [89], ensuring good material compatibility and preserving the electrical and optical properties of graphene.

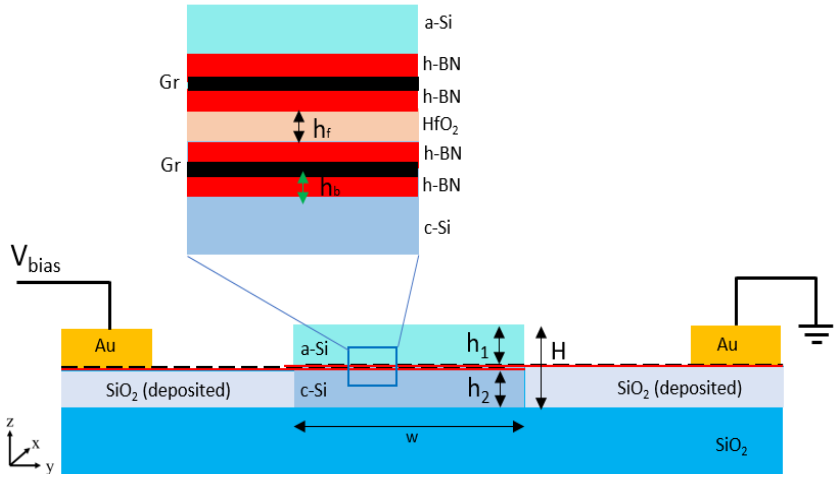

Figure 48. Schematic cross-section (not in scale) of the proposed EA modulator, consisting of a DLG created on a c-Si ridge on SiO_2. An a-Si:H stripe, deposited on top, completes the SOI channel waveguide, which overall has a 500 nm × 220 nm cross section. HfO_2 is the dielectric material placed in between the h-BN layers.

The schematic cross-section of the proposed electro-absorption modulator is illustrated in Fig. 48. The device employs a rib waveguide geometry with a thickness of H = 220 nm and a width of W = 500 nm, designed to support single-mode TE polarization at a wavelength of λ = 1550 nm.

To maintain the high quality and carrier mobility of the graphene layers, each graphene sheet is encapsulated between two layers of hexagonal boron nitride (h-BN). This protective structure minimizes impurities and surface roughness, helping to preserve the intrinsic electronic properties of graphene [51] [90].The dielectric spacer between the graphene layers is composed of hafnium dioxide (HfO_2), deposited using the Atomic Layer Deposition (ALD) technique [91]. Owing to its high dielectric constant (high-k), HfO_2 significantly enhances the graphene–oxide–graphene (GOG) capacitance, thereby improving modulation efficiency [92]. The combination of h-BN and HfO_2 not only provides excellent electrical insulation and voltage stability, but also helps retain the high mobility and low intrinsic doping of the graphene layers, making the structure highly suitable for high-speed and low-power electro-optic applications.

Notably, the augmented breakdown voltage provided by this dielectric architecture, even beyond the regime of full transparency (Pauli blocking), results in an enhanced electro-optic response and a reduction in insertion losses. The Au electric contacts must be sufficiently far from the waveguide center to keep metal absorption, and insertion losses in turn, low [93] [94].

4.4.2 Static Simulation of the modulator

The electro-absorption (EA) modulator was analyzed through comprehensive multi-physics simulations, which included:
(a) Calculating the two-dimensional electric field distribution across the waveguide cross-section under different bias voltages, both in static and dynamic conditions;
(b) Evaluating the resulting shift in the Fermi level of the graphene layers; and
(c) Determining the modification of the optical field propagation using the Finite Difference Method

(FDM).

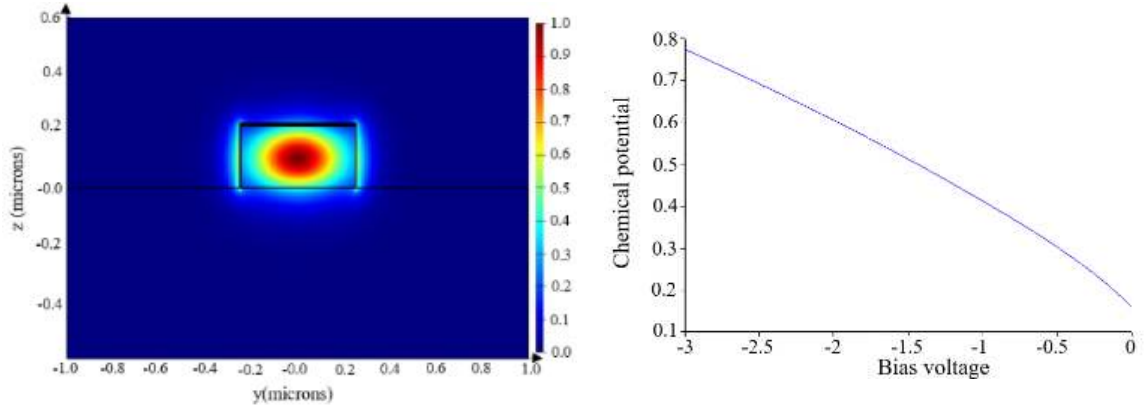

(a) (b)

Figure 49. (a) Electric field distribution for the propagating TE mode, (b) Variation in the chemical potential of the bottom Graphene sheet as a function of the bias voltage.

From a physical standpoint, graphene differs significantly from conventional optical materials in two key aspects. First, it is an ultra-thin material, consisting of a single atomic layer. Second, its behavior is best described by its surface conductivity rather than a bulk permittivity. As a result, in numerical simulations, graphene can be modeled as a two-dimensional (2D) material, eliminating the need for an excessively fine computational mesh. This approach allows for accurate and efficient simulations while significantly reducing computational time.The electrical and optical parameters of the materials used in the simulations are summarized in Table 7.

The electric field distribution corresponding to the fundamental TE mode is shown in Fig. 49.a. This result was obtained for a configuration with 220 nm of crystalline silicon (c-Si) and no a-Si:H layer (0 nm), placing the double-layer graphene (DLG) structure at the top of the waveguide. Under these conditions, the simulation yielded an attenuation of 0.128 dB/µm at zero bias, representing the intrinsic optical loss of the device before electrical modulation is applied.

Table 7. Properties of used materials.

Material	Refractive index	Work function (eV)
a-Si:H	3.57	4.15
c-Si	3.47	4.15
h-BN	1.98	4.6
HfO_2	1.87	2.9
SiO_2	1.44	0.95

To study the effect of applying bias to the graphene layers, an isothermal steady-state electrical simulation was performed. In this setup, the top graphene (Gr) layer was grounded, while a DC voltage sweep was applied to the bottom Gr layer. By analyzing the band structure, the Fermi level shift was extracted as a function of the applied voltage, as shown in Fig. 49.b. When a –3 V bias was applied, a clear change in the in-plane permittivity (ε‖) was observed, resulting in a reduction of optical attenuation down to approximately 0 dB/µm, confirming the effective electro-absorption modulation

behavior of the device.

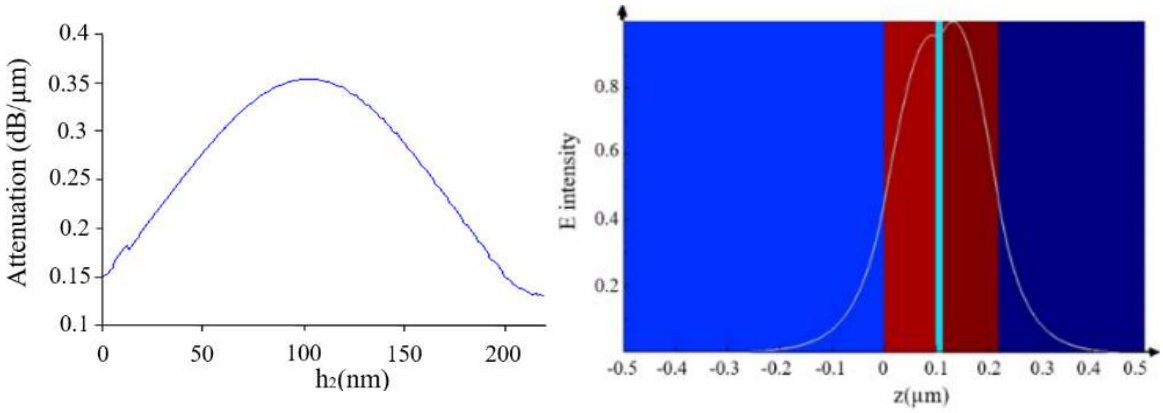

(a) (b)

Figure 50. (a) Simulated attenuation as a function of h_2 (thickness of c-Si layer) to find the best position for the Gr capacitor. (b) Electric field intensity as a function of the position of the Graphene-on-Graphene stack along the z-axis.

To evaluate how the position of the graphene/oxide/graphene (GOG) structure affects the device performance, a set of parametric simulations was carried out. The total waveguide thickness was kept constant at 220 nm, while the relative thicknesses of the crystalline silicon (c-Si) and hydrogenated amorphous silicon (a-Si:H) layers were varied.

As shown in Fig. 50.a, the attenuation was analyzed as a function of h_2, which represents the thickness of the c-Si layer (see Fig. 48). The results indicate that the optimal position of the graphene capacitor is near the mid-height of the waveguide, where the optical field intensity reaches its maximum, as illustrated in Fig. 50.b.

To further enhance the modulation depth, the thicknesses of the h-BN and HfO_2 layers were optimized, as reported in Fig. 51.a and .b. The final optimized parameters providing the best overall performance are summarized in Table 8. It is important to note that small variations in the thickness of h-BN and HfO_2 do not significantly affect the overall modulation performance, indicating a degree of fabrication tolerance in the design.

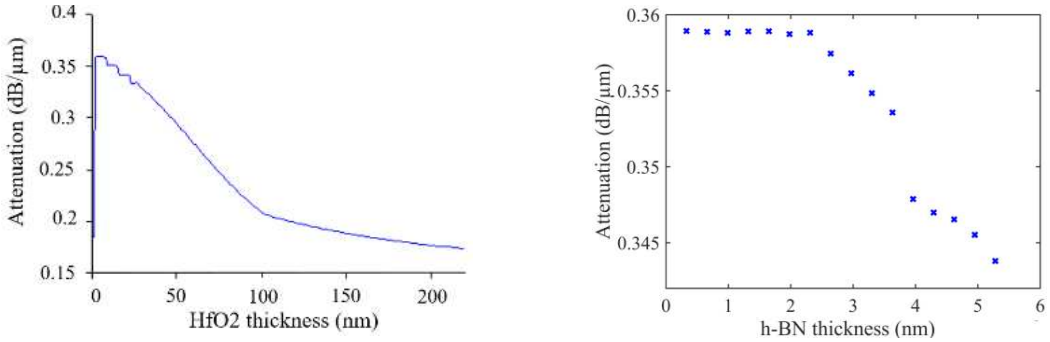

(a) (b)

Figure 51. (a) Attenuation dependence on h_f (HfO_2 thickness) (b) Attenuation dependence on h_b (h-BN thickness) for different layers of h-BN.

Table 8. Parameters that are used in modulator.

Parameter	Description	Best position
h_1	a-Si:H thickness	105 nm
h_2	c-Si thickness	106 nm
h_b	h-BN thickness	0.33-2.31 nm
h_f	HfO_2 thickness	2-8 nm

4.4.3 Dynamic simulation results

Figure. 52.a shows the attenuation at wavelength of 1550 nm light wave through the optimized modulator as a function of the applied bias voltage (Vbias). For the current design, a 1 µm-long device achieves a modulation depth of 0.34 dB when Vbias = –3 V. Transient electrical simulations were also performed to analyze the device's dynamic response, considering parasitic resistances (mainly in the graphene layers connecting the Au contacts) and parasitic capacitances (arising from the graphene–insulator–graphene structure). These parasitic elements influence the speed and frequency response of the modulator.

The results of time-dependent Fermi level and carrier distributions were then used to calculate the dynamic optical behavior. At high switching frequencies, power dissipation can cause localized heating, slightly changing the silicon refractive index due to the thermo-optic effect. However, the operating principle of the device, based on modulation of absorption in the graphene capacitor, and its optical design, allows it to continue working properly. This is also shown in Fig. 52.a, where the attenuation as a function of voltage is reported for comparison at 400 K as well, which might be considered a practical operation limit for a photonic device.

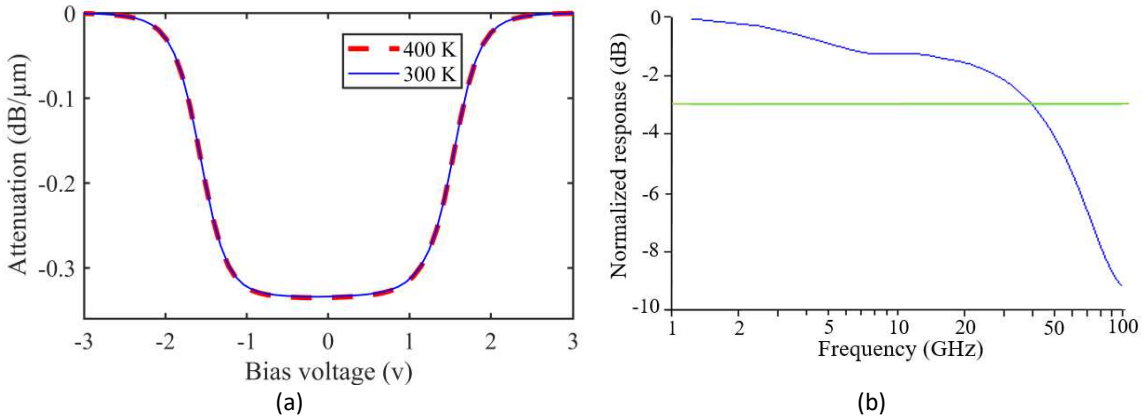

Figure 52. (a) Static electro-optical response of the device for bias voltage Vbias varying from -3 V to 3 V, calculated at 300 K and 400 K; (b) dynamic electro-optical response of the device. It shows the relative electro-optical response of the modulator as a function of frequency obtained by applying pulses of -2.5 V amplitude. The measured -3 dB bandwidths of the device is 39.5 GHz.

Figure. 52.b shows the frequency response of the transmitted signal, obtained by applying a –2.5 V step voltage to the modulator and performing a Fast Fourier Transform (FFT) on the output signal. The results reveal a –3 dB bandwidth of 39.5 GHz when the graphene–oxide–graphene (GOG) structure is

embedded within the waveguide core, indicating high-speed operation. When the GOG structure is positioned at the top of the waveguide, the bandwidth decreases to 32 GHz, due to the weaker overlap between the optical mode and the active graphene region. This demonstrates that embedding the GOG capacitor within the core significantly improves the modulation speed and efficiency.

To evaluate the data transmission capability of the proposed modulator, time-domain simulations were performed to generate an eye diagram for a 50 µm-long device using the Interconnect simulation environment, which is specialized for photonic integrated circuit (PIC) analysis. In the virtual setup shown in Fig. 53, a random pattern generator (PG) is used to generate the electrical drive signal, which modulates the optical carrier through the electro-absorption (EA) modulator. The modulated optical signal is then detected by a high-speed PIN Photodetector with responsivity of R = 1 and considering a thermal noise of 1.4×10^{-11}A/Hz connected to an oscilloscope for signal analysis.

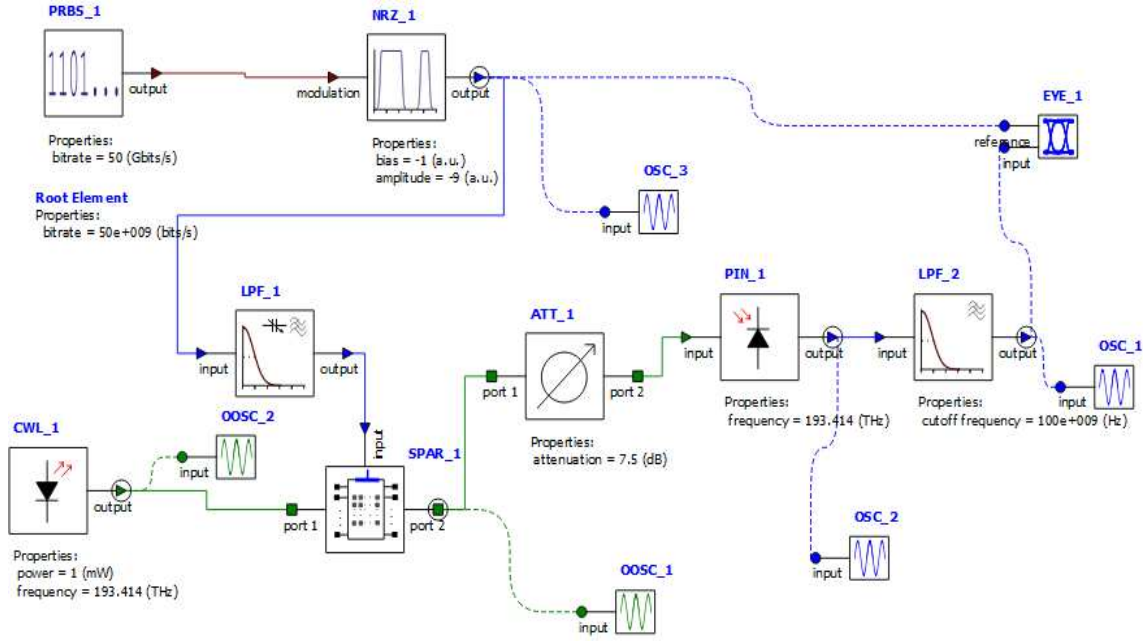

Figure 53. Block diagram of the virtual simulation setup used for dynamic analysis and eye-diagram generation of the electro-absorption modulator, including the PRBS–NRZ electrical drive, CW laser source, EA modulator modelled with S-parameters, optical detection, filtering stages, and eye-diagram analyzer.

The electrical input signal consists of a pseudorandom binary sequence (PRBS) in non-return-to-zero (NRZ) format at a given data rate (Gb/s), with the voltage varying between −1 V and −3 V. The optical source is a continuous-wave laser operating at a wavelength of 1550 nm (f = 193.414 THz) with an output power of 1 mW.

To characterize the frequency response of the device, a low-pass filter (LPF) is included in the simulation to extract the −3 dB cutoff frequency as a function of the applied voltage. The electrical S-parameter response of the system is modeled using an SPAR element. Eye diagrams are generated using an eye-diagram analyzer connected at the output of a Bessel filter, while the original NRZ signal from the pulse generator is used as a reference for clock recovery and compensation of propagation

delays between the transmitter and receiver. Finally, an attenuator element is included to account for insertion losses present in the system.

Figure. 54 shows the resulting eye diagrams for a 40 Gb/s signal, obtained using input pulses varying between –1 V and –3 V. The comparison highlights that when the GOG capacitor is placed at the center of the waveguide, the modulator achieves a dynamic extinction ratio (ER) of 3.17 dB, whereas positioning it at the top results in a lower ER of 1.2 dB. These results confirm the superior modulation efficiency and signal integrity of the optimized device configuration.

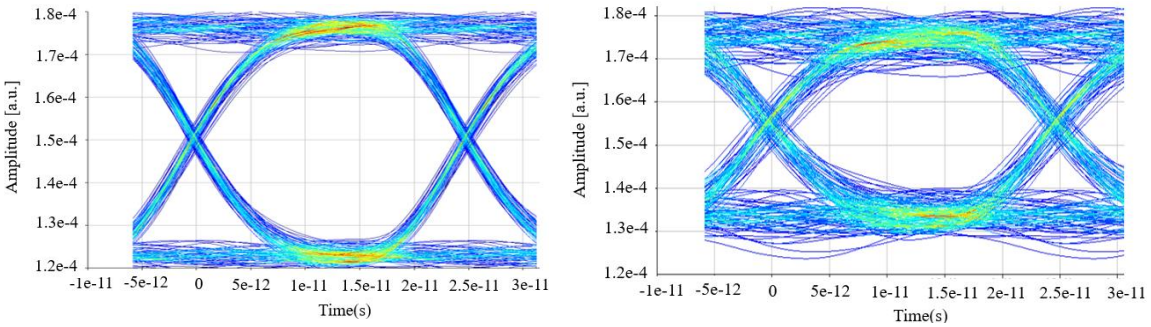

Figure 54. Eye diagrams of the optical signal obtained at 1550 nm for the 50 µm long EA modulator at 40 Gb/s (5ps/div) for (a) GOG in the middle and (b) GOG at the top of the waveguide.

4.4.4 Fabrication hints

The device can be fabricated starting from a standard SOI wafer, with the required thickness of the Si device layer. After defining the bottom part of the waveguide, the lower h-BN/Gr/h-BN stack is formed through a hot-pick-up technique, and then properly defined with a mask/etch process. Afterward, HfO_2 is deposited by ALD and defined in turn. The second stack of h-BN/Gr/h-BN (top) is then laid, and a-Si:H is deposited by PECVD and soon defined to form the top part of the waveguide. Finally, after opening h-BN, Au contacts are formed. The quality of materials can be monitored consistently by Raman spectroscopy during the intermediate steps. It is worthwhile highlighting that, while alignment tolerances in silicon processing are well-established, the industrial-scale integration of 2D materials presents unique challenges. These challenges encompass the development of scalable transfer techniques, accurate patterning methods, and reliable yield characterization. Addressing them at industrial scale is critical for the successful commercialization of 2D material–based devices.

The proposed architecture is based on a double h-BN–SLG–h-BN heterostructure, whose large-area implementation has already been demonstrated by encapsulating CVD-grown single-layer graphene within h-BN, as reported in [95]. In that study, it was shown that, through appropriate encapsulation and cleaning protocols, room-temperature mobilities above 10,000 $cm^2\ V^{-1}\ s^{-1}$ can be achieved in CVD-grown SLG transferred using a conventional and scalable PMMA-assisted wet process. Moreover, the encapsulation of SLG within h-BN has enabled the fabrication of functional devices, such as the THz detector presented in [96]. For instance, in that work, SLG was integrated between h-BN layers using well-established procedures: both h-BN and SLG flakes were prepared by micromechanical exfoliation on intrinsic Si substrates with a 285 nm SiO_2 layer and sequentially assembled (top h-BN, SLG, bottom h-BN) with poly (dimethylsiloxane) (PDMS) and poly-carbonate (PC) stamps.

4.4.5 Comparison

Table 9 summarizes the main performance metrics of various double-layer graphene electro-absorption modulators reported in the literature and compares them with the device proposed in this work. While the extinction ratios achieved are comparable to those of previously reported graphene modulators, including devices with similar geometries such as in [51] , the proposed modulator simultaneously offers a wider bandwidth, a high extinction ratio, and a more compact footprint. Moreover, it exhibits the highest modulation depth among the devices considered, highlighting the effectiveness of the proposed design.

Table 9. Comparison of Reported Electro-Absorption (EA) and Electro-Optic (EO) Modulators Based on Graphene and Other Materials (MD=modulation depth, BW=bandwidth, ER=extinction ratio).

Ref	MD (dB/μm)	Type	Wavelength (nm)	Size (μm×μm)	Structure	BW (GHz)	ER (dB)	Mode	Year
This work	0.34	EA	1550	50×0.5	Double-layer graphene, h-BN –HfO_2– h-BN	39.5	3.17	TE	2026
[51]	0.037	EA	1550	60×0.45	Double-layer graphene	39	4.4	TM	2021
[56]	0.137	EA	1550	120×0.65	SOI waveguide (air-clad, DLG, 20 nm SiN spacer	29	1.7	TE	2019
[55]	0.165	EA	1550	1.2×18.09	Double-stripe Si_3N_4	30.6	---	TE/TM	2017
[97]	28 dB	EO	1555	1×0.3	Graphene on Si_3N_4 waveguide ring resonator	30	---	TE	2015
[53]	0.16	EA	1537	40×2	Double-layer graphene optical modulator	1	---	TE/TM	2011
[98]	0.2–0.3	EA	1550	~1 × <1	Hybrid plasmonic ridge waveguide	70	35	-	2024
[99]	15 dB	EA	1300	50×5	GaAs	2.5	---	TE	2025

4.4.6 Conclusion

In this section, a photonic electro-absorption modulator integrating a buried active structure based on a graphene–insulator–graphene (GIG) capacitor has been investigated to enhance the optical response of the device. The proposed architecture exploits the placement of the graphene capacitor at a position where the electric field of the propagating TE mode is maximized, thereby strengthening light–matter interaction. In contrast to earlier demonstrations of double-layer graphene modulators, this work introduces a more rigorous physical modeling approach combined with a systematic optimization of both dielectric and structural parameters.

Although the optimized structure cannot be realized using standard silicon photonics technology alone, it can be fabricated by incorporating the deposition of hydrogenated amorphous silicon (a-Si:H) into the process flow. This approach enables the embedding of graphene within a rib waveguide composed of crystalline silicon (c-Si) and a-Si:H. In particular, experimentally feasible integration

routes based on low-temperature PECVD for a-Si:H deposition and atomic layer deposition (ALD) of high-k dielectrics are highlighted, allowing the simultaneous achievement of enhanced modulation strength and wide bandwidth within a compact footprint.

By positioning the graphene capacitor at the optimal location within the waveguide, numerical simulations predict an attenuation of 0.34 dB/μm at an operating wavelength of 1550 nm. Furthermore, a realistic electro-optic bandwidth of 39.5 GHz is estimated using HfO_2 as the dielectric spacer, together with h-BN encapsulation of the graphene layers to preserve high carrier mobility. The proposed modulator is capable of supporting data transmission rates of up to 40 Gb/s, achieving an extinction ratio of 3.17 dB.

5. Fabrication and experimental result

5.1 Computer Aided Design of the photolithography mask for the adiabatic splitter and switch

5.1.1 Luceda IPIKISS Introduction

To design the adiabatic structures with nanometer-scale precision, the Luceda IPKISS platform was used to generate the CAD files that were later prepared for fabrication by IMEC. In this section, we briefly introduce the software environment and explain how it was employed to design the adiabatic structures.

IPKISS is a photonic design framework that provides advanced tools for layout generation, device simulation, and photonic circuit implementation. Luceda also offers an online training resource, the Luceda Academy, which provides step-by-step guidance for learning the software from the basics. Before working with IPKISS, it is essential to install the appropriate design kit. The design kits enable all IPKISS features such as the Canvas environment, parameterized components, and the scripting interface. For example, the si_fab design kit provided by Luceda appears by default in the “Design Kits” section of the control panel.

Since IMEC is the foundry responsible for fabricating our design, the IMEC Process Design Kit (PDK) was used. This PDK includes all the process-compatible components required to build the switch, such as standard silicon waveguides, heaters, and routing elements defined for specific wavelength bands. However, the IMEC library did not include a taper waveguide suitable for the adiabatic structure. For this reason, we first designed the device using standard waveguide elements in IPKISS and later converted these sections into tapered geometries using KLayout during the final mask preparation.

A detailed list of the components used in the IPKISS design environment, along with their relevant properties, is provided in the following section.

5.1.1.1 Thermal Phase shifter

Thermal phase shifters are employed to adjust the optical phase without introducing additional propagation loss. In this design, the phase shifter consists of a thin metal heater (tungsten) placed on top of the silicon waveguide. When electrical power is applied, the generated heat locally increases the refractive index of silicon through the thermo-optic effect, producing the required phase shift.

The silicon waveguide beneath the heater is designed to support single-mode operation in the C- or O-band. One example of the phase shifters used in the circuit is shown in Fig. 55. In our layout, the length of each individual phase shifter was set to 120 µm. To achieve a larger and more controllable phase shift, two identical phase shifters were placed next to each other, effectively increasing the total heated region and enhancing the phase-modulation capability.

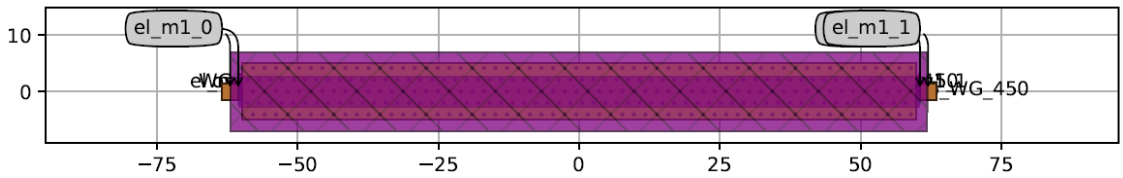

Figure 55. Layout of the IMEC thermal phase shifter, consisting of a tungsten (W) metal heater positioned above a 450 nm full-etch silicon waveguide (WG_450).

5.1.1.2 Grating coupler

The fiber grating coupler (FGC) is the component used to couple light between an optical fiber and the integrated photonic circuit. This coupling approach is particularly advantageous during wafer-level testing, as it allows optical access to the device without requiring chip dicing or edge polishing. Grating couplers, however, typically offer a narrower operational bandwidth compared to edge couplers and exhibit polarization dependence, with different efficiencies for TE and TM modes. Figure. 56 shows an example of a grating coupler from the IMEC PDK, which was used in the design and testing of our fabricated devices.

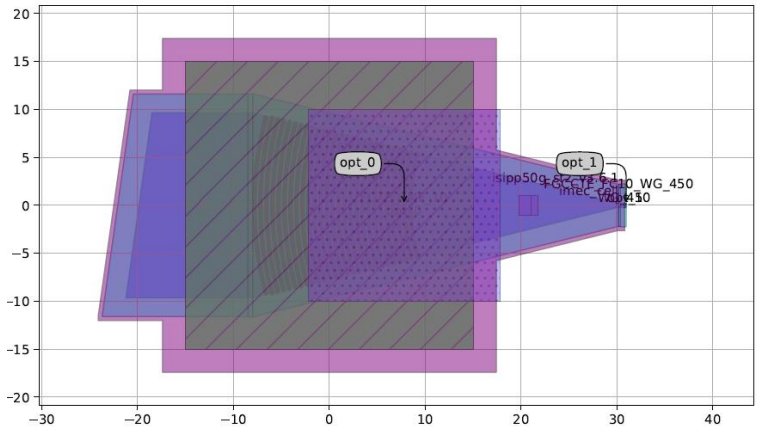

Figure 56. CAD layout of the IMEC partial-etch grating coupler designed for TE-polarized operation in the C- or O-band. The structure includes the grating region, apodized transition section, and the underlying 450 nm silicon waveguide, enabling efficient vertical coupling between an optical fiber and the on-chip waveguide.

5.1.1.4 Bond pad

Bond pads serve as the electrical interface between the on-chip components and external instrumentation, enabling connections via probe needles or wire bonding. The pads provided by IMEC incorporate an aluminum capping layer and are available in multiple geometries and configurations. In this design, the two-layer bond pads with dimensions of 80 µm × 60 µm are employed, as illustrated in Fig. 57 Each pad includes four ports per metal layer, supporting reliable electrical access and integration within the circuit.

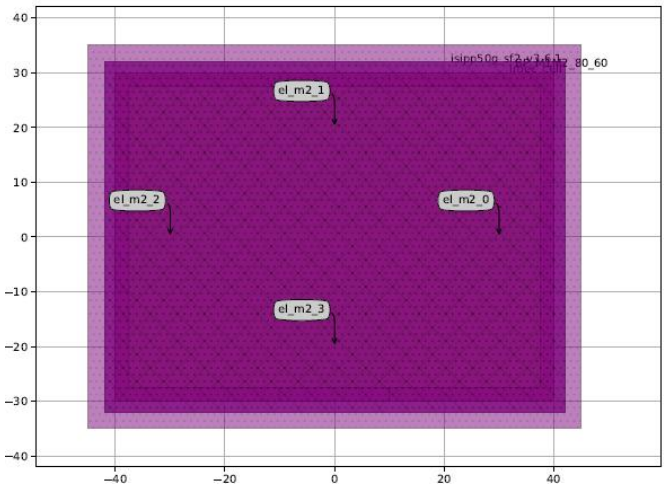

Figure 57. Layout of the IMEC bond pad, featuring an 80 µm length and 60 µm width. The pad includes multiple metal-layer access points to support wire bonding and electrical probing within the photonic integrated circuit.

5.1.1.5 Waveguide

In the circuit layout, a silicon waveguide with a width of 450 nm is employed, as illustrated in Fig. 58. Because the IMEC PDK geometries in Luceda IPKISS cannot be directly modified, the waveguide width is subsequently tapered in KLayout to achieve a minimum width of 100 nm at one end. This modification enables the implementation of an adiabatic taper required for efficient mode transformation. The resulting taper section has a total length of 245 µm.

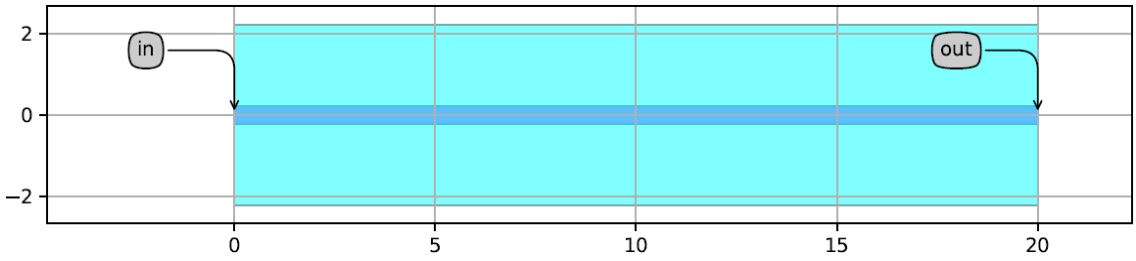

Figure 58. Silicon waveguide with a width of 450 nm, designed for single-mode operation in the C- or O-band.

5.1.1.6 Bent waveguide

To implement waveguide bends using the IMEC PDK, the standard bend element for the WG_450 full-etch silicon waveguide was employed as it is shown in Fig. 59. This bend is defined for a waveguide width of 450 nm and incorporates a bend radius of 10 µm, ensuring low-loss propagation and compatibility with the design rules of the platform.

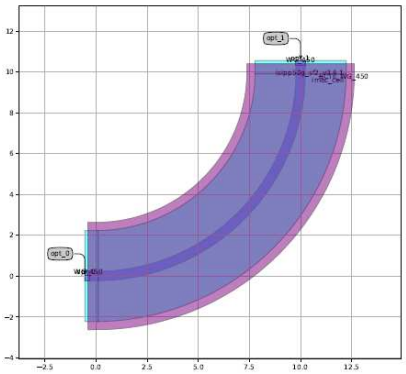

Figure 59. IMEC standard waveguide bend for a 450-nm-wide silicon waveguide, designed with a bend radius of 10 µm.

5.1.2 Adiabatic passive splitter

The passive adiabatic Y-splitter consists of a rectangular input waveguide, three parallel tapered waveguides forming the adiabatic transition region, and two S-bent output waveguides. The device integrates three grating couplers: one at the input for laser coupling and two at the outputs for monitoring the transmitted optical power. The splitter is fabricated in silicon (n = 3.4732), with SiO_2 used as both the lower and upper cladding layers. Figure. 60 shows the final CAD layout of the 3 dB adiabatic splitter, which was designed and included in the mask design submitted for fabrication.

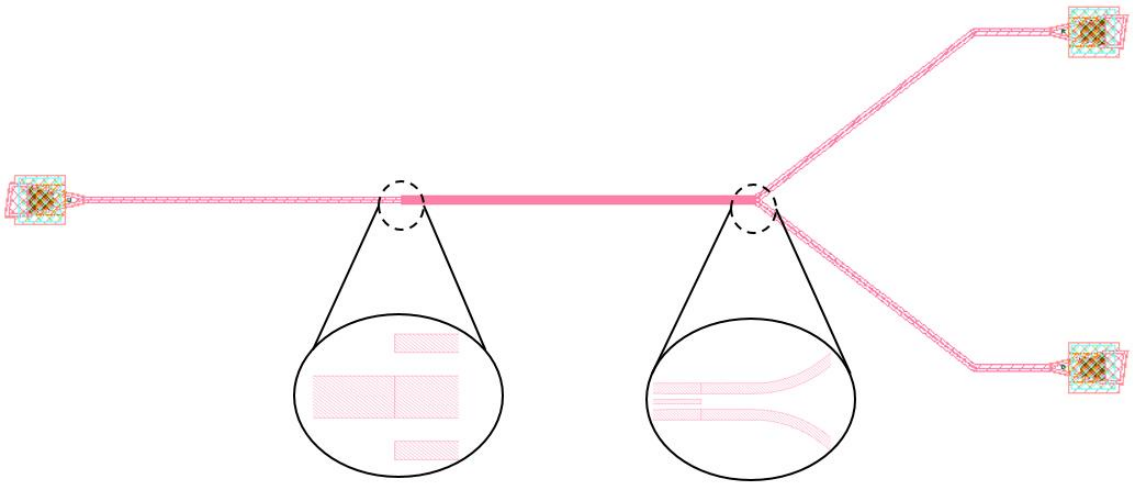

Figure 60. CAD layout of the passive adiabatic splitter, featuring three tapered waveguides with a taper length of 245 µm.

5.1.3 Adiabatic active thermo-optic switch

Figure. 61 presents the CAD layout of the adiabatic thermo-optic switch, designed using Luceda IPKISS and KLayout. The layout highlights the placement of metal heaters above the tapered and S-shaped waveguide sections, where local heating induces a refractive index change in the silicon core through the thermo-optic effect. The adiabatic taper geometry ensures broadband operation and improved

tolerance to fabrication variations, making the switch suitable for large-scale photonic integrated circuit (PIC) applications.

The device consists of a central straight waveguide and two symmetrically bent output waveguides, connected through tapered regions that enable adiabatic mode evolution. Two thermo-optic phase shifters are positioned adjacent to the taper region to generate the required phase shifts for switching. The lateral separation between each waveguide and its corresponding heater is set to 9 µm, enabling efficient thermal coupling while maintaining low propagation loss.

Electrical access is provided through three bond pads: two dedicated pads for individually driving the heaters, and a third shared pad that serves as a common ground. Activating either heater by applying voltage enables selective routing of optical power to the corresponding output port.

The geometric parameters of the switch are chosen to balance optical confinement, coupling efficiency, and thermal performance. For example, the taper tip width of 200 nm and the 250 nm spacing within the adiabatic region strongly influence the coupling characteristics, while the heater width of 450 nm and the 9 µm waveguide–heater separation are optimized to achieve effective phase shifting with reduced power consumption. The precise alignment of waveguide segments and heaters in the CAD layout reflects the optimization steps performed during the simulation phase and is critical for achieving low-loss, thermally efficient switching behavior after fabrication.

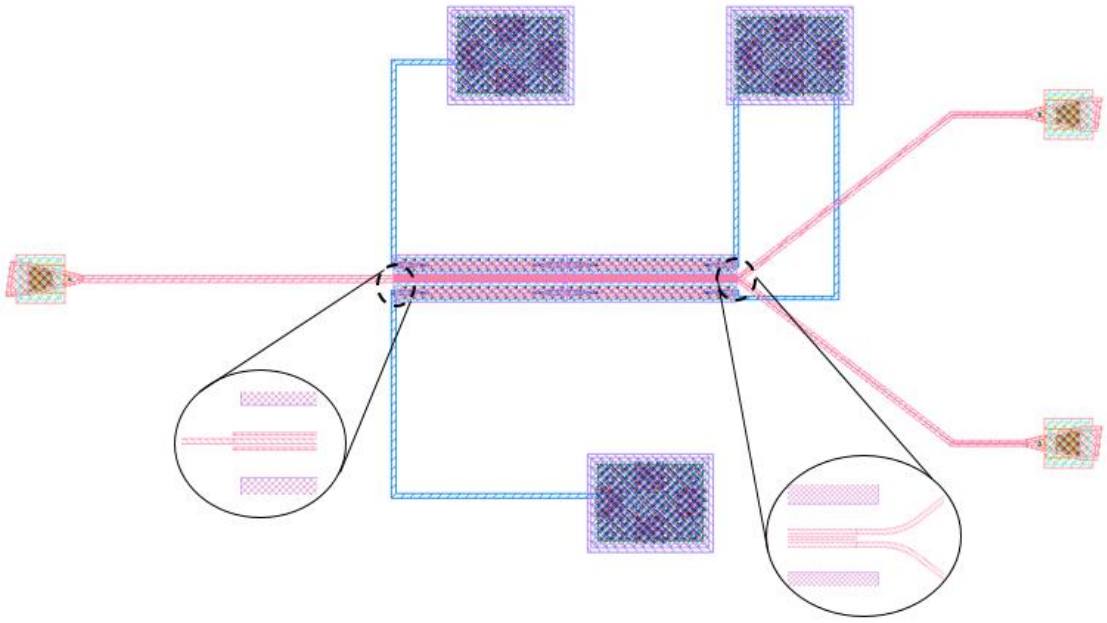

Figure 61. CAD layout of the adiabatic thermo-optic switch, showing the tapered waveguide region, integrated heaters, and electrical bond pads.

5.1.4 Conclusion

In this chapter, the fabrication-oriented design and implementation of the adiabatic thermo-optic switch were presented. The Luceda IPKISS platform, together with KLayout and the IMEC Photonic

Design Kit, was used to create complete and foundry-compliant CAD layouts. All key components, including waveguides, adiabatic tapers, thermal phase shifters, grating couplers, and bond pads, were successfully integrated into the final design.

Both the passive adiabatic splitter and the active thermo-optic switch were translated from optimized simulations into layouts suitable for fabrication. These results demonstrate that adiabatic thermo-optic switches can be reliably fabricated using standard silicon photonics processes, providing a solid basis for experimental characterization and for the development of scalable optical switching systems.

5.2 Fabrication and characterization of Multi-Mode Interference (MMI) Mach–Zehnder Interferometer thermo optic switch

5.2.1. MMI passive splitter

This section describes in detail the fabrication process of the multimode interference (MMI) switch developed in our cleanroom facility, as well as the results of its passive splitter characterization. The fabrication was carried out on a silicon-on-insulator (SOI) wafer using laser-writer photolithography with a positive photoresist, followed by pattern transfer through reactive ion etching (RIE) in an Oxford PlasmaPro 80 system. The main process steps included wafer cleaning, adhesion layer coating, photoresist coating, direct-write lithography, post-exposure baking and development, dry etching, resist removal, and final cleaning.

5.2.1.1 Photolithography process

The process began with wafer preparation to ensure a clean and particle-free surface. The SOI wafer was washed sequentially in acetone, isopropanol (IPA), and deionized water, followed by nitrogen drying to remove any remaining contaminants. To improve adhesion, an HMDS adhesion promoter was first spin-coated at 5000 rpm for 60 seconds. Then, the positive photoresist (OIR 906-12) was applied using the same spin parameters to achieve the desired thickness. A soft bake at 90 °C for one minute was then performed to remove residual solvents and stabilize the photoresist layer.

The patterns for the input and output waveguides, as well as the MMI region, were written using a direct-write laser lithography system. The exposure parameters, such as the laser dose (120 mJ/cm^2) and focus, were carefully optimized to obtain sharp and well-defined features on a sample. After exposure, the samples were developed in FujiFilm OPD 4262 for various durations to determine the optimal development time. The best result was achieved with a 40 second development, which produced a clean and uniform pattern transfer.

The final fabricated device is shown in Fig. 62, demonstrating strong agreement with the CAD layout designed in KLayout and confirming the successful execution of the fabrication process following the photolithography step. The tapered regions and waveguide sections are smooth and well defined, indicating that the lithography process can reliably achieve a resolution of 1 µm with high precision.

Furthermore, the critical design dimensions used for fabrication closely match the simulation parameters specified in Table 4 in Section “4.2.1, MMI Passive Splitter”.

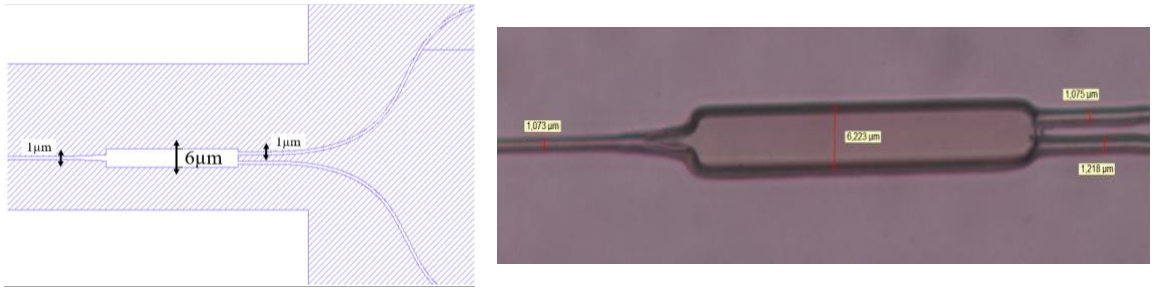

(a) (b)

Figure 62. (a)CAD layout of the 1×2 MMI splitter with a 1 µm-wide input and output waveguide, designed in KLayout software. (b) Optical microscope image of the fabricated MMI splitter pattern produced using the laser-writer photolithography system, showing a good match with the designed geometry. The MMI region width is approximately 6 µm, and the waveguide widths are around 1 µm, consistent with the design specifications.

5.2.1.2 Waveguide etching optimization

To optimize the etching process of the optical switches, a single CAD layout containing eight identical devices was designed and patterned simultaneously on the same SOI substrate using the laser writer. This approach allowed direct comparison of the etching results across multiple devices fabricated under identical conditions. The analysis focused on both the 1 µm-wide single-mode waveguides and the 6 µm-wide MMI regions, each with a 1.5 µm height, corresponding to the full thickness of the silicon device layer on the SOI wafer, as shown in Fig. 63. The main goal was to achieve vertical sidewalls, which required a strongly anisotropic etching process.

The first set of experiments utilized Inductively Coupled Plasma Reactive Ion Etching (ICP-RIE) in the Oxford PlasmaPro NGP80 system with typical silicon etching gas mixtures. Sulfur hexafluoride (SF_6) was selected as the primary etchant due to its high etch rate and strong chemical reactivity with crystalline silicon, although it tends to produce isotropic profiles [100]. To improve anisotropy and protect the waveguide sidewalls during etching, oxygen (O_2) was added to the plasma. However, an excessive amount of oxygen can attack and damage the photoresist, so a careful trade-off is required to ensure both good profile control and sufficient resist durability.

Three etching processes were tested as it groups in table 10:

Table 10. Reactive Ion Etching (ICP-RIE) process parameters.

Process	RF power(w)	ICP power(w)	SF_6(sccm)	O_2(sccm)	etching time(s)	Etch depth(µm)	etch rate(nm/s)
A	7	150	20	3.5	60	1.25	20.8
B	7	125	20	5	60	0.75	12.5
C	7	125	20	5	120	1.4	12.5

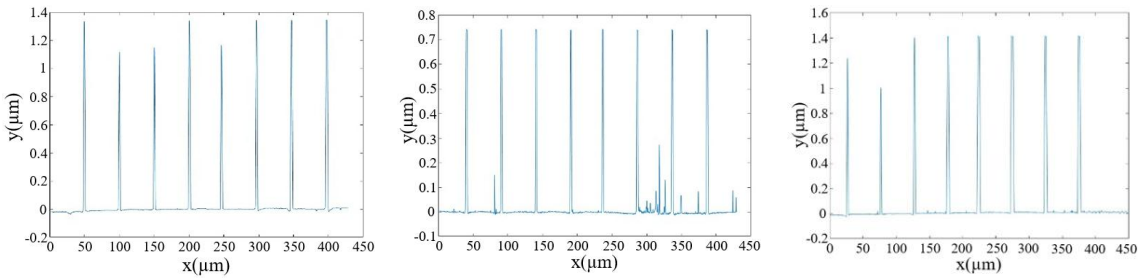

Figure 63. Profiles measured with a profilometer of etched waveguides obtained by RIE using a SF_6/O_2 gas mixture: (a) process A, (b) process B, and (c) process C.

Although the three processes gave different etch depths and rates, they all showed non-uniform and mostly isotropic etching, meaning the material was removed both vertically and sideways. This caused extra etching on the sides, especially in the narrow 1 µm-wide waveguides, as shown in Fig. 64. Consequently, the waveguides did not reach the planned 1.5 µm height, and the top parts became slightly thinner, reducing the accuracy of their shape and their ability to guide light properly. The SEM images in Fig. 64 clearly show this isotropic behavior, where the sidewalls are not straight and some unwanted side etching is visible.

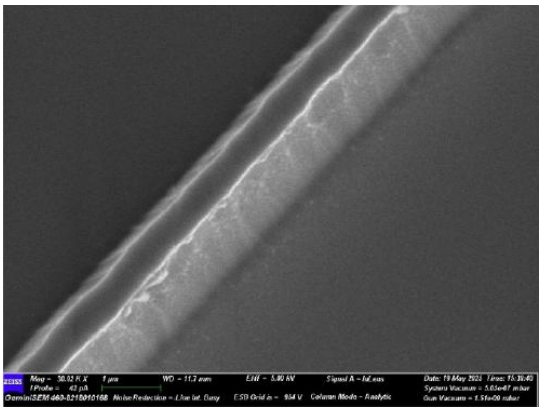

Figure 64. SEM image of a silicon waveguide etched using a standard reactive ion etching (RIE) process. The image reveals an isotropic etching profile, where the sidewalls are not perfectly vertical, indicating simultaneous lateral and vertical material removal during the etching process.

These results revealed the limitations of standard SF_6/O_2 plasma recipes for performing the high quality etching in silicon and highlighted the need for a more anisotropic approach. To overcome this issue, for the next fabrication step the Deep Reactive Ion Etching (DRIE) process based on the Bosch technique was employed [101]. The Bosch process is a cyclic etching method designed to achieve highly anisotropic sidewalls. Each Bosch etching cycle is composed of three main phases that repeat sequentially to achieve the desired etch depth and sidewall quality.

Deposition phase:

In the first step of the cycle, C_4F_8 gas is added to the chamber to form a thin protective polymer layer on all surfaces of the etched pattern. This coating works like a shield that covers both the bottom and the sidewalls. Its main purpose is to protect the sidewalls from being etched, helping to keep the structure straight and well-defined.

Break phase:

A short SF_6 gas pulse is then added to remove the protective polymer only from the bottom of the etched areas. The ions in the plasma hit the surface vertically and physically clean the bottom, while the fluorine atoms in the gas help to remove the remaining polymer through a soft chemical reaction. During this step, the RF power is adjusted to improve the vertical direction of the etching.

Etching phase:

In the last step of each cycle, another SF_6 gas pulse is used to etch the silicon at the bottom of the pattern that has been uncovered. Since the sidewalls are still protected by the polymer layer, the etching happens mainly in the vertical direction. This helps to create deep and narrow structures with smooth and straight sidewalls.

By repeating these steps many times, the Bosch process can create deep and narrow ridge structures with very smooth surfaces and precise shapes. To reach the desired 1.5 µm etch depth and 1 µm waveguide width, the process parameters such as the time of each step, gas flow rates, plasma power, and the total number of cycles had to be carefully adjusted. This optimization helped keep the shape of the waveguides accurate and reduced any surface roughness or optical losses that could affect the performance of the devices.

To address the previously observed challenges in etching narrow 1 µm-wide waveguides, a new CAD layout containing five parallel waveguides with variable spacing was designed to facilitate process optimization. Several experimental tests were performed to systematically tune the deposition and etching parameters and achieve the desired anisotropy and surface smoothness.

The SEM images of the fabricated waveguides etched using the Bosch process are shown in Fig. 65. After process optimization, the final Bosch etching parameters were defined as four cycles with an etching phase duration of 1.4 s and an ICP power of 400 W applied during all phases, with the detailed phase parameters summarized in Table 11.

Table 11. Phase parameters of the Bosch process

Phase	**RF power(w)**	**Pressures (mTorr)**	**SF_6(sccm)**	**C_4F_8 (sccm)**	**etching time(s)**
Deposition	35	25	5	100	3
Break	35	30	100	5	2.5
Etching	35	30	100	5	1.4

As it can be seen in Fig .65.a and b the optimized Bosch process successfully produced smooth, vertical sidewalls and achieved the desired etch depth, enabling precise waveguide geometry suitable for high-quality optical performance in the fabricated MMI splitters and switches.

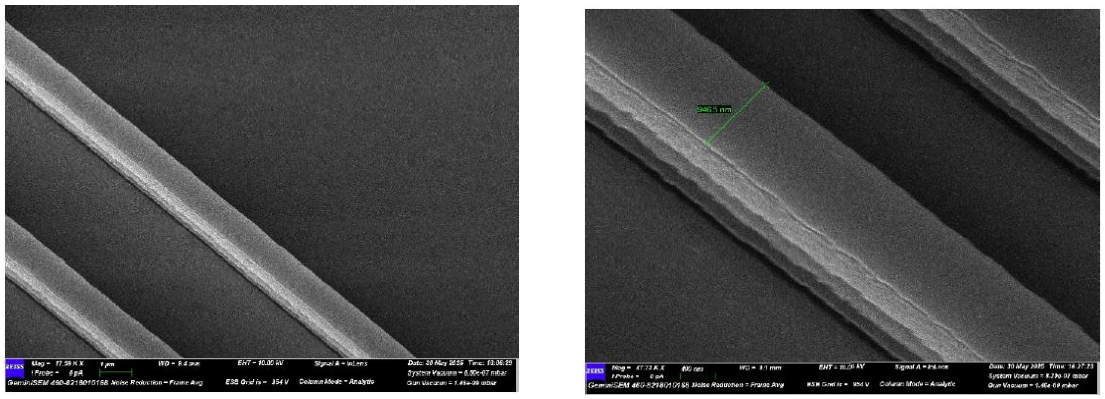

(a) (b)

Figure 65. SEM images of the silicon waveguides etched using the Bosch deep reactive ion etching (DRIE) process. (a) Overview of two adjacent waveguides showing well-defined and nearly vertical sidewalls obtained through the cyclic Bosch process. (b) A magnified view highlighting the characteristic scalloped sidewall morphology resulting from the alternating deposition and etching cycles inherent to the Bosch technique.

A comparison between the conventional ICP-RIE and the optimized Bosch process is shown in Fig. 66. In the optical image of the ICP-RIE etched waveguides (Fig. 66.a), the shapes are not very accurate and do not fully match the CAD design. The sidewalls look tilted instead of straight, and some shadow effects can be seen around the edges. In contrast, the Bosch-etched waveguides (Fig. 66.b) look much cleaner and closer to the original design. The sidewalls are straight and smooth, and no shadows are visible, showing that the Bosch process gives a better and more precise etching result.

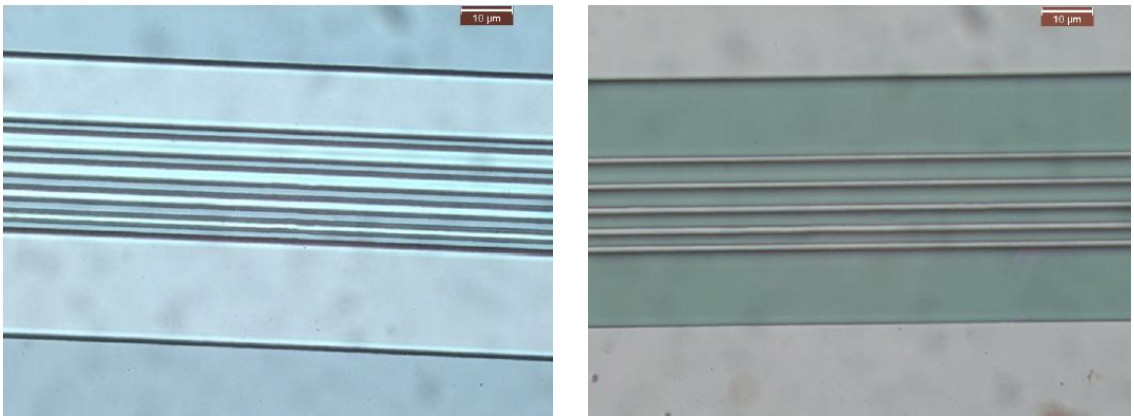

(a) (b)

Figure 66. Comparison between conventional ICP-RIE and the optimized Bosch process. Optical microscope images of the waveguides are shown in (a) and (b). The image highlights the excellent pattern transfer fidelity and structural accuracy achieved, closely reproducing the intended CAD design.

Finally, Fig. 67 shows the fabricated splitter device after completion of the etching process. The optical micrograph confirms that the final pattern was accurately transferred and closely matches the CAD design, demonstrating the effectiveness of the optimized Bosch etching process. Following successful fabrication, the device was transferred to the optical laboratory for the characterization stage, where a dedicated experimental setup was employed to evaluate its performance.

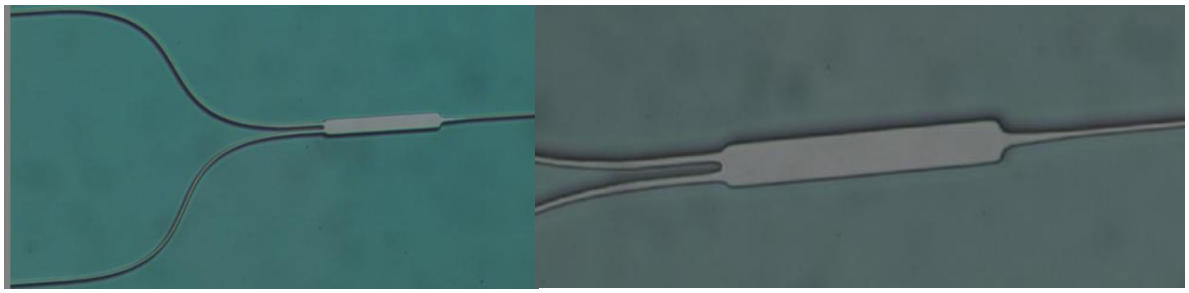

Figure 67. Optical microscope images of the fabricated MMI splitter produced using the optimized Bosch etching process. The images show smooth and well-defined waveguide boundaries, confirming the high quality of the fabrication. The device is fully fabricated and ready for optical characterization.

5.2.1.3 Optical characterization

To characterize the fabricated MMI passive splitter, the experimental setup shown in Fig. 68 was employed. This setup was designed to measure the optical transmission at the two output ports over the wavelength range of 1.50–1.65 µm. The system includes a tunable laser source, two polarization-maintaining tapered fibers for coupling light into and out of the device, an InGaAs photodetector (Thorlabs DET10CFC), and a lock-in amplifier for accurate power measurement.

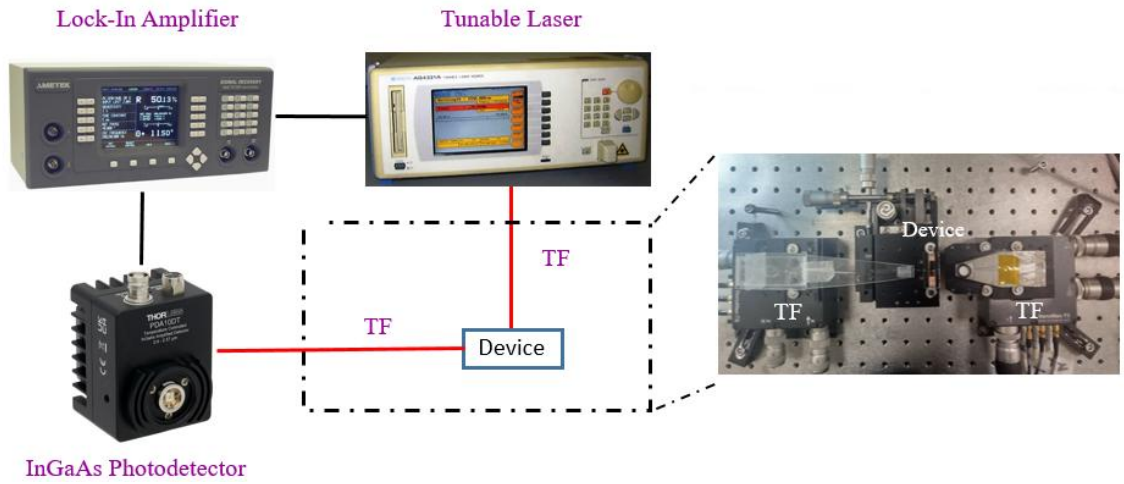

Figure 68. Experimental setup used for the characterization of the fabricated MMI passive splitter, including a tunable laser source, polarization-maintaining tapered fibers for input/output coupling, an InGaAs photodetector, and a lock-in amplifier for accurate optical transmission measurements.

Light from the tunable laser (ANDO AQ4321D) was modulated and coupled into the input waveguide

through a single mode tapered fiber (TF). The transmitted signal at the output was collected using another single mode tapered fiber and converted to an electrical signal by the calibrated InGaAs photodetector. Single mode tapered fibers were chosen instead of multimode fibers (MF) to ensure higher coupling efficiency and perfectly localized collection. The electrical output of the photodetector was then measured using a lock-in amplifier (Signal Recovery 7280 DSP), which suppresses noise and enhances measurement sensitivity, enabling precise extraction of the transmitted optical power.

The measurement results of the fabricated MMI splitter are presented in Fig. 69, where the optical output power from the two output ports was recorded using an oscilloscope. The collected data were then processed using custom MATLAB scripts to precisely analyze the transmission characteristics of the device.

As shown in Fig. 69.a, the output power was measured across a wavelength range from 1.5 µm to 1.65 µm. The average insertion loss within this range was approximately 0.57 dB for Output Port 1 and 1.3 dB for Output Port 2, indicating good overall device performance and efficient optical splitting.

Figure. 69.b shows the power imbalance between the two output ports as a function of wavelength, which varies between 0.6 dB and 0.96 dB. By comparing the simulation results of the MMI splitter in section" 4.2.1 MMI passive splitter" with the experimental characterization data, a fairly good agreement can be observed. While the simulated structure shows perfectly balanced transmission between the two output ports, the fabricated device exhibits a small difference in output power. This small difference can result from several practical factors commonly encountered during fabrication and measurement steps including fabrication tolerances, non-uniform etch depth, material absorption, lithography misalignment, surface contamination, and coupling misalignments during optical testing. Such imperfections can slightly change propagation of light within the device, resulting optical loss and power imbalanced between the two outputs.

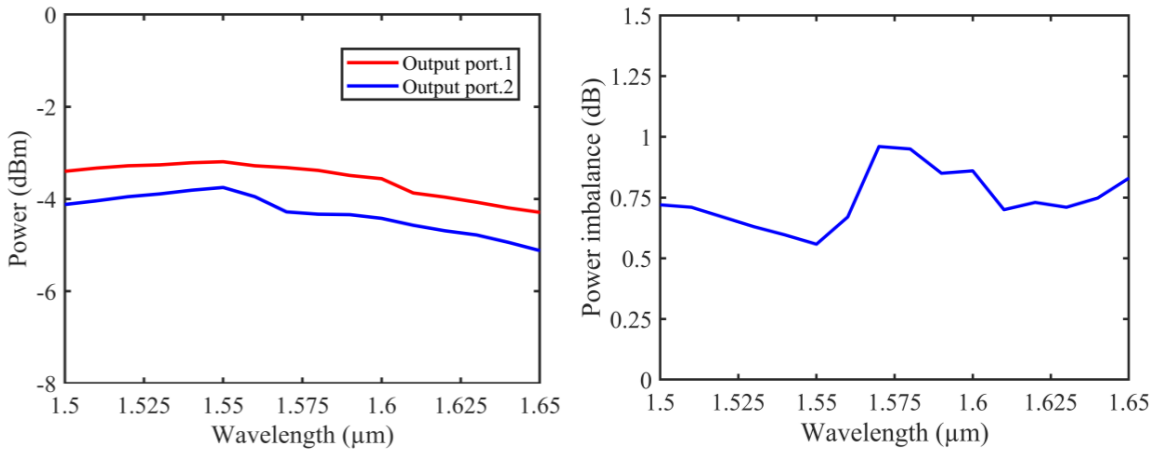

(a) (b)

Figure 69. (a) Optical power as a function of wavelength for the two output ports of the 1×2 MMI splitter. (b) Power imbalance between the two output ports as a function of wavelength. The results indicate uniform power distribution and low imbalance across the wavelength range of 1.5–1.65 µm, confirming broadband performance of the splitter.

5.2.2. MMI Mach–Zehnder interferometer switch

For the next phase of the project, a thermo-optic MMI switch was designed for fabrication, building upon the previously developed 1×2 MMI splitter. This new design extends the splitter architecture by integrating metal contact heaters and an additional 2×2 MMI section, thereby forming a complete MMI-based Mach–Zehnder thermo-optic switch. The design parameters were selected based on the simulation results discussed in Table 4 and Section“4.2.2 Active Mach-Zehnder thermo-optic switch with MMI structure.”

Figure. 70.a shows the CAD layout of the complete switch, designed in KLayout. The full layout comprises two MMI structures and the interferometer waveguide arms connecting them. The fabrication process follows the same procedure used for the 1×2 MMI splitter, including photolithography, etching, and pattern transfer steps. In the subsequent fabrication stage, metal contacts will be deposited to form micro-heaters, enabling the thermo-optic effect for active control of light propagation and switching between the output ports.

Figure. 70.b shows a microscope image of the fully fabricated MMI thermo-optic switch after the first round of fabrication, which included the waveguide and MMI pattern definition. The fabricated structure matches closely with the CAD layout, confirming a successful pattern transfer. In the next step, the second round of fabrication will be carried out to form the metal contacts for the heaters.

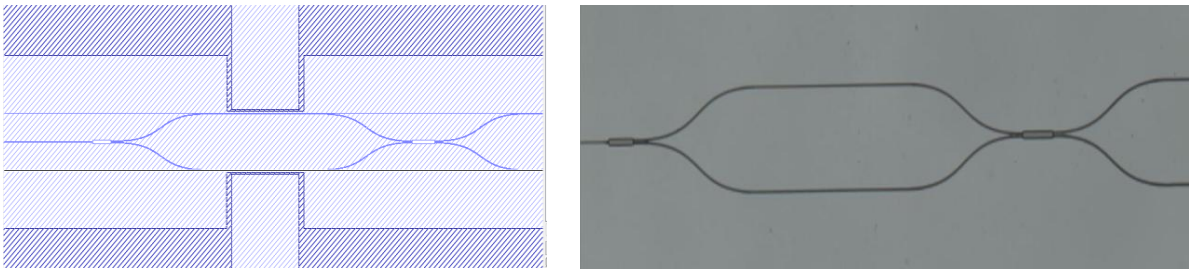

(a) (b)

Figure 70. (a) CAD layout of the MMI-based Mach–Zehnder switch designed in KLayout software. (b) Optical microscope image of the fabricated switch after the first round of photolithography, showing successful pattern transfer of the MMI and waveguide structures.

5.2.2.1 Heater Fabrication and Metallization

In the second round of fabrication, a new photolithography step was done to create the metal heaters. These heaters are used to warm up specific parts of the device and control the light inside the Mach–Zehnder interferometer (MZI) by using the thermo-optic effect. The heaters were placed close to the silicon waveguides so that the heat could transfer efficiently, but still far enough to prevent the metal from absorbing light and causing optical losses.

Each heater was connected to large metal pads that serve as electrical contacts. These pads were placed a few hundred micrometres away from the active area to ease the contacting procedure that will follow. The metal lines connecting the heaters to the pads were made wide enough to reduce electrical resistance and power loss.

For the metal layer, a thin film of nickel (about 10 nm thick) was deposited using the thermal evaporation method. Nickel was chosen because it has a relatively high resistance, which helps to generate enough heat even with small electrical currents.

After the metal deposition, a lift-off process was done to remove the extra metal and leave only the desired pattern. The samples were placed in acetone heated to 50 °C for 5 minutes, which cleaned the unwanted metal and revealed the final shape of the heaters and contact pads. The result was a smooth and well-defined heater structure, as shown in Fig. 71, ready to be used for thermo-optic switching experiments.

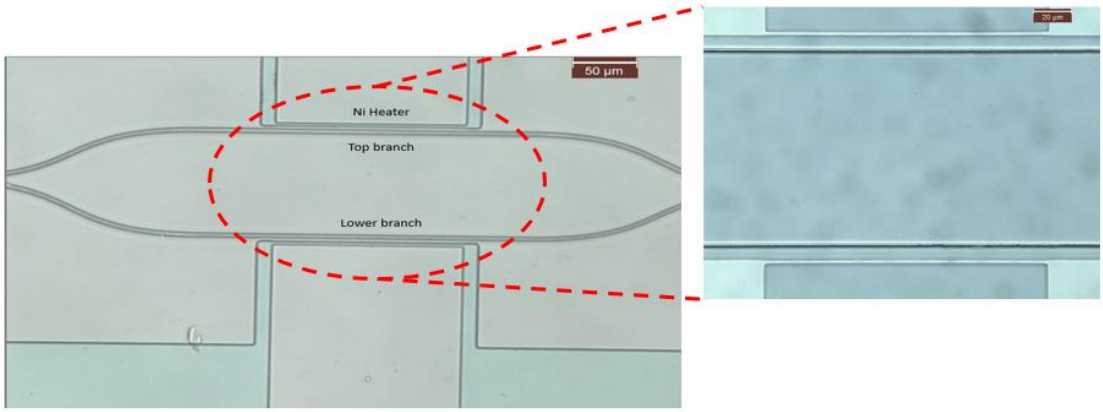

Figure 71. Optical microscope images of the nickel (Ni) heaters integrated into the MMI-based Mach–Zehnder thermo-optic switch.

An optical image of the device at the end of the fabrication process in the cleanroom is shown in Fig. 72.

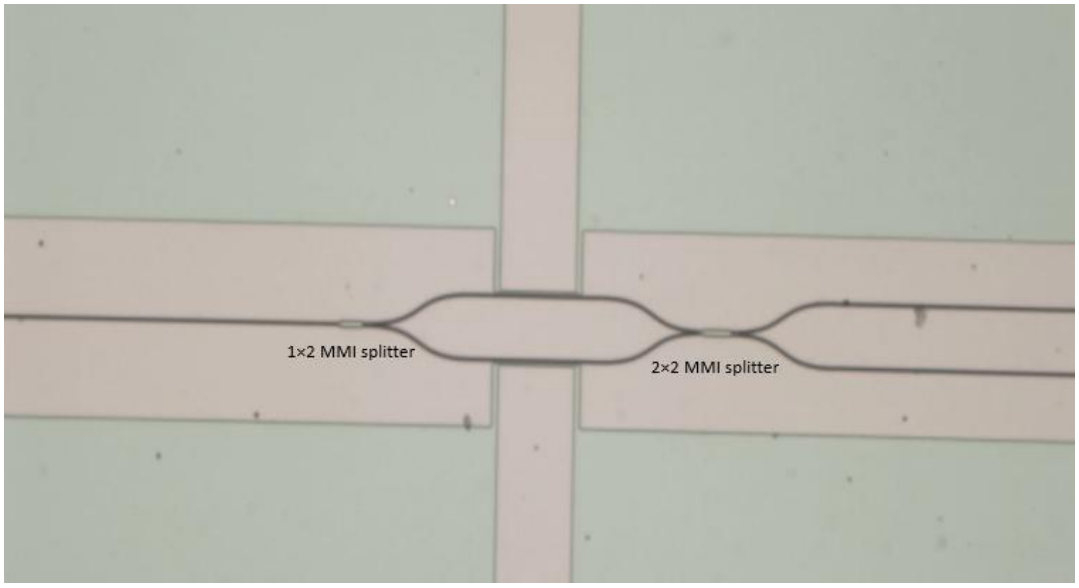

Figure 72. Optical microscope image of the fully fabricated MMI-based Mach–Zehnder thermo-optic switch, illustrating the completed device structure with integrated waveguides, MMI regions, and heater contacts.

5.2.2.2 Resistivity measurement of thin film nickel using four-point measurement.

To determine the resistivity of the deposited 10 nm nickel layer, a four-point probe measurement was performed. [102] This technique provides an accurate resistance measurement for thin films because it separates the current injection and voltage sensing paths, eliminating errors caused by contact resistance. In this method, four aligned probes are placed on the sample surface: the two outer probes inject a known current, while the two inner probes measure the resulting voltage drop. A linear V–I curve is obtained by sweeping the current and recording the voltage, and from its slope the sheet resistance R_s=V/I is extracted. Knowing the film thickness t, the resistivity of the nickel layer is then calculated using $\rho=R_s t$.

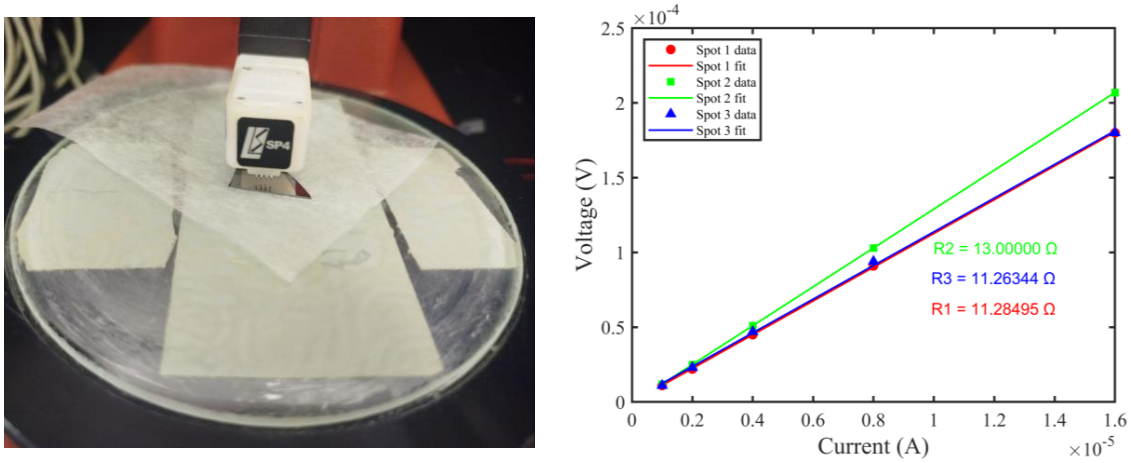

(a) (b)

Figure 73. (a) Four-point probe measurement setup used to characterize the thin-film nickel (Ni) layer deposited on the substrate. (b) Current–voltage (I–V) characteristics of the Ni thin film measured at three different spots, showing linear behavior consistent with ohmic conduction. The extracted resistances for the three locations are R_1 = 11.284 Ω, R_2 = 13.00 Ω, and R_3 = 11.26 Ω, confirming uniform film quality across the surface.

As shown in Fig. 73.a, the four-point probe measurements were performed at three different locations on the nickel thin film to check that the thickness and surface quality were uniform across the sample. The measured voltage–current (V–I) curve, shown in Fig. 73.b, was linear, which confirms that the nickel film behaves as a good Ohmic conductor. The measured resistance values at each point are also listed in the figure.

For a thin film measured with a four-point probe where all probe spacing are equal, the sheet resistance R_s can be calculated directly from the measured voltage and current. Because the current spreads out in the film in a circular manner, a geometric correction factor is needed. This factor comes from the mathematical solution of the current flow in a two-dimensional sheet. For equal probe spacing, the sheet resistance is given by:

$$R_s = \frac{\pi}{\ln 2}\frac{V}{I} \approx 4.53236\frac{V}{I}[\Omega/s] \quad (5.1)$$

$$\rho = R_s t \quad (5.2)$$

The factor $\pi/\ln(2) \approx 4.5326$ is not an experimental value; it comes directly from the geometry of four equally spaced probes and from the way voltage spreads in a thin film, which follows a logarithmic behavior. This relationship was first derived by Smits in 1958, who established the theoretical basis for the four-point probe method used today to measure sheet resistance. [102]

The average resistivity obtained from the measurements is 53×10^{-6} Ω·cm which in a good agreement with reported values for thin nickel films, typically ranging between 15×10^{-6} Ω·cm and 30×10^{-6} Ω·cm, confirming the good quality and uniformity of the deposited layer.

5.2.2.3 Device Mounting and Electrical Interfacing

After fabrication, the switches were mounted on custom 3D-printed mechanical holders designed to keep the devices stable and provide an easy way to connect them electrically. Metallic wires were carefully soldered to the electrode pads to create strong and reliable electrical connections, as shown in Fig. 74. This setup helped prevent unwanted electrical resistance, which could affect the accuracy of the thermo-optic tuning and the measurement results during testing.

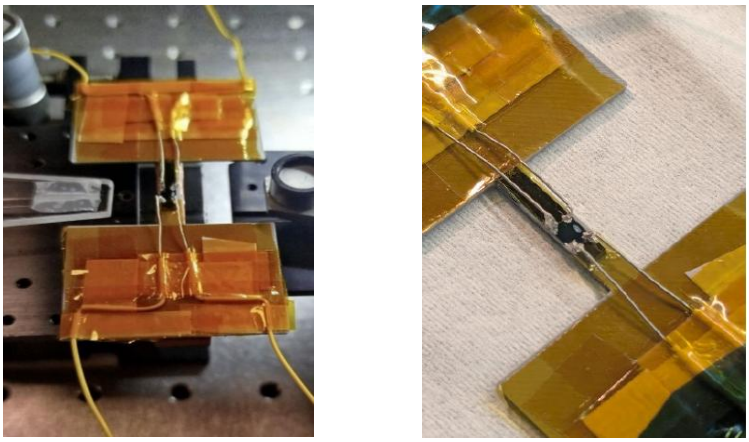

Figure 74. Fabricated optical switches mounted on custom 3D-printed mechanical supports. It shows the mounted devices with metallic wires soldered to the electrode pads, providing mechanical stability and ensuring reliable electrical connections for thermo-optic operation.

5.2.1.4 Optical characterization

The optical characterization of the fabricated switches was carried out using the experimental setup shown in Fig. 75. This setup was designed to measure the transmission response of the devices under different wavelengths and applied voltages. The system consisted of a tunable laser source, polarization-maintaining tapered fibers for coupling light in and out of the chip, an InGaAs photodetector (Thorlabs DET10CFC), a source-measurement unit for applying bias to the heater electrode, and a lock-in amplifier for accurate low-power signal detection.

Light from the tunable laser (ANDO AQ4321D), operating from 1500 to 1650 nm, was launched into the input waveguide of the device through a tapered fiber. The output fiber was aligned to one of the output ports of the switch, and the collected optical power was converted into an electrical signal by

the photodetector. Because the coupling efficiency between the tapered fiber and the on-chip waveguides was relatively low, the transmitted power levels were small. For this reason, a lock-in amplifier (Signal Recovery 7280 DSP) was used to extract the signal from the background noise and ensure precise measurements of the transmission.

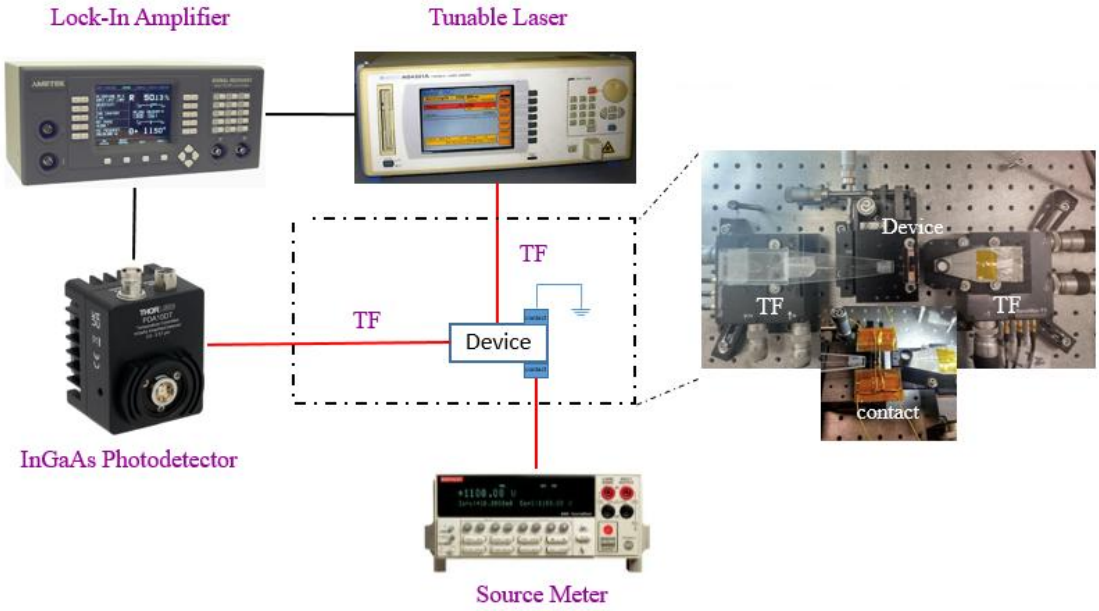

Figure 75. Experimental setup used for the optical characterization of the fabricated switches, including a tunable laser source, polarization-maintaining tapered fibers for chip coupling, an InGaAs photodetector, a source meter for heater biasing, and a lock-in amplifier for low-power transmission measurements under varying wavelength and applied voltage.

The heater electrodes of the device were connected to a source-measurement unit (Keithley 2410), which supplied the required voltage to induce the thermo-optic phase shift in one of the Mach–Zehnder arms. By adjusting the applied voltage, the refractive index of the heated arm was modified, leading to controlled switching between the output ports. All instruments, including the tunable laser, source meter, and lock-in amplifier, were controlled and monitored via GPIB, and a MATLAB script was used to automate data acquisition and analyze the transmission characteristics.

Figure. 76.a shows the measured optical power at one of the output ports (P_1) as a function of wavelength, ranging from 1535 nm to 1610 nm, for five different applied voltages. As shown in the figure, the device exhibits its optimal switching performance around 1550 nm, the wavelength at which the switch was originally designed and optimized.

Figure. 76.b presents the voltage-dependent modulation behavior of the switch in more detail. It shows the measured optical power at output port P_1 as a function of the applied voltage at a wavelength of 1.55 µm. As the voltage increases from 0 to 10 V, corresponding to an electrical power of approximately 30 mW, the transmitted optical power decreases from 630 pW to about 210 pW, roughly one-third of the initial value. This response, nearly linear within this voltage range,

demonstrates the thermo-optic phase modulation effect in the Mach–Zehnder interferometer and confirms a correct device operation, achieving the desired extinction ratio at the target wavelength.

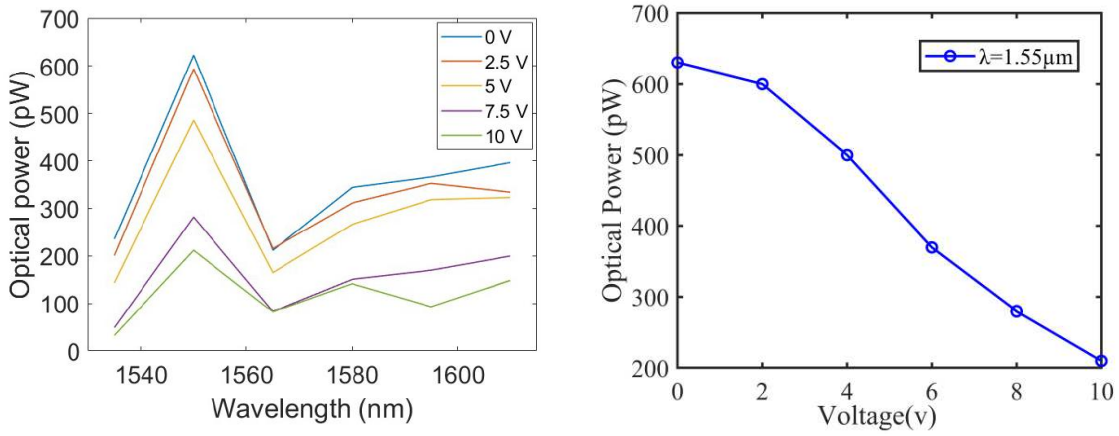

(a) (b)

Figure 76. (a) Measured optical power transmitted through the MMI-based Mach–Zehnder thermo-optic switch as a function of wavelength for different applied voltages on the heater electrodes. (b) Optical power at 1.55 μm as a function of applied voltage, a gradual decrease in transmitted power with increasing voltage due to the thermo-optic phase shift induced in one arm of the interferometer is shown.

Using the following formula, the phase shift between the two arms of the switch corresponding to each applied voltage can be calculated [81]. The results are shown in Fig. 77.a.

$$P_1(V) = \frac{P_{in}}{2}[1 + cos\,\Delta\phi(V)] \quad (5.3)$$

$$\Delta\phi(V) = arccos\left[2\frac{P_1(V)}{P_1(V=0)} - 1\right] \quad (5.4)$$

By also considering the wavelength of λ=1.55 μm and length of L=250 μm it is possible to find the relation between effective index changes and voltage as it shows in Fig. 77.b.

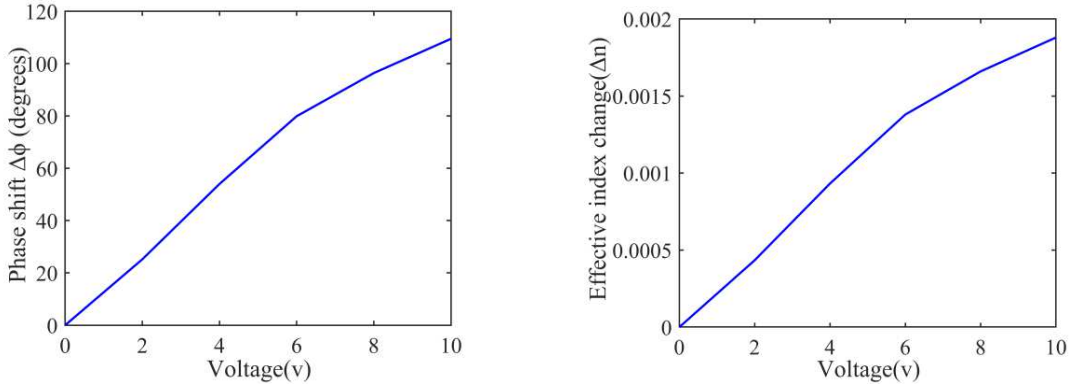

(a) (b)

Figure 77.(a) Phase shift (Δφ) between the two arms of the MMI-based Mach–Zehnder thermo-optic switch as a function of the applied voltage. (b) Variation of the effective refractive index (Δn) with respect to the applied voltage.

As shown in Fig. 78, the device temperature increases with the applied voltage, derived from the extracted phase shift and the associated change in effective refractive index. As observed, applying a voltage of 10 V results in a temperature increase of approximately 10.1 K, which is close to the 8.3 K temperature change predicted by the thermal simulation of the Mach–Zehnder switch required to achieve a π/2 phase shift, as discussed in Section" 4.2.2.1 Thermal simulation". This close agreement confirms the consistency between the experimental results and the simulation predictions.

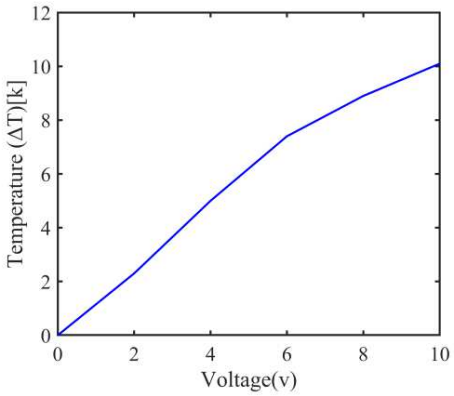

Figure 78. Calculated temperature rise (ΔT) as a function of the applied voltage, derived from the extracted phase shift and effective index change.

5.2.3. Asymmetric MMI Mach–Zehnder interferometer switch

After the fabrication of the symmetric MMI-based Mach–Zehnder switch, the next step was to fabricate the asymmetric version of the device, previously studied in Section 4.2.3 ("Asymmetric Mach–Zehnder Interferometer with MMI Structure").

To realize this design, the CAD layout was first developed using KLayout software. The layout consists of two MMI structures placed at the input and output of the interferometer. The 1×2 MMI splitter was designed with a length of 40 µm, while the 2×2 MMI coupler has a length of 50 µm. Both MMI sections have a width of 6 µm. The connecting waveguides have a width of 1.2 µm. In addition, a tapered waveguide was introduced at the input of the 1×2 MMI splitter, with the width gradually increasing from 1.2 µm to 2 µm to improve mode matching and coupling efficiency.

Unlike the symmetric configuration, the asymmetric design introduces a deliberate length difference between the two optical arms. This length mismatch creates a built-in phase difference between the propagating optical signals, making the device inherently wavelength-dependent. As a result, the interference at the output becomes sensitive to both wavelength and applied thermal tuning, enabling enhanced control of the switching behavior.

In this work, three different arm-length differences were implemented: 50 µm, 60 µm, and 70 µm. These values were selected to investigate the impact of asymmetry on the spectral response and switching performance of the device. Figures. 79.a, 79.b, and 79.c show the corresponding CAD layouts of the three asymmetric switch configurations.

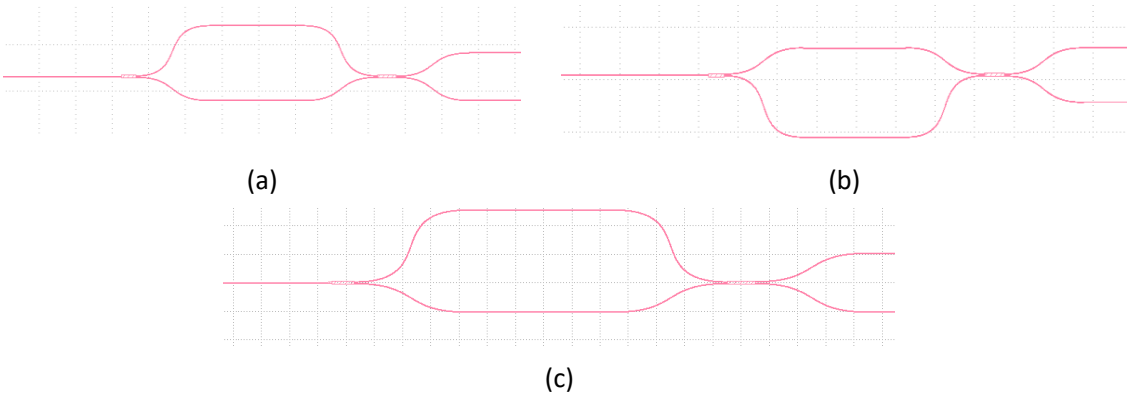

Figure 79. CAD layout of the asymmetric MMI switch with 1.2 µm-wide input and output waveguides, designed in KLayout software for different arm-length differences: (a) 50 µm, (b) 60 µm, and (c) 70 µm.

For the fabrication of the asymmetric MMI Mach–Zehnder switches, the same process flow described in the previous sections was employed. The devices were fabricated on a silicon-on-insulator (SOI) wafer using standard cleanroom techniques, including photolithography and dry etching. The process began with wafer cleaning to remove contaminants, followed by the application of an adhesion promoter (HMDS) and spin-coating of a positive photoresist layer.

The device patterns, including the MMI regions, input and output waveguides, and asymmetric interferometer arms, were defined using a direct-write laser lithography system. The exposure parameters were carefully optimized to ensure accurate pattern transfer, particularly for the 1.2 µm-wide waveguides used in this design. After exposure, the samples were developed to reveal the patterned photoresist, which was then used as a mask for the subsequent etching process.

The pattern was then transferred into the silicon device layer using dry etching. As discussed in earlier sections, optimized etching conditions were employed to achieve well-defined waveguide structures with smooth and nearly vertical sidewalls, which are essential for minimizing optical losses. Following the etching step, the remaining photoresist was removed, and the samples were cleaned to complete the fabrication process. The silicon device layer thickness was measured by profilometer to be in the range of 1.5 to 1.6 µm.

The final fabricated devices exhibit good agreement with the designed geometry, confirming the reliability of the fabrication process. Optical microscope images of the fabricated asymmetric switches are shown in Fig. 80. Figures. 80.a, 80.b, and 80.c correspond to devices with arm length differences of 50 µm, 60 µm, and 70 µm, respectively, in the Mach–Zehnder interferometers.

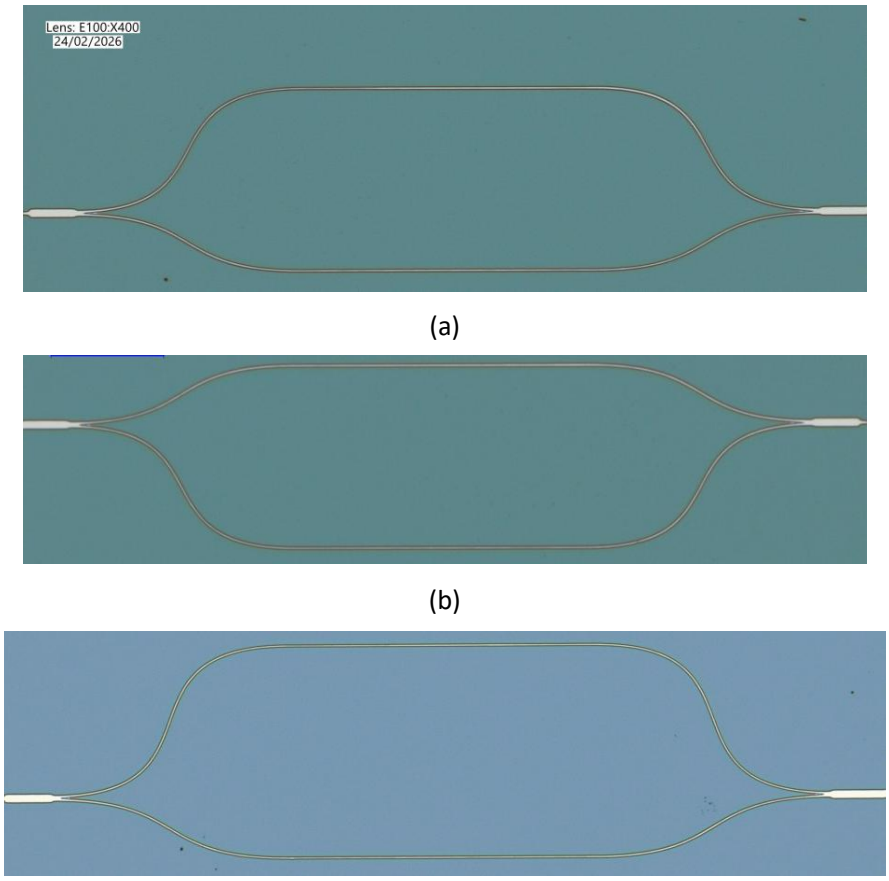

(a)

(b)

(c)

Figure 80. Optical microscope image of the fully fabricated MMI-based asymmetric Mach–Zehnder switch for different arm-length differences: (a) 50 µm, (b) 60 µm, and (c) 70 µm.

From Fig. 81, which shows the scanning electron microscope (SEM) image of the fabricated asymmetric switch, it can be observed that the device exhibits well-defined waveguide structures that closely follow the intended CAD geometry. The waveguide width appears consistent along the propagation direction, indicating good control during the photolithography and pattern transfer steps. The sidewalls of the waveguides are relatively vertical and smooth, confirming the effectiveness of the optimized dry etching process, particularly the use of the Bosch technique. Although slight surface roughness and scalloping are visible along the sidewalls, which are typical features of the Bosch process, they are not expected to significantly degrade the optical performance.

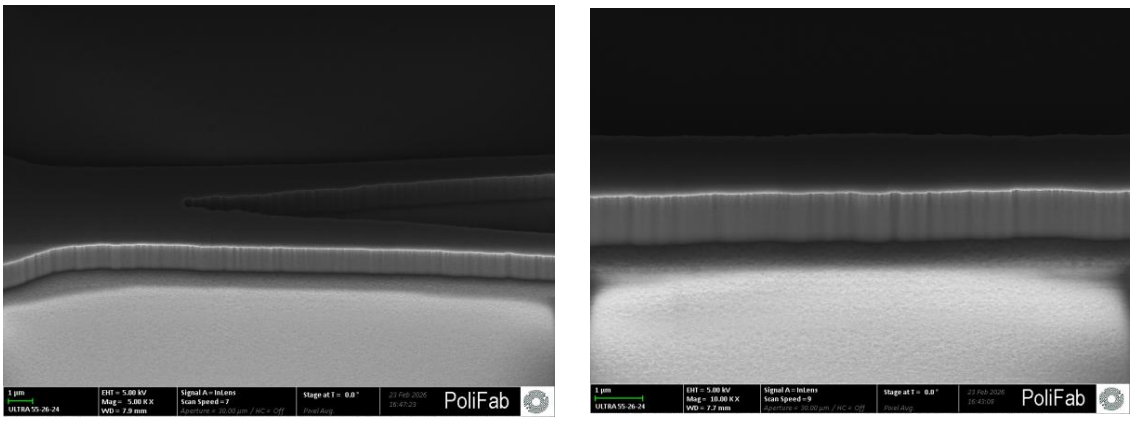

Figure 81. SEM images of the silicon waveguides etched using the Bosch deep reactive ion etching (DRIE) process. The analysis shows that the fabricated waveguides exhibit high structural quality, which is essential for achieving low optical losses and reliable interference behavior in the Mach–Zehnder interferometer.

For the characterization of the fabricated asymmetric MMI Mach–Zehnder switches, an optical measurement setup similar to the one described previously was used, with a key modification. In this case, the output optical signal was directly connected to an Ando (Yokogawa) Optical Spectrum Analyzer (OSA, AQ6317C), enabling direct measurement of the spectral response without the use of a photodetector.

A tunable laser source was used to generate the input signal, which was coupled into the device through a tapered fiber (TF) to ensure efficient coupling with the input waveguide. The transmitted signals from the two output ports were collected using single-mode fibers (SF) and routed to the optical spectrum analyzer. The laser source and the OSA were operated together to perform wavelength-dependent measurements over the desired spectral range.

During the characterization, the input wavelength was swept from 1520 nm to 1620 nm, allowing the observation of the interference effects caused by the intentional length difference between the two arms of the asymmetric Mach–Zehnder interferometer. This resulted in a wavelength-dependent transmission response at the output ports.

The measured spectra were recorded and transferred to a PC, where MATLAB was used for data processing and visualization. This enabled a clear analysis of the interference patterns and switching behavior of the device. The complete configuration of the measurement setup is shown in Fig. 82.

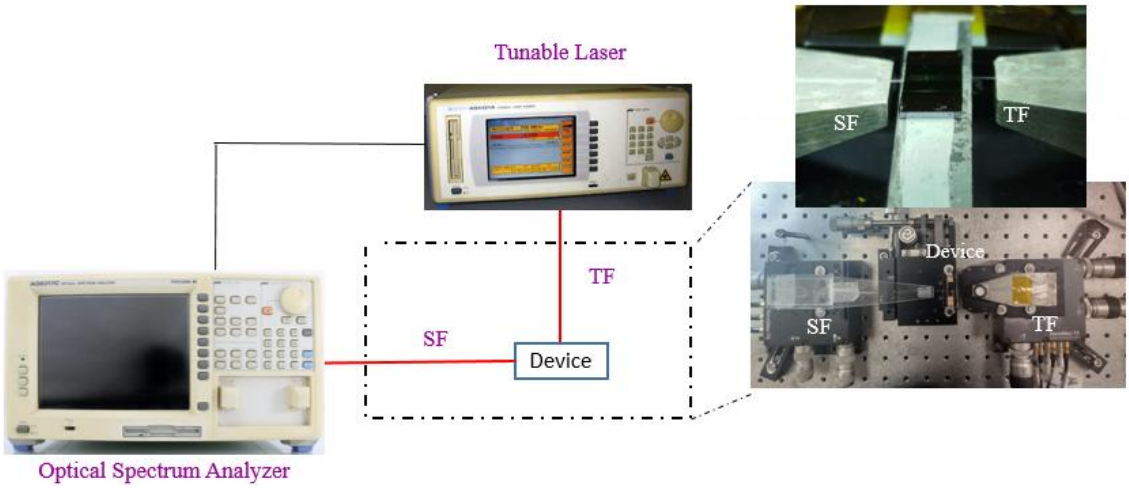

Figure 82. Experimental setup used for the optical characterization of the fabricated switches, including a tunable laser source, polarization-maintaining tapered fibers for chip coupling, a single-mode fiber at the output for light collection, and an optical spectrum analyzer for analyzing the optical signal.

Figure. 83 presents a comparison between the simulated and experimentally characterized transmission spectra of the fabricated asymmetric MMI-based Mach–Zehnder switches for arm-length differences of 70 µm and 60 µm. As shown in Fig. 83.b and Fig. 83.d, the simulation results exhibit a periodic and complementary response between the two output ports, with a spectral period of approximately 10 nm for ΔL = 70 µm and 12 nm for ΔL = 60 µm. This behavior is expected, as the interference pattern in an asymmetric Mach–Zehnder interferometer is directly determined by the optical path length difference between the two arms. This periodic spacing corresponds to the free spectral range (FSR) of the device, which is inversely proportional to the arm-length difference, explaining the smaller FSR observed for the larger ΔL.

The experimental results, shown in Fig. 83.a and Fig. 83.c, follow the same periodic trend, with measured peak spacings of approximately 10–11 nm for the 70 µm device and around 12 nm for the 60 µm device. The good agreement between the simulated and measured spectral periods confirms that the fabricated devices accurately reproduce the designed asymmetry and optical behavior. Although minor variations in peak amplitude and spectral shape are observed, these differences can be attributed to practical factors such as fabrication tolerances, sidewall roughness, and coupling losses during measurement.

Overall, the close match between simulation and experimental results demonstrates the reliability of the design and fabrication process, confirming that the asymmetric MMI Mach–Zehnder switches operate as expected and exhibit predictable wavelength-dependent switching behavior.

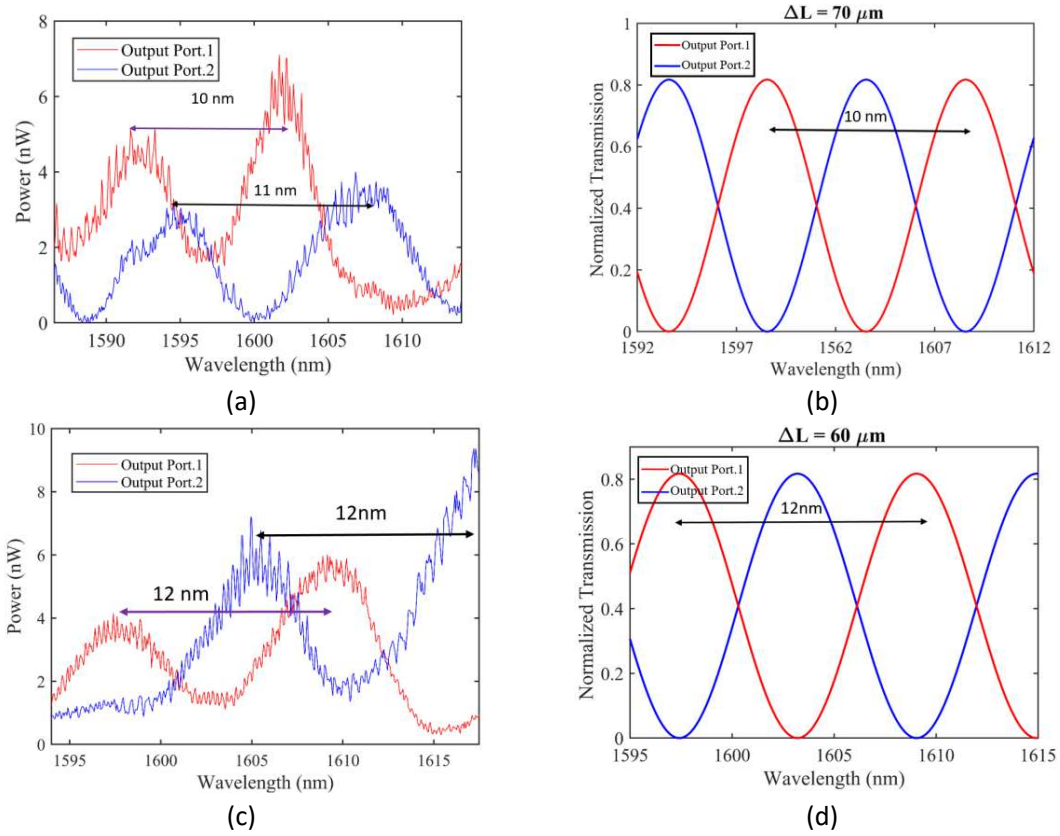

Figure 83. Comparison between experimental and simulated transmission spectra of asymmetric MMI-based Mach–Zehnder switches for two arm-length differences. (a) Measured output power for ΔL = 70 µm, (b) corresponding simulated normalized transmission, (c) measured output power for ΔL = 60 µm, and (d) corresponding simulated normalized transmission. The spectral spacing between consecutive peaks is approximately 10–11 nm for ΔL = 70 µm and 12 nm for ΔL = 60 µm, showing good agreement between experimental results and simulations.

5.2.4. Conclusion

In this section, the fabrication and experimental characterization of MMI-based Mach–Zehnder interferometer switches were successfully demonstrated, including both symmetric thermo-optic and asymmetric configurations. The devices, fabricated on SOI wafers using laser-writer photolithography and an optimized Bosch DRIE process, exhibited high structural quality and reliable optical performance. The passive MMI splitter showed broadband operation with low insertion loss and good agreement with simulations. The symmetric thermo-optic switch enabled efficient and controllable phase modulation around 1.55 µm, with results consistent with thermal and optical predictions. In addition, the asymmetric structures exhibited a wavelength-dependent periodic response, with measured spectra closely matching simulations, confirming accurate implementation of the designed arm-length differences. Overall, the results validate the robustness, flexibility, and suitability of MMI-based Mach–Zehnder architectures for integrated silicon photonic switching applications.

6. Conclusions and Future Perspectives

6.1 Conclusions

This thesis has investigated the design, simulation, fabrication, and experimental validation of silicon-based photonic integrated switches for telecommunication applications, with particular emphasis on thermo-optic and graphene-enabled electro-optic devices. The work was carried out in the context of the GrapHICS project, aiming at the development of compact, broadband, and energy-efficient optical switching solutions compatible with standard silicon photonics technology.

A comprehensive study of different switching architectures was first conducted, including Mach–Zehnder interferometers, ring resonators, multimode interference (MMI) structures, and adiabatic devices. Through systematic numerical analysis and comparison, two main architectures were identified as the most promising candidates: the adiabatic thermo-optic switch and the MMI-based Mach–Zehnder thermo-optic switch. These designs were selected due to their broadband operation, robustness to fabrication tolerances, and compatibility with large-scale integration.

A major original contribution of this thesis is the proposal and detailed investigation of an adiabatic thermo-optic switch based on tapered waveguide transitions. The adiabatic switch structure enables smooth mode evolution, low insertion loss, and reduced sensitivity to wavelength and polarization. Simulations demonstrated efficient switching operation for both TE and TM polarizations across the C- and L-bands, with low power consumption and high extinction ratio. The extracted performance parameters were successfully used to design and simulate scalable 2×2 and 4×4 switching matrices using an S-parameter-based system-level approach, confirming the suitability of this architecture for reconfigurable optical networks such as FTTH systems.

In parallel, an MMI-based Mach–Zehnder thermo-optic switch was designed, fabricated, and experimentally characterized. The fabrication process was developed and optimized in a cleanroom environment, addressing key challenges related to photolithography and silicon etching. The adoption of the Bosch deep reactive ion etching process enabled the realization of high-quality waveguides with vertical sidewalls and good dimensional control. Optical measurements confirmed the correct operation of the fabricated devices, showing good agreement with simulation results in terms of insertion loss, extinction ratio, and wavelength response.

From a scalability point of view, the insertion loss increases as the size of the switching matrix grows due to the accumulation of losses from multiple cascaded elements. Based on the results obtained in this work, a single adiabatic switch shows an insertion loss of approximately 0.37–0.52 dB, while the 2×2 matrix exhibits values around 0.7 dB for TE mode and 0.91 dB for TM mode. When extending the design to a 4×4 matrix, the insertion loss increases to about 1.55–1.8 dB in the forward direction and can reach up to 3.6 dB in the worst-case paths. This behavior is expected since the optical signal passes through a higher number of switching elements as the matrix size increases. In addition, each stage includes components such as MMI couplers and interferometric sections with insertion losses on the order of 0.4–0.65 dB, which further contributes to the total loss. These results confirm that, although the proposed structures exhibit low insertion loss at small scale, optimization of individual components is important to maintain acceptable performance in larger switching matrices.

In addition to thermo-optic switching, this thesis explored graphene-based electro-optic devices, including a graphene–insulator–graphene capacitor and a graphene-assisted electro-absorption modulator. By embedding graphene at positions of high optical field overlap and employing hydrogenated amorphous silicon as an additional guiding layer, enhanced modulation efficiency and high-speed operation were achieved in simulation. This part of the work highlights the potential of integrating two-dimensional materials with silicon photonics to overcome the intrinsic speed limitations of thermo-optic devices.

Overall, the results presented in this thesis demonstrate that adiabatic and MMI-based switching architectures implemented on silicon platforms offer an effective balance between performance, scalability, and fabrication robustness. The combination of detailed physical modeling, careful design optimization, and experimental validation provides a solid foundation for the development of next-generation photonic integrated switches.

6.2 Future Perspectives

Several promising research directions emerge from this work.

A first immediate step is the experimental characterization of the fabricated adiabatic thermo-optic switch, which was designed and submitted for fabrication but not fully tested within the timeframe of this thesis. Detailed optical and thermal measurements will allow direct validation of the predicted broadband performance, polarization tolerance, switching efficiency, and power consumption.

A natural extension of this work is the fabrication and experimental demonstration of a complete N×N adiabatic switching matrix, such as the 2×2 and 4×4 architectures investigated through interconnect simulations. Realizing such matrices would represent a key milestone toward practical deployment in telecommunication systems, particularly for remotely reconfigurable passive optical networks and fiber-to-the-home (FTTH) infrastructures.

Another important future direction is the integration of graphene-based electro-optic functionality within adiabatic switch architectures. By combining the broadband and fabrication-tolerant properties of adiabatic waveguides with the electrically tunable optical properties of graphene, a new class of hybrid adiabatic electro-optic switches could be developed. Embedding graphene layers at positions of high optical field overlap within the adiabatic region would enable fast, low-power electro-optic control, potentially replacing or complementing thermo-optic actuation. This hybrid approach could significantly improve switching speed and energy efficiency while preserving the robustness and broadband response of adiabatic devices.

Further perspectives include the experimental realization of graphene-based ring switches and electro-absorption modulators, allowing direct comparison with thermo-optic devices in terms of speed, footprint, and power consumption. Hybrid switching schemes that combine thermo-optic tuning for coarse reconfiguration and electro-optic tuning for fast operation also represent a promising avenue.

Finally, continued optimization of materials, heater designs, dielectric stacks, and waveguide geometries may further reduce power consumption and improve performance. The integration of these devices into larger photonic–electronic systems opens the way toward intelligent, reconfigurable, and fully integrated optical networks.

In conclusion, this thesis provides original device concepts, validated fabrication strategies, and scalable design methodologies that contribute to the advancement of silicon photonic switching technologies and pave the way for next-generation high-performance optical communication systems.

References

[1] L. Chen e Y.-k. Chen, «Compact, low-loss and low-power 8×8 broadband silicon optical switch,» *Optics express,* vol. 20, n. 17, pp. 18977-18985, 2012.

[2] W. Li e D. Huang , «Silicon Photonics Devices and Integrated Circuits,» *MDPI,* vol. 12, n. 3, p. 187, 2025.

[3] B. Jalali e S. Fathpour, «Silicon Photonics,» *Journal of lightwave technology,* vol. 24, n. 12, pp. 4600-4615, 2007.

[4] M. Lipson, «The revolution of silicon photonics,» *Nature Materials ,* vol. 21, n. 9, pp. 974-975, 2022.

[5] X. Chen, J. Lin e K. Wang, «A Review of Silicon-Based Integrated Optical Switches,» *Laser & Photonics Reviews,* vol. 17, n. 4, p. 2200571, 2023.

[6] Y. Singh e H. Subbaraman, «Recent advances in graphene-enabled silicon-based high-speed optoelectronic devices—a review,» *Photonics,* vol. 10, n. 12, p. 1292, 2023.

[7] M. Asghari e A. V. Krishnamoorthy, «Energy-efficient communication.,» *Nature photonics,* vol. 5, n. 5, pp. 268-270, 2011.

[8] J. Wang e Y. Long, «On-chip silicon photonic signaling and processing: a review.,» *Science Bulletin,* vol. 63, n. 19, pp. 1267-1310, 2018.

[9] R. Yu, S. Cheung, Y. Li, K. Okamoto, R. Proietti, Y. Yin e S. J. B. Yoo, «A scalable silicon photonic chip-scale optical switch for high performance computing systems.,» *Optics Express,* vol. 21, n. 26, pp. 32655-32667, 2013.

[10] T. Hirokawa, M. Saeidi, S. Pillai, A. Nguyen-Le, L. Theogarajan, A. A. M. Saleh e C. L. Schow, «A wavelength-selective multiwavelength ring-assisted Mach–Zehnder interferometer switch.,» *Journal of Lightwave Technology,* vol. 38, n. 22, pp. 6292-6298, 2020.

[11] S. J. B. Yoo, «Photonic switching technologies, architectures, and integrated-systems for future disaggregated and optically reconfigurable data centers.,» in *2022 International Conference on Optical Network Design and Modeling (ONDM). IEEE*, Warsaw, Poland, 2022.

[12] A. H. A. S. Moazeni, F. Pavanello, H. Gevorgyan, J. Notaros, L. Alloatti, M. T. Wade, C. Sun, S. A. Kruger, H. Meng, K. Al Qubaisi, I. Wang, B. Zhang, A. Khilo, C. V. Baiocco, M. A. Popović, V. M. Stojanović e R. J. Ram, «Integrating photonics with silicon nanoelectronics for the next generation of systems on a chip.,» *Nature,* vol. 556, n. 7701, pp. 349-354, 2018.

[13] P. P. Absil, P. Verheyen, P. De Heyn, M. Pantouvaki, G. Lepage, J. De Coster e J. Van Campenhout, «Silicon photonics integrated circuits: a manufacturing platform for high density, low power optical I/O's.,» *Optics express,* vol. 23, n. 7, pp. 9369-9378, 2015.

[14] S. Kumar, S. Kumar Raghuwanshi e A. Kumar, «Implementation of optical switches using Mach–Zehnder interferometer,» *Optical Engineering,* vol. 52, n. 9, pp. 097106-097106, 2013.

[15] Z. Guo, L. Lu, L. Zhou, L. Shen e J. Chen, «16 × 16 Silicon Optical Switch Based on Dual-Ring-Assisted Mach–Zehnder Interferometers,» *Journal of Lightwave Technology,* vol. 36, n. 2, pp. 225-232, 2017.

[16] S. Nagai, G. Morishima, H. Inayoshi e K. Utaka, «Multimode interference photonic switches (MIPS),» *Journal of Lightwave Technology,* vol. 20, n. 4, pp. 675-681, 2004.

[17] X. Jia, S. Luo e X. Cheng, «Design and optimization of novel ultra-compact SOI multimode

interference optical switch,» *Optics communications,* vol. 281, n. 5, pp. 1003-1007, 2008.

[18] B. Hashemi, M. Keihani e A. H. Alizadeh, «Design, simulation of XOR / XNOR and AND logic gates using the optical two-circle switch,» *Optics Continuum,* vol. 1, n. 2, pp. 399-408, 2022.

[19] J. Van Campenhout, W. M. J. Green, S. Assefa e Y. A. Vlasov, «Low-power, 2×2 silicon electro-optic switch with 110-nm bandwidth for broadband reconfigurable optical networks,» *Optics Express,* vol. 17, n. 26, pp. 24020-24029, 2009.

[20] M. R. Watts, J. Sun, C. DeRose, D. C. Trotter, R. W. Young e G. N. Nielson, «Adiabatic thermo-optic Mach–Zehnder switch,» *Optics letters,* vol. 38, n. 8, pp. 733-735, 2013.

[21] L. Song, L. Lyu, X. Jiao, C. Gao, W. Liu, H. Li, Y. Shi e D. Dai, «Low-Loss C+L+S-Band 2 × 2 Thermo-Optic Mach-Zehnder Switches with Compact Fast Quasi-Adiabatic Couplers,» *Journal of Lightwave Technology ,* pp. 1 - 7, 2024.

[22] M. G. Robinson, K. M. Johnson e D. Doroski, «Polarization-independent, broadband, bistable, 2 × 2 optical exchange switch,» *Optics Letters,* vol. 15, n. 2, pp. 145-147, 1990.

[23] X. Sun, J. Feng, L. Zhong, H. Lu, W. Han, F. Zhang, R. Akimoto e H. Zeng, «Silicon nitride based polarization-independent 4 × 4 optical matrix switch,» *Optics & Laser Technology,* vol. 119, p. 105641, 2019.

[24] H. Wang, J. Dai, H. Jia, S. Shao, X. Fu, L. Zhang e L. Yang, «Polarization-independent tunable optical filter with variable bandwidth based on silicon-on-insulator waveguides.,» *Nanophotonics,* vol. 7, n. 8, pp. 1469-1477, 2018.

[25] J. S. Wey, «The outlook for PON standardization: A tutorial,» *Journal of Lightwave Technology,* vol. 38, n. 1, pp. 31-42, 2019.

[26] C. Ozcan, M. Mojahedi e J. S. Aitchison, «Short, broadband, and polarization-insensitive adiabatic Y-junction power splitters,» *Optics Letters,* vol. 48, n. 18, pp. 4901-4904, 2023.

[27] G. Queraltó, V. Ahufinger e J. Mompart, «Integrated photonic devices based on adiabatic transitions between supersymmetric structures,» *Optics Express,* vol. 26, n. 26, pp. 33797-33806, 2018.

[28] Y. Fu, T. Ye, W. Tang e T. Chu, «Efficient adiabatic silicon-on-insulator waveguide taper,» *Photonics Research,* vol. 2, n. 3, pp. A41-A44, 2014.

[29] S. Khan, S. M. Buckley, J. Chiles, R. P. Mirin e S. W. Nam, «Low-loss, high-bandwidth fiber-to-chip coupling using capped adiabatic tapered fibers,» *APL Photonics ,* vol. 5, n. 5, 2020.

[30] C. Ozcan, S. Aitchison e M. Mojahedi, «Foundry-Processed Compact and Broadband Adiabatic Optical Power Splitters with Strong Fabrication Tolerance.,» *Photonics. Vol,* vol. 10, n. 12, p. 1310, 2023.

[31] W. K. Burns e A. F. Milton, «Mode conversion in planar-dielectric separating waveguides,» *IEEE Journal of Quantum Electronics,* vol. 11, n. 1, pp. 32-39, 1975.

[32] Y. Shani, C. Henry, R. Kistler, R. Kazarinov e K. Orlowsky, «Integrated optic adiabatic devices on silicon,» *IEEE Journal of quantum Electronics,* vol. 27, n. 3, pp. 556-566, 1991.

[33] Y. Wang, S. Gao, K. Wang e E. Skafidas, «Ultra-broadband and low-loss 3 dB optical power splitter based on adiabatic tapered silicon waveguides,» *Optics Letters,* vol. 41, n. 9, pp. 2053-2056, 2016.

[34] L. B. Soldano e E. C. Pennings, «Optical multi-mode interference devices based on self-imaging: principles and applications,» *Journal of lightwave technology,* vol. 13, n. 4, pp. 615-627, 2002.

[35] J. M. Heaton e R. M. Jenkins, «General matrix theory of self-imaging in multimode interference (MMI) couplers.,» *IEEE Photonics Technology Letters,* vol. 11, n. 2, pp. 212-214, 2002.

[36] D. Marcuse, Theory of dielectric optical waveguides, Elsevier, 2013.

[37] A. M. Al-Hetar, A. B. Mohammad, A. S. M. Supa'at e Z. A. Shamsan, «MMI-MZI Polymer Thermo-Optic Switch With a High Refractive Index Contrast,» *Journal of Lightwave Technology,* vol. 29, n. 2, pp. 171-178, 2010.

[38] S.-H. Kim, J.-B. You, H.-W. Rhee, D. E. Yoo, D.-W. Lee e K. Yu, «High-Performance Silicon MMI Switch Based on Thermo-Optic Control of Interference Modes,» *IEEE Photonics Technology Letters ,* vol. 30, n. 16, pp. 1427-1430, 2018.

[39] Krishnanunni R. A e S. Ravindran, «A Compact Silicon Based 1 × 2 MMI Switch Based on Carrier Injection Based Refractive Index Change,» *IEEE Photonics Journal,* 2025.

[40] D. R. Cooper, B. D'Anjou, N. Ghattamaneni, B. Harack, M. Hilke, A. Horth, N. Majlis, M. Massicotte, L. Vandsburger, E. Whiteway e V. Yu, «Experimental review of graphene.,» *International Scholarly Research Notices,* vol. 2012, n. 1, p. 501686, 2012.

[41] A. K. Geim e K. Novoselov, «The rise of graphene.,» *Nature materials,* vol. 6, n. 3, pp. 183-191, 2007.

[42] J. E. Proctor, D. Melendrez Armada e A. Vijayaraghavan, An Introduction to Graphene and Carbon Nanotubes, CRC Press, 2017.

[43] K. S. Novoselov, A. K. Geim, S. V. Morozov, D. Jiang, M. I. Katsnelson, I. V. Grigorieva, S. V. Dubonos e A. A. Firsov, «Two-dimensional gas of massless Dirac fermions in graphene.,» *nature ,* vol. 438, n. 7065, pp. 197-200, 2005.

[44] G. W. Hanson, «Dyadic Green's functions and guided surface waves for a surface conductivity model of graphene,» *Journal of Applied Physics ,* vol. 103, n. 6, 2008.

[45] A. H. Castro Neto, F. Guinea, N. M. Peres, K. S. Novoselov e A. K. Geim, «The electronic properties of graphene.,» *Reviews of modern physics,* vol. 81, n. 1, pp. 109-162, 2009.

[46] S. Luryi, «Quantum capacitance devices,» *Applied Physics Letters,* vol. 52, n. 6, pp. 501-503, 1988.

[47] J. Xia, F. Chen, J. Li e N. Tao, «Measurement of the quantum capacitance of graphene.,» *Nature nanotechnology,* vol. 4, n. 8, pp. 505-509, 2009.

[48] Z. Wang e W. Ren, «Mid-infrared optical modulator enabled by photothermal effect,» *light: science & applications ,* vol. 12, n. 1, p. 7, 2023.

[49] V. M. Passaro, C. De Tullio, . B. Troia, M. La Notte, G. Giannoccaro e F. De Leonardis, «Recent advances in integrated photonic sensors,» *Sensors,* vol. 12, n. 11, pp. 15558-15598, 2012.

[50] R. Rauf e B. Bennett, «Electrooptical effects in silicon,» *IEEE journal of quantum electronics,* vol. 23, n. 1, pp. 123-129, 1987.

[51] H. Agarwal, B. Terrés, L. Orsini, A. Montanaro, V. Sorianello, M. Pantouvaki, K. Watanabe, T. Taniguchi, D. Van Thourhout, M. Romagnoli e F. H. L. Koppens, «2D-3D integration of hexagonal boron nitride and a high-κ dielectric for ultrafast graphene-based electro-absorption modulators,» *Nature communications,* vol. 12, n. 1, p. 1070, 2021.

[52] M. Zhao, Y. Hao, C. Zhang, R. Zhai, R. Zhai, B. Liu, W. Liu, C. Wang, H. Jafri, M. A. Razaq, J. Liu, X. Ye, X. Zheng e H. Li, «Advances in Two-Dimensional Materials for Optoelectronics Applications,» *Crystals,* vol. 12, n. 8, p. 1087, 2022.

[53] M. Liu, X. Yin, E. Ulin-Avila, B. Geng, T. Zentgraf, L. Ju, F. Wang e X. Zhang, «A graphene-based broadband optical modulator,» *Nature 474,* n. 7349, pp. 64-67, 2011.

[54] H. Dalir, Y. Xia, Y. Wang e X. Zhang, «Athermal Broadband Graphene Optical Modulator with 35 GHz Speed,» *ACS photonics,* vol. 3, n. 9, pp. 1564-1568, 2016.

[55] M. Fan, H. Yang, P. Zheng, G. Hu, B. Yun e Y. Cui, «Multilayer graphene electro-absorption optical modulator based on double-stripe silicon nitride waveguide,» *Optics express,* vol. 25, n. 18, pp. 21619-21629, 2017.

[56] M. A. Giambra, V. Sorianello, V. Miseikis, S. Marconi, A. Montanaro, P. Galli, S. Pezzini, C. Coletti e M. Romagnoli, «High-speed double layer graphene electro-absorption modulator on SOI waveguide,» *Optics express ,* vol. 27, n. 15, pp. 20145-20155, 2019.

[57] J. Gosciniak e D. T. H. Tan , «Theoretical investigation of graphene-based photonic modulators,» *Scientific reports,* vol. 3, n. 1, p. 1897, 2013.

[58] S.-W. Ye, F. Yuan, X.-H. Zou, M. K. Shah, R.-G. Lu e Y. Liu, «High-Speed Optical Phase Modulator Based on Graphene-Silicon Waveguide,» *IEEE Journal of Selected Topics in Quantum Electronics,* vol. 23, n. 1, pp. 76-80, 2016.

[59] E. Palik e G. C. Ghosh, Handbook of thermo-optic coefficients of optical materials with applications, 1997.

[60] G. Cocorullo, F. Della Corte e I. Rendina, «Temperature dependence of the thermo-optic coefficient in crystalline silicon between room temperature and 550 K at the wavelength of 1523 nm,» *Applied physics letters,* vol. 74, n. 22, pp. 3338-3340, 1999.

[61] G. T. Reed e A. P. Knights, Silicon Photonics: An Introduction, West Sussex: John Wiley, 2004.

[62] R. Soref e B. R. Bennett, «IEEE journal of quantum electronics,» *Electrooptical effects in silicon,* vol. 23, n. 1, pp. 123-129, 1987.

[63] M. Quirk e J. Serda, Semiconductor manufacturing technology, NJ: Prentice Hall Upper Saddle River, 2001.

[64] L. Martinu, O. Zabeida e J. Klemberg-Sapieha, «Plasma-enhanced chemical vapor deposition of functional coatings.,» in *Handbook of deposition technologies for films and coatings*, Science, Applications and Technology, 2010, pp. 392-465.

[65] D. Rugar e P. Hansma, «Atomic force microscopy.,» *Physics today,* vol. 43, n. 10, pp. 23-30, 1990.

[66] CEA-LETI Photonics, [Online]. Available: https://europractice-ic.com/technologies/photonics/cea-leti/.

[67] S. G. Volz e G. Chen, «Molecular-dynamics simulation of thermal conductivity of silicon crystals.,» *Physical Review,* vol. 61, n. 4, p. 2651, 2000.

[68] B. J. Frey, D. B. Leviton e T. J. Madison, «Temperature-dependent Refractive Index of Silicon and Germanium,» *Optomechanical technologies for Astronomy,* vol. 6273, 2006.

[69] F. Brotzen, P. Loos e D. Brady, «Thermal conductivity of thin SiO2 films.,» *Thin Solid Films ,* vol. 207, n. 1-2, pp. 197-201, 1992.

[70] H. Gao, Y. Jiang, Y. Cui, L. Zhang, J. Jia e L. Jiang, «Investigation on the Thermo-Optic Coefficient of Silica Fiber Within a Wide Temperature Range,» *Journal of Lightwave Technology ,* vol. 36, n. 24, pp. 5881-5886, 2018.

[71] P. G. Klemens e R. K. Williams, «Thermal conductivity of metals and alloys.,» *International*

metals reviews , vol. 31, n. 1, pp. 197-215, 1986.

[72] G. Gülşen e M. N. Inci, «Thermal optical properties of TiO2 films.,» *Optical materials,* vol. 18, n. 4, pp. 373-381, 2002.

[73] J. Yue, M. Wang, J. Zou, T. Liu, J. Fang, X. Sun, Y. Wu e D. Zhang, «Low-loss silica waveguide 1× 8 thermo-optic switch based on large-scale multimode interference couplers,» *Optics Communications,* vol. 573, p. 131014, 2024.

[74] M. Wang, J. Yue, Z. Yao, T. Liu, X. Sun, Y. Wu e D. Zhang, «Low-power and wide-band 1 × 8 silica waveguide optical switch,» *Optics & Laser Technology,* vol. 171 , p. 110380, 2024.

[75] S. Wang e D. Dai, «Polarization-insensitive 2 × 2 thermo-optic Mach–Zehnder switch on silicon,» *Optics letters,* vol. 43, n. 11, pp. 2531-2534, 2018.

[76] Q. Chen, M. K. Wang, X. Xia Ma, H. Yao e K. X. Chen, «Broadband and low-random-phase-errors 2× 2 optical switch on thin-film lithium niobate,» *IEEE Photonics Journal,* vol. 14, n. 6, pp. 1-5, 2022.

[77] W. Li, L. Xu, J. Zhang, D. Mao, Y. D'Mello e Z. Wei, «Broadband polarization-insensitive thermo-optic switches on a 220-nm silicon-on-insulator platform.,» *IEEE Photonics Journal ,* vol. 14, n. 6, pp. 1-7, 2022.

[78] T. Chen,, Z. Ding,, Z. Dang, X. Jiang e Z. Zhang, «Function-versatile thermo-optic switch using silicon nitride waveguide in polymer.,» *Photonics,* vol. 10, n. 3, p. 277, 2023.

[79] M. Jin, G. Wu, X. Zhou, Q. Jiang, Z. Lin e W. Jiang, «Parabolic MMI coupler for 2× 2 silicon optical switch with robustly high extinction ratio for four paths.,» *IEEE Photonics Technology Letters,* vol. 35, n. 13, pp. 737-740, 2023.

[80] D. M. Pozar, in *Microwave engineering.*, Fourth Editions, University of Massachusetts at Amherst, John Wiley & Sons, 2012, pp. 26-30.

[81] A. Yariv e P. Yeh, Photonics: optical electronics in modern communications, New York: Oxford university press, 2007.

[82] Q. Xu e M. Lipson, «All-optical logic based on silicon micro-ring resonators,» *Optics Express,* vol. 15, n. 3, pp. 924-929, 2007.

[83] X. Liu, P. Ying, X. Zhong, J. Xu, Y. Han, S. Yu e X. Cai, «Highly efficient thermo-optic tunable micro-ring resonator based on an LNOI platform,» *Optics Letters,* vol. 45, n. 22, p. 2020, 6318-6321.

[84] M. Li, J. Ling, Y. He, U. A. Javid, S. Xue e Q. Lin, «Lithium niobate photonic-crystal electro-optic modulator,» *Nature communications,* vol. 11, n. 1, 2020.

[85] L. Wu, H. Liu, J. Li, S. Wang, S. Qu e L. Dong, «A 130 GHz Electro-Optic Ring Modulator with Double-Layer Graphene,» *Crystals ,* vol. 7, n. 3, p. 65, 2017.

[86] L. Yang, T. Hu, A. Shen, C. Pei, Y. Li, T. Dai, H. Yu, Y. Li, X. Jiang e J. Yang, «Proposal for a 2×2 Optical Switch Based on Graphene-Silicon-Waveguide Microring,» *IEEE Photonics Technology Letters ,* vol. 26, n. 3, pp. 235-238, 2013.

[87] X. Xiao, H. Xu, X. Li, Z. Li, T. Chu, Y. Yu e J. Yu, «High-speed, low-loss silicon Mach–Zehnder modulators with doping optimization.,» *Optics express ,* vol. 21, n. 4, pp. 4116-4125, 2013.

[88] M. Müller, M. Bouša, Z. Hájková, M. Ledinský, A. Fejfar, K. Drogowska-Horná, M. Kalbáč e O. Frank, «Transferless Inverted Graphene/Silicon Heterostructures Prepared by Plasma-Enhanced Chemical Vapor Deposition of Amorphous Silicon on CVD Graphene,»

Nanomaterials, vol. 10, n. 3, p. 589, 2020.

[89] G. Lupina, C. Strobel, J. Dabrowski, G. Lippert, J. Kitzmann, H. Krause, C. Wenger, M. Lukosius, A. Wolff, M. Albert e J. Bartha, «Plasma-enhanced chemical vapor deposition of amorphous Si on graphene,» *Applied Physics Letters,* vol. 108, n. 19, p. 193105, 2016.

[90] F. Pizzocchero, L. Gammelgaard, B. S. Jessen, J. M. Caridad, L. Wang, J. Hone, P. Bøggild e T. J. Booth , «The hot pick-up technique for batch assembly of van der Waals heterostructures,» *Nature communications,* vol. 7, n. 1, p. 11894, 2016.

[91] Z. Xiao, K. Kisslinger, S. Chance e S. Banks , «Comparison of Hafnium Dioxide and Zirconium Dioxide Grown by Plasma-Enhanced Atomic Layer Deposition for the Application of Electronic Materials,» *Crystals,* vol. 10, n. 2, p. 136, 2020.

[92] L. Liao, J. Bai, R. Cheng, Y.-C. Lin, S. Jiang, Y. Huang e X. Duan, «Top-gated graphene nanoribbon transistors with ultrathin high-k dielectrics,» *Nano letters,* vol. 10, n. 5, pp. 1917-1921, 2010.

[93] P. Giannozzi, S. Baroni, N. Bonini, M. Calandra, R. Car, C. Cavazzoni e D. Ceresoli, «QUANTUM ESPRESSO: a modular and open-source software project for quantum simulations of materials,» *Journal of physics: Condensed matter,* vol. 21, n. 39, p. 395502, 2009.

[94] F. Giubileo e A. Di Bartolomeo, «The role of contact resistance in graphene field-effect devices,» *Progress in Surface Science ,* vol. 92, n. 3, pp. 143-175, 2017.

[95] D. De Fazio, D. G. Purdie, A. K. Ott, P. Braeuninger-Weimer, T. Khodkov, S. Goossens, T. Taniguchi, K. Watanabe, P. Livreri, F. H. L. Koppens, S. Hofmann, I. Goykhman, A. C. Ferrari e A. Lombardo, «High-mobility, wet-transferred graphene grown by chemical vapor deposition,» *ACS nano,* vol. 13, n. 8, pp. 8926-8935, 2019.

[96] L. Viti, D. G. Purdie, A. Lombardo, A. C. Ferrari e M. S. Vitiello, «HBN-encapsulated, graphene-based, room-temperature terahertz receivers, with high speed and low noise.,» *Nano Letters,* vol. 20, n. 5, pp. 3169-3177, 2020.

[97] C. T. Phare, Y.-H. D. Lee, J. Cardenas e M. Lipson, «Graphene electro-optic modulator with 30 GHz bandwidth,» *Nature photonics,* vol. 9, n. 8, pp. 511-514, 2015.

[98] H. Nezamdoost, M. Nikoufard e H. Saghaei , «Graphene-based hybrid plasmonic optical electro-absorption modulator on InP platform,» *Optical and Quantum Electronics,* vol. 56, n. 3, p. 482, 2024.

[99] M. M. A. Eid, A. N. Z. Rashed, V. Sorathiya, S. Lavadiya, M. A. Habib e I. Sadegh Amiri, «GaAs electro-optic absorption modulators performance evaluation, under high-temperature variations,» *Journal of Optical Communications,* vol. 45, n. s1, pp. s359-s368, 2025.

[100] Y. Tzeng e T. H. Lin, «Dry Etching of Silicon Materials in SF 6 Based Plasmas: Roles of and Gas Additives.,» *Journal of the Electrochemical Society,* vol. 134, n. 9, p. 2304, 1987.

[101] F. Laerme, A. Schilp, K. Funk e M. Offenberg, «Bosch deep silicon etching: improving uniformity and etch rate for advanced MEMS applications,» in *IEEE International MEMS 99 Conference. Twelfth IEEE International Conference on Micro Electro Mechanical Systems*, Orlando, FL, USA,, 1999.

[102] F. M. Smits, « Measurement of sheet resistivities with the four-point probe.,» *Bell System Technical Journal,* vol. 37, n. 3, pp. 711-718, 1958.

[103] N. Farmakidis, N. Youngblood, J. S. Lee, J. Feldmann, A. Lodi, X. Li, S. Aggarwal, W. Zhou, L. Bogani, W. H. Pernice, C. D. Wright e H. Bhaskaran, «Electronically reconfigurable photonic switches incorporating plasmonic structures and phase change materials,» *Advanced Science,*

vol. 9, n. 20, p. 2200383, 2022.

[104] G. Cocorullo, F. g. Della Corte e I. Rendina, «Temperature dependence of the thermo-optic coefficient in crystalline silicon between room temperature and 550 K at the wavelength of 1523 nm,» *Applied physics letters,* vol. 74, n. 22, pp. 3338-3340, 1999.

[105] W. E. Spear e P. G. Comber, «Substitutional doping of amorphous silicon,» *Solid state communications,* vol. 17, n. 9, pp. 1193-1196, 1975.

[106] B. G. Yacobi, R. W. Collins, G. Moddel, P. Viktorovitch e W. Paul, «Effect of oxygen on the optoelectronic properties of amorphous hydrogenated silicon,» *Physical Review ,* vol. 24, n. 10, p. 5907, 1981.

[107] J. E. Proctor, D. A. M. Armada e A. Vijayaraghavan, An Introduction to Graphene and Carbon Nanotubes, CRC Press, 2017.

SOMMARIO
Questa tesi analizza la progettazione, la simulazione, la fabbricazione e la caratterizzazione di commutatori fotonici integrati su piattaforme in silicio per applicazioni nell'ambito delle telecomunicazioni. Vengono studiate diverse architetture per lo switching, con particolare attenzione ai commutatori termo- ottici adiabatici e quelli basati su interferenza multimodale (MMI), nonché a dispositivi elettro-ottici basati su grafene. Viene proposto e analizzato un nuovo switch termo-ottico adiabatico, che mostra banda larga, tolleranza alla polarizzazione e robustezza ai processi di fabbricazione. Sono inoltre progettate e simulate matrici di commutazione scalabili basate su questa architettura. In parallelo, sono illustrate la fabbricazione e la caratterizzazione di commutatori Mach–Zehnder basati su MMI, che mostrano un buon accordo con i risultati delle simulazione. Per superare i limiti di velocità dei dispositivi termo-ottici, vengono studiati modulatori e commutatori elettro-ottici basati su grafene, evidenziando il potenziale delle piattaforme ibride silicio– grafene. Nel complesso, questo lavoro fornisce soluzioni scalabili ed efficienti dal punto di vista energetico per sistemi di comunicazione ottica riconfigurabili di nuova generazione.

ABSTRACT
This thesis investigates the design, simulation, fabrication, and characterization of integrated photonic switches on silicon platforms for telecommunication applications. Several switching architectures are analyzed, with particular focus on adiabatic and multimode interference (MMI) thermo-optic switches, as well as graphene-based electro-optic devices. A novel adiabatic thermo-optic switch is proposed and studied, demonstrating broadband, polarization-tolerant, and fabrication-robust performance. Scalable switching matrices based on this architecture are also designed and simulated. In parallel, MMI-based Mach–Zehnder switches are fabricated and experimentally characterized, showing good agreement with simulations. To overcome the speed limitations of thermo-optic devices, graphene-enabled electro-optic modulators and switches are investigated, highlighting the potential of hybrid silicon–graphene platforms. Overall, this work contributes scalable and energy-efficient solutions for next-generation reconfigurable optical communication systems.

Babak Hashemi

Design, fabrication and characterization of photonic integrated switch circuits for telecommunication applications

SCUOLA di DOTTORATO

Dottorato di Ricerca in Ingegneria dell'Informazione

Babak Hashemi

DESIGN, FABRICATION AND CHARACTERIZATION OF PHOTONIC INTEGRATED SWITCH CIRCUITS FOR TELECOMMUNICATION APPLICATIONS

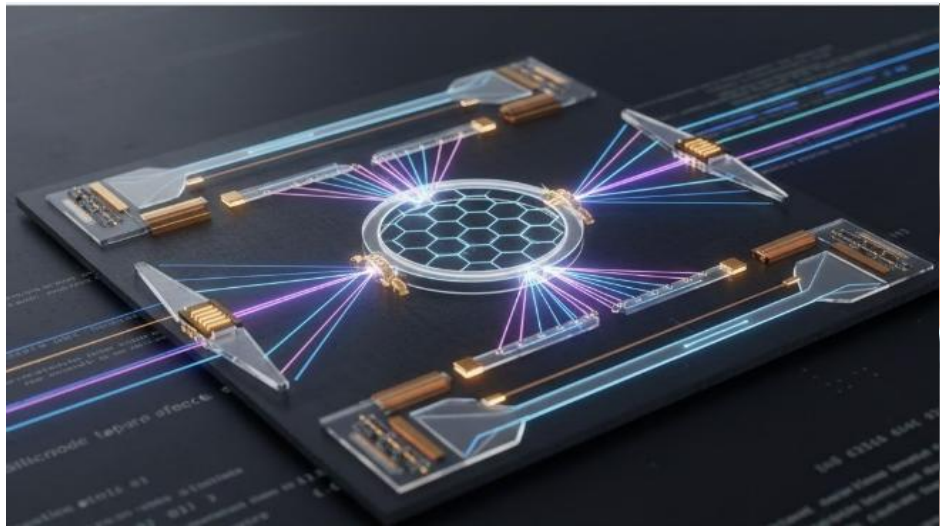

SCUOLA di DOTTORATO